UiT The Arctic University of Norway

Faculty of Science and Technology

Investigation of Multilayers in Polar Mesospheric Summer Echoes

Dorota Sofia Jozwicki

A dissertation for the degree of Philosophiae Doctor

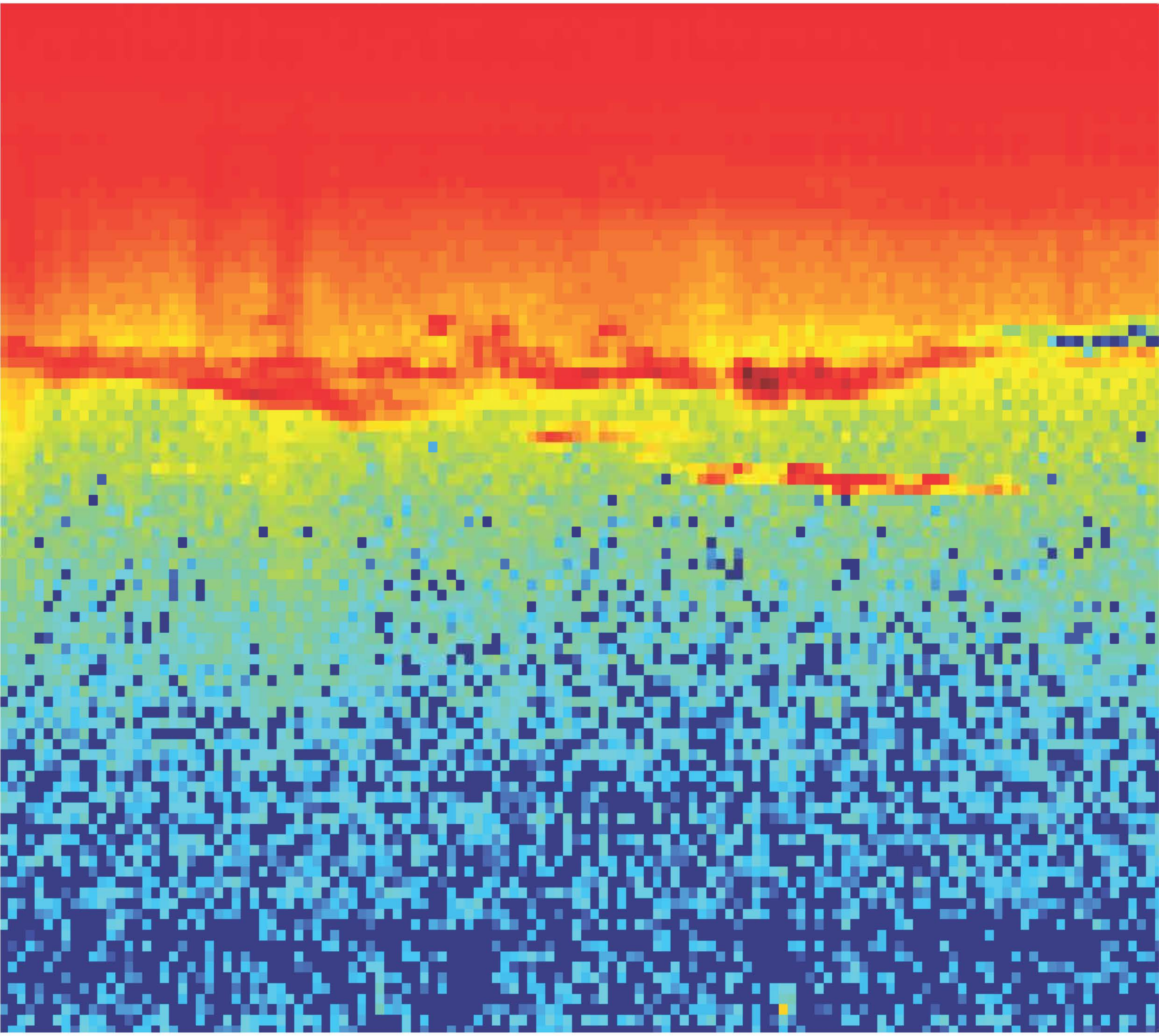

Investigation of Multilayers in Polar Mesospheric Summer Echoes

Dorota Sofia Jozwicki

A dissertation for the degree of Philosophiae Doctor (PhD)
at UiT The Arctic University of Norway

November 2024

Cover:
EISCAT VHF data plotted by Dorota Jozwicki using MATLAB

”Most of the fundamental ideas of science are essentially simple, and may, as a rule, be expressed in a language comprehensible to everyone.”

— Albert Einstein

Abstract

Understanding the influence of the Sun and space on the Earth's atmosphere is of current interest, as it may be valuable in the context of global climate change research. Polar Mesospheric Summer Echoes (PMSE) are phenomenona that rely on the presence of ice particles, offering insights into the mesosphere's temperature and water vapor content. This thesis aimed to investigate PMSE in the upper atmosphere using the EISCAT VHF radar data, with a focus on quantifying PMSE multilayers during solar maximum and solar minimum.

To achieve this, a random forests-based model was used to segment PMSE data within the radar observations. This model allowed for a finer exploration of PMSE multilayers and was applied to investigate the multi-layered PMSE structures during different phases of the solar cycle, and under varying ionospheric conditions.

The output of the model enabled segmentation of PMSE data with reduced back-scattered power threshold filtering, preserving a larger number of valuable data points compared to previous studies. This approach enabled the examination of both monolayer and multilayer PMSE structures in finer detail. Notably, during solar maximum, PMSE demonstrated higher average altitude, echo power, and layer thickness compared to solar minimum. Analysis of individual layers in multilayer sets shows that the altitude of the first, second, and third highest layers increases with the number of layers. Additionally, the altitude of the the lowest layer generally matched with the altitude of noctilucent clouds (NLC), as reported by observers. These clouds are visible due to light scattering off their ice particles. Furthermore, a positive correlation between echo power and ionospheric electron density at 92 km altitude above PMSE was observed. This indicates that higher electron densities might be essential for the observation of multi-layered PMSE.

Looking ahead, future studies could explore the links between multi-layered PMSE formation, winds, and gravity waves. Future research could also focus on investigating mean altitudes of different multilayers by utilizing different radars or operating modes offering better resolution within the 80 to 90 km altitude range. Additionally, extending the data analysis to include more EISCAT data of more than one solar cycle to analyse possible trends could provide further insights into PMSE. The analysis tools that emerged from this work can be used for examining many more hours of EISCAT observations.

Acknowledgements

I am immensely grateful to my main supervisor, Ingrid Mann, for her guidance throughout this journey. Despite the challenges, her constructive critiques and unwavering encouragement played a pivotal role in my successful completion of this thesis.

My sincere thanks go to my co-supervisor, Puneet Sharma, for his expert guidance on the programming aspects of the projects and his constant support. I am also grateful to Devin Huyghebaert, whose guidance and encouragement during the final paper and the last part of this doctoral journey were immensely valuable. I would also like to express my gratitude to Ulf-Peter Hoppe for his assistance and constructive feedback.

I extend my appreciation to the EISCAT VHF facility for providing easy access to the data, and I am thankful to the Research Council of Norway for funding this research. Special thanks to Anders Tjulin at EISCAT for insightful discussions and assistance with the EISCAT data. I am grateful to all the reviewers of the papers for their constructive and helpful comments. I also deeply appreciate Gabriela Sirbu for her support with administrative and logistical matters, and for always being there to help.

A heartfelt thank you to my loved ones. First and foremost, I would like to express my deepest gratitude to my partner, Sebastian Arnesen, for his unwavering support throughout this journey. Without you, this achievement would not have been possible. I also extend my sincere appreciation to my dear friends, including Vitalia Khokhlova, Marie Claret, Jonathan Lemus, Charly Leroy, Antoine Nuel, Silje Strand, Bilal Babar, Margherita Falavigna, Anton Garri Fagerbakk, Luka Jerončić, Christian Johnsen, and many others, for their encouragement and support, and for bringing joy during challenging times. Lastly, my deepest and most heartfelt thanks go to my family in France, Poland, and Norway, for their endless love and support, which have been the foundation of this accomplishment.

Finally, I would like to express my appreciation to the defense committee for taking the time to read and evaluate this thesis.

Dorota Jozwicki,
Oslo 2024

List of publications

This thesis consists of a subject introduction and the following papers which will be referred to by their Roman numerals. In addition, an open access database (Labels) containing labeled images is made available.

Paper I	**Jozwicki, D.** and Sharma, P. and Mann, I.: Investigation of Polar Mesospheric Summer Echoes Using Linear Discriminant Analysis, Remote Sensing, doi:10.3390/rs13030522, 2021, published
Paper II	**Jozwicki, D.** and Sharma, P. and Mann, I. and Hoppe, U.-P.: Segmentation of PMSE Data Using Random Forests, Remote Sensing, doi:10.3390/rs14132976, 2022, published
Labels	**Jozwicki, D.** and Sharma, P. and Mann, I. and Hoppe, U.-P.: Labels used for model training in the study by Jozwicki et. al., doi:10.18710/NHD4HU, 2023, DataverseNO, *in revision*
Paper III	**Jozwicki, D.** and Sharma, P. and Huyghebaert, D. and Mann, I.: Polar mesospheric summer echo (PMSE) multilayer properties during the solar maximum and solar minimum, Annales Geophysicae, doi: 10.5194/angeo-42-431-2024, 2024, published

Contents

Chapter 1

Introduction

Space physics is a fascinating and complex field that seeks to understand the physical phenomena that occur in space. In particular, the influence of the Sun and space on the Earth's atmosphere are of current interest, as it can provide us insights into global climate change. The mesosphere is a layer of the Earth's atmosphere that is characterized by temperature decreasing with altitude; its varying boundaries are at the lower altitude around 50 to 60 km and at upper altitude around 80 to 100 km. Its upper boundary, the mesopause, is also considered part of the near-space environment and displays interesting phenomena.

One such phenomenon of great interest are Polar Mesospheric Summer Echoes (PMSE), which happens at polar latitudes during summer months. In the Northern hemisphere, PMSE typically occur between May and August, and in the Southern hemisphere from November to February. Investigating the processes that form PMSE presents challenges due to the altitude location. PMSE predominantly occur at altitudes ranging from 80 to 90 km, which makes acquiring in-situ measurements particularly difficult. While meteorological balloons can reach at best the upper stratosphere and satellites can reach the thermosphere, they cannot access the precise PMSE region. Only sounding rockets have the capability to physically reach this altitude, but during a very short time interval. Observation from the ground have become the main tool for investigating the mesosphere and mesopause region. Moreover, radar observations allow observations independent from weather conditions. The understanding of the PMSE formation is therefore valuable for interpretation of radar data.

The study by Ecklund and Balsley (1981) marked the first observation of PMSE using the Poker Flat mesosphere-stratosphere-troposphere (MST) radar in Alaska. Their findings revealed a seasonal preference for PMSE formation during the summer months, primarily occurring at altitudes between 80 and 100 km, with a peak occurrence at 85 km altitude. Fainter echoes were observed at lower altitudes (55-80 km) during non-summer months. Subsequent research has further explored the nature of PMSE. Notably, Rapp and Lübken (2004) provided an extensive review on PMSE observations and the underlying formation process. They identified specific conditions necessary for PMSE occurrence, including very cold temperatures (130K) that facilitate the formation of ice particles in the mesosphere. If these particles become electrically charged and are arranged in a particular manner due to turbulence, along with the presence of sufficient free electrons, PMSE can be detected using radar systems.

A few studies exist about multiple PMSE layers. Among the existing research we can note a study on the occurrence and mean altitude of PMSE layers (Hoffmann et al., 2005) and a study explaining multiple PMSE layers resulting from successive nucleation cycles of ice particles (Li et al., 2016). PMSE formation may vary with the degree of ionization in the ionosphere and in general with the solar cycle. Also long-term trends possibly occur, as recent investigations suggest a trend in water vapor concentration at this altitude (Lübken et al., 2018). The EISCAT VHF radar was used for a number of PMSE investigations in the past, as for instance in the studies by Shucan et al. (2019), Jozwicki et al. (2021), and (Narayanan et al., 2022). The EISCAT radars are designed to measure the incoherent scatter from the ionosphere. The EISCAT VHF radar simultaneously provides measurements of PMSE and of the electron density in the ionosphere above the PMSE. This allows us to study the PMSE layers together with the ionospheric conditions under which they occur.

The main focus of this thesis lies in the investigation of PMSE, with the central question being: how do the characteristics of PMSE multi-layered structures change in response to the solar cycle, encompassing both solar maximum and minimum phases. The first objective is to implement a classification model that could effectively identify PMSE data within the EISCAT VHF radar data and to quantify the less explored PMSE multilayers. While PMSE have been largely investigated now for decades, these multilayers have received limited attention within the scientific community, making them a valuable area of research for this study. The second objective is to to apply the model on a set of EISCAT observations to investigate how the multilayers appear during different phases of the solar cycle and during different ionospheric conditions.

The thesis will be structured as follows. Chapter 2 describes the physics underlying the formation of PMSE and presents an overview of current research on PMSE monolayers and multilayers. Chapter 3 focuses on the implementation of a classification tool designed to pre-select PMSE data. Chapter 4 will discuss the results obtained by applying the classification model to EISCAT VHF data. It encompasses our findings regarding PMSE monolayers and multilayers, along with our analyses and interpretations. Finally, the thesis concludes by summarizing our research outcomes and proposing avenues for future investigation.

Chapter 2

PMSE

PMSE is an area of study that is still being explored and expanding. While there are many intriguing questions being investigated, it is natural to wonder about the value of PMSE research and its contributions to the scientific field. PMSE are closely connected to the water vapour content in the mesosphere and rely on the presence of neutral air turbulence, which is influenced by the movement of air masses. This means that it is possible to gather information about mesospheric water content and track its variations over time (Lübken et al., 2018). This topic will be discussed in more detail in the following section. Furthermore, the occurrence frequency of Noctilucent Clouds (NLC) has increased over the years (Lübken et al., 2018). Both PMSE and NLC rely on the presence of ice particles, and therefore on the presence of water vapour and cold temperatures in the mesosphere. This chapter delves into the prerequisites for PMSE formation, presents general knowledge about PMSE, and explores previous research on PMSE concerning single layers and multiple layers, as well as its relation to the solar cycle.

2.1 PMSE formation

During the summer months, PMSE can be measured by radars in the upper atmosphere. PMSE exhibit a distinctive wavy pattern in terms of their height and thickness variations over time. The formation of PMSE relies on the presence of turbulence, free electrons, and charged aerosols. The charged aerosols contain water ice and are dependent on low temperatures and adequate water vapor. It has been suggested that Meteor Smoke Particles (MSP), formed through meteor ablation and recondensation (Hunten et al., 1980), can serve as the probable condensation nuclei for PMSE (Rapp and Lübken, 2004).

MSP, as indicated by Megner et al. (2006), are believed to serve as these nucleation centers, thereby initiating the formation of ice particles. These minuscule smoke particles are formed in the upper atmosphere through the ablation of meteoroids. These particles have typical sizes in the nanometer scale. The MSP attract water vapor molecules, leading to the nucleation and growth of ice particles in the mesospheric region. It is worth noting that the formation

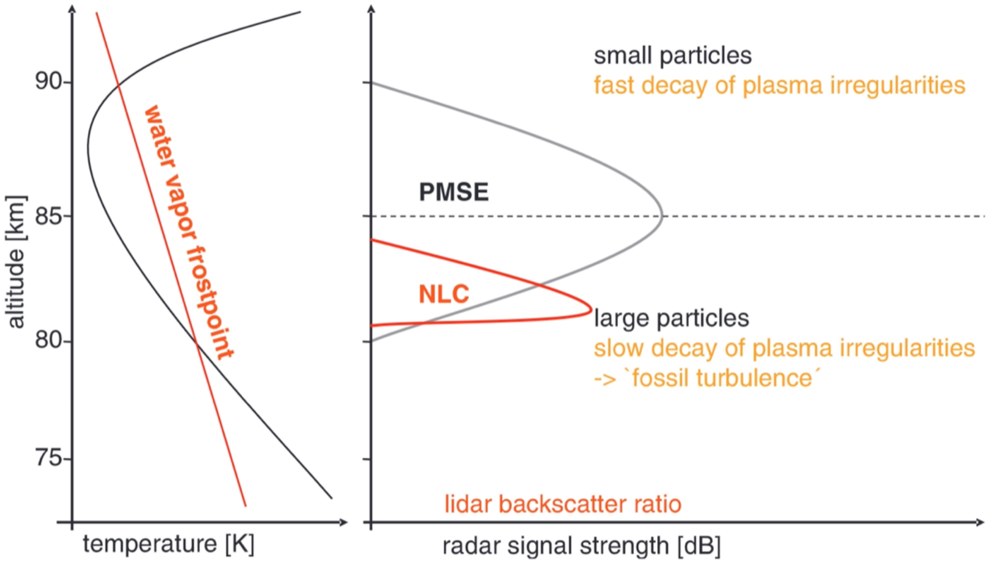

Figure 2.1: On the left hand side : altitude distribution of the temperature at altitude from 75 to 90 km altitude. The red line represents the water vapor frost-point limit. On the right hand side : illustration comparing the altitude distribution of PMSE and NLC. PMSE is represented by a black line with grey shading, and NLC is represented by a red line. The relevant physical mechanisms at different altitudes are also noted. Figure adapted from the study by Rapp and Lübken (2004).

of ice particles can occur without MSP acting as nucleation centers, with only ice water present in them. In this thesis, we have chosen to refer to particles covered with ice, or particles made of ice alone as ”ice particles”. Additionally, we will use the term ”dust” to encompass various scenarios, including ice particles, MSP alone, or ice particles without MSP acting as nucleation centers.

Another key component is a sufficiently low temperature which can be attained in the polar mesopause during summer months. The mesopause is defined as the boundary between the mesosphere and the thermosphere and is the coldest portion of the atmosphere. The left hand side of Figure 2.1 from the study by Rapp and Lübken (2004) shows the temperature variation in the mesosphere and the water vapor frost-point for these altitudes.

One can notice that at altitudes where PMSE are observed, between 80 and 90 km altitude, is where the temperature descends below the water vapor frost point, making it possible for water molecules to condense around nucleation centers. The temperature of the summer mesopause is lower compared to the winter mesopause. This temperature difference is caused by ascending air at the summer pole and descending air at the winter pole, being part of a residual summer pole to winter pole circulation pattern. When air rises, it expands and cools, leading to a colder summer mesopause. On the other hand, when air descends, it compresses and the associated increase in temperature leads to a warmer winter mesopause. Because of this, during the summer months at polar latitudes, the mesopause reaches its coldest temperatures.

There is an intriguing connection between PMSE and NLC worth exploring. As mentioned in the introduction, both phenomena provide insights into the water content in the mesosphere, as they are associated with the presence of ice particles. NLC, known as the highest clouds in the atmosphere, consist of the same ice particles found in PMSE. The key distinction is that in NLC, these ice particles grow significantly larger, becoming visible to the naked eye.

The right hand side of Figure 2.1 provides a comparison of the altitudes at which PMSE and NLC form. Once the criterion of a sufficiently low temperature below the water vapor frost point is obtained, NLC will form beneath PMSE. This aligns with the fact that NLC consist of larger and heavier particles (Rapp and Lübken, 2004). Also, NLC are observed using lidar or visual observation methods, while PMSE are observed using radar. This distinction arises from the scattering of the radar signal by electrons structured within the PMSE region, highlighting the significance of ice particle charging in PMSE observation, as discussed earlier. On the other hand, NLC do not require a charging mechanism and can be directly observed with the naked eye, cameras, or lidar instruments.

Historically, ice particles were first observed as NLC, then as PMSE, and finally as Polar Mesospheric Clouds (PMC). In fact, NLC and PMC are both made of ice particles. They are the same thing, the only difference is that PMC are observed from space, and NLC are observed from the ground (Rapp and Lübken, 2004). Research about those clouds is still ongoing to understand better the instabilities leading to turbulence in the upper mesosphere during polar summer. The study by Fritts et al. (2019) presents new observations together with a description of the open questions in this area.

The turbulence of the neutral air plays another key role in PMSE formation. This turbulence can be caused by the presence of gravity waves and winds at mesospheric altitudes but also at altitudes above or below our altitude of interest. Upon reaching mesospheric altitudes, these waves break, leading to the generation of turbulence in the surrounding neutral air and interactions with other charged particles (Rapp and Lübken, 2004). This high turbulence and the present winds at these altitudes increase the air mixing. Figure 2.2 from Megner et al. (2006) shows a distribution of the wind velocity as a function of altitude, with the dashed line representing the wind profile for the summer, and the dashed and dotted line represents the profile for the winter. One can see that the winds are stronger in the summer than during the winter, and they have a peak velocity at 90km altitude, which is very close to the PMSE formation altitude.

Turbulence plays a crucial role in the formation of PMSE. However, it is possible to observe PMSE events even when there is no ongoing neutral air turbulence at that precise moment. This phenomenon is known as ”fossil turbulence” (Rapp and Lübken, 2004). The reason behind this is that if turbulence

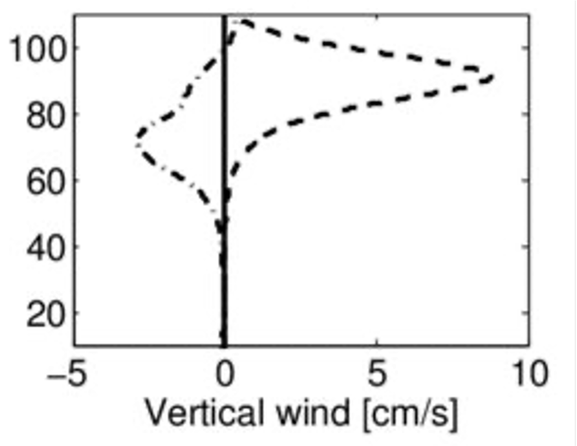

Figure 2.2: Wind profile as a function of altitude. The vertical axis shows the altitude with vales ranging from 20 to 100 km. The dashed line represents the wind profile for the summer, and the dashed and dotted line represents the profile for the winter. Figure obtained from the study by Megner et al. (2006).

occurred relatively recently, its effects can still be present at the place where they occurred. When turbulence occurs, it organizes the surrounding ice particles, consequently influencing the electrons around in a manner favorable for radar detection. Even after the turbulence subsides, this organized structure persists for a certain period, determined by the diffusion of the ice particles. A turbulent event lasts approximately 15 min in accordance with model results and observations from Andreassen et al. (1994) and Czechowsky and Rüster (1997).

Rapp and Lübken (2003) proposed a method to estimate the frequency of PMSE occurrence using the observed frequencies of turbulence. Figure 2.3 illustrates this concept. It is possible to see that the Signal to Noise Ratio (SNR) decay depends on the size of the particles, once the turbulence stops. The SNR of smaller particles will decrease faster than the SNR of bigger particles. Rapp and Lübken (2003) calculated the decay times for a decay of 10 dB. According to their work, the decay time for a signal by a number Φ of dB may be written as :

$$\tau_{diff}^{-\Phi dB} = \frac{\lambda^2 \Phi / 10 ln(10)}{8\pi^2 D_2^0} \approx 0.02\Phi \frac{\lambda^2 r_A^2}{\nu} \tag{2.1}$$

In the given equation, D_2^0 represents the electron diffusion coefficient resulting from their interaction with charged aerosol particles. λ denotes the radar wavelength, r_A represents the aerosol radius, and ν represents the kinematic viscosity of air. The approximate formula on the right side of Equation 2.1 uses units of meters for radar wavelength, nanometers for aerosol radius, and square meters per second for kinematic viscosity, resulting in the diffusional decay time τ_{diff} being expressed in seconds. Equation 2.1 reveals that the decay time is proportional to the square of both the radius of the charged

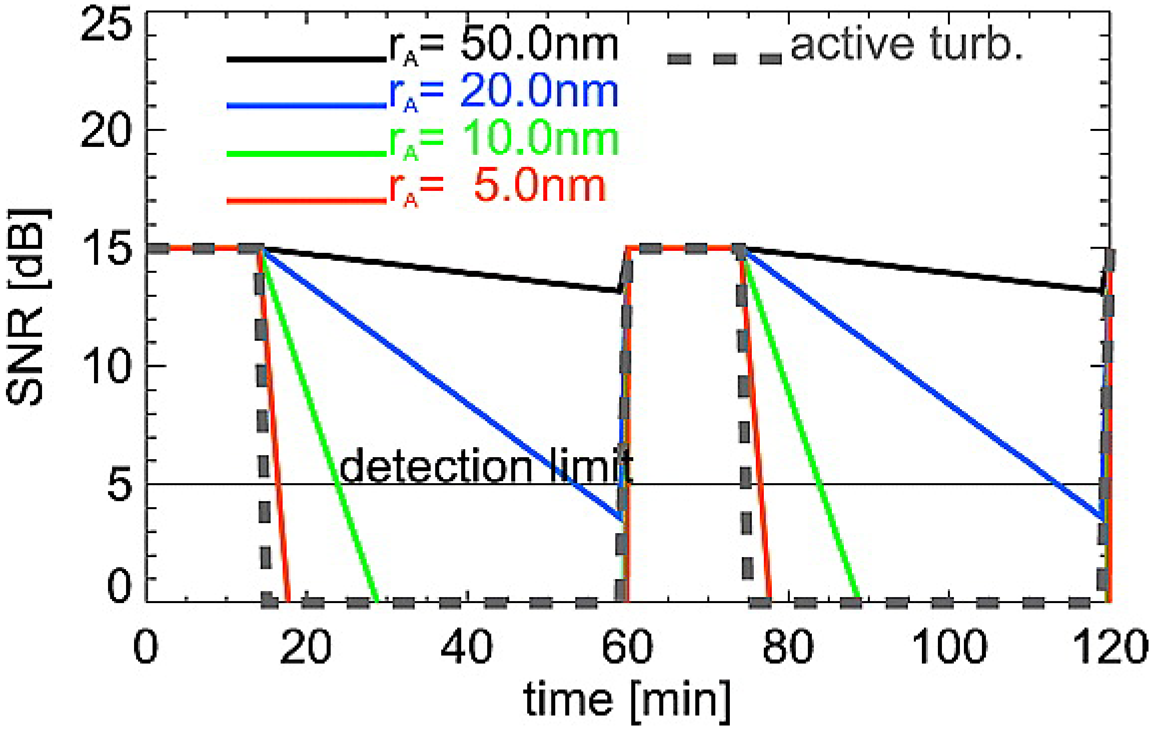

Figure 2.3: The change in radar signal to noise ratio over time is shown in relation to periodic bursts of neutral air turbulence (shown as gray dashed lines), resulting in an SNR of 15 dB. The decay of SNR for various assumed aerosol particle radii is represented by the colored lines. The horizontal line at SNR = 5 dB represents the assumed detection limit. Figure obtained from Rapp and Lübken (2003).

particles involved and the radar wavelength.

Rapp and Lübken (2004) show in their study that for particles smaller than 10 nm, the decay time is relatively short. For instance, particles with a radius of 5 nm exhibit a decay time of only 2.5 minutes, while particles with a radius of 10 nm have a decay time of 10 minutes. Due to the quadratic dependence of decay time on aerosol radius, the decay time increases significantly. For aerosol particles with a radius of 20 nm, the decay time is already 40 minutes, and for particles with a radius of 50 nm, which exist in the NLC environment, the decay time can extend to several hours.

In their study, Rapp and Lübken (2003) also derived Equation 2.2 given below, in which they express the PMSE Occurrence Rate (POR) as a function of the Turbulence Occurrence Rate (TOR). They note that for altitudes above 88 km, POR follows TOR almost one to one. This is caused by the fact that at these altitudes, the particles are smaller and their decay time is therefore short. This means that as soon as the turbulence stops, the PMSE will stop as well. However, at lower altitudes and especially at altitudes lower than 85 km, POR is much higher than TOR. This is because of the fossil turbulence due to the fact that the particles are larger than at higher altitudes. This statement can be connected back to Figure 2.1, where one can see on the right hand side of the

Figure a comparison of PMSE altitudes versus NLC altitudes. Due to the above mentioned correlation between the size of the particles and the decay time, it is logical that smaller ice particles at higher altitudes which are at the origin of PMSE, would also have short a decay time compared to the particles further down, at NLC altitudes.

$$POR = TOR\left(1 + \frac{\tau_{diff}^{-10dB}}{\tau_{turb}}\right) \tag{2.2}$$

The mesosphere is populated by various constituents, including ice particles, free electrons, ions, and neutrals. In order to obtain PMSE, we need the ice particles to be charged to maintain significant fluctuations in the electron gas at scales around the Bragg scale, which is equivalent to the radar's half wavelength. Newly formed ice particles become charged through several processes, most notably collisions with free electrons and ions driven by thermal motion. The lighter electrons experience more frequent collisions with the ice particles compared to ions and accumulate faster on the particles. So, the ice particles typically acquire a negative equilibrium charge. However, when other charging processes play a role, the equilibrium charge can be positive. Notably, when particle precipitation occurs, high-energy particles may dislodge electrons from the ice particle's surface, known as secondary emission. Research conducted by Baumann et al. (2016) explored this phenomenon and revealed that such cases are relatively rare, with the majority of ice particles maintaining a negative charge. Furthermore, the study from Baumann et al. (2016) highlighted the influence of the ionosphere on ice particle charging. A few additional scenarios resulting in the charging of ice particles include the photoelectric effect, and photo-detachment. The photoelectric effect consists in incoming photons sufficiently energetic to dislodge an electron from within the ice particle, while photo-detachment consists in photons that would detach an electron from the surface of the ice particle. For more information about the different charging mechanisms, please see the thesis from Baumann (2016).

2.2 Measurement of PMSE

Radar detection of PMSE becomes possible when all the conditions for formation are present. This includes very cold temperatures, the charging of ice particles formed due to the cold temperatures, their spatial arrangement due to turbulence, and the presence of sufficient free electrons. Figure 2.4 shows all the necessary initial conditions for PMSE observation. One can distinguish three major categories in this process, which are denoted by the three different color groups. The blue group on the top contains the turbulence, the ice particles and the spatial structure of ice particles. It represents the first step during which the initial structural configuration of the ice particles take place, which is needed for the rest of the process to unfold. The green group

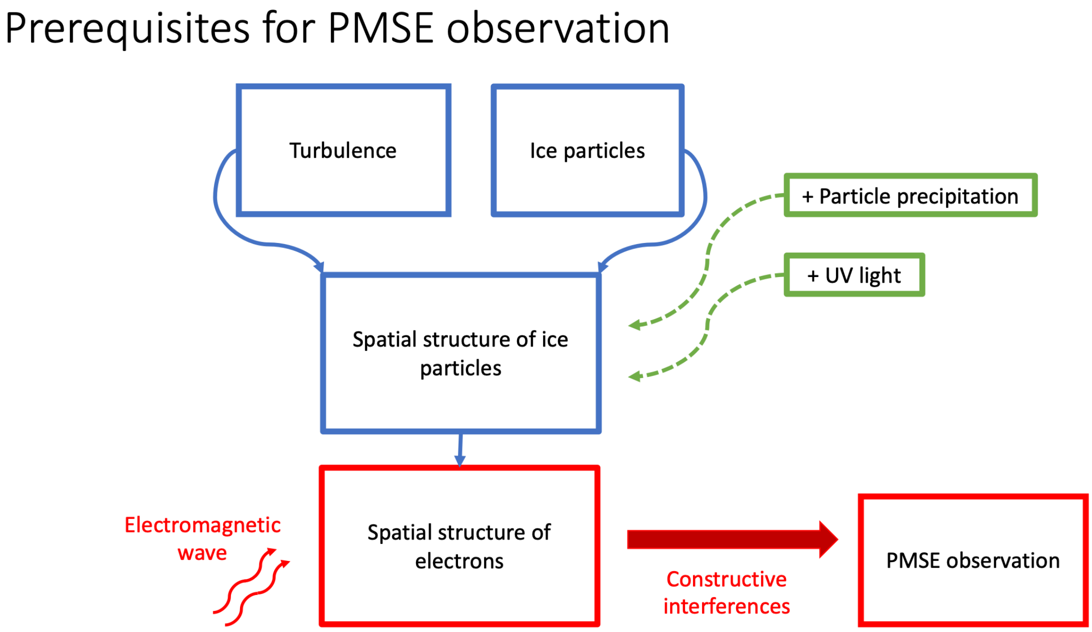

Figure 2.4: Illustration of PMSE formation as discussed in the text. The prerequisite atmospheric features are marked in blue, the radar echoe formation is marked in red and in green are marked conditions that influence the electron density and the dust charging and that may vary at the PMSE altitude.

contains the particle precipitation and the UV light. This group represents the charging mechanisms of the ice particles, which might increase or decrease the observed intensity of the echo power of the PMSE. Finally the red group contains the electromagnetic wave, the spatial structure of electrons, the constructive interferences and the PMSE observation. This group represents the part of the process which is connected to the radio wave scattering, and has to do with the final necessary components for the radar observation of the PMSE to be possible.

PMSE are strong radar echoes that have a characteristic wavy pattern with variations in height and thickness over time. These echoes can manifest as a single layer (monolayer) or multiple layers (multilayers). Figure 2.5 illustrates a recorded instance of PMSE data obtained from the EISCAT VHF radar near Tromsø, showcasing an example of three multilayers visible within the depicted red frame.

In this thesis, all the data were obtained from the EISCAT VHF radar, which is situated near Tromsø and operates at a frequency of 224 MHz. The primary function of the EISCAT VHF radar is to measure the small scale fluctuations in electron density within the ionospheric plasma. When an electromagnetic wave is emitted by the radar and propagates through a section of the ionosphere, the electrons within the ionosphere will start to oscillate due to the electric

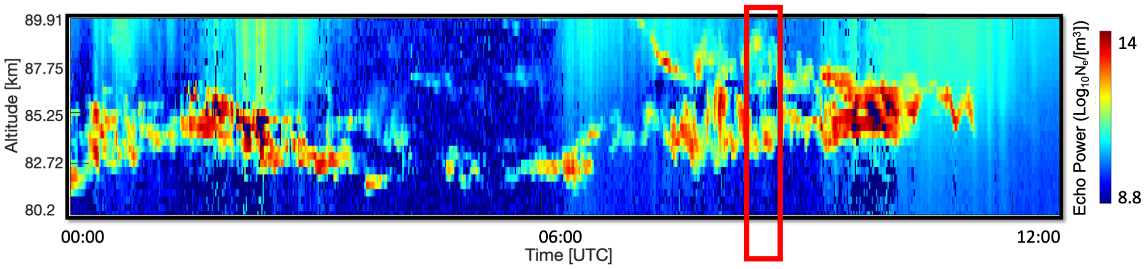

Figure 2.5: Data from EISCAT VHF from 16 July 2015 from 00:00 to 12:00, showing an example of a PMSE event that contains 3 multilayers in the red frame. This figure comes from the study by Jozwicki et al. (2024)

field of the incoming wave. As a result, the electromagnetic wave is scattered by the electrons at the same frequency as the incoming wave, a phenomenon known as Thomson scattering. The Doppler spectrum observed is a result of the distribution of electron velocities. This process, referred to as incoherent scatter, relies on the ionospheric plasma parameters, and it is possible to extract valuable information such as electron density, as well as electron and ion temperatures (Beynon and Williams, 1978) from the recorded signal. Additionally, Rapp and Lübken (2004) highlight the contrasting features of PMSE in comparison to incoherent scatter at the same altitude. PMSE signals tend to be stronger than incoherent scatter and exhibit a narrower spectrum. Figure 2.6 shows a typical spectrum of incoherent scatter in comparison to PMSE.

Within the turbulent regions in the mesosphere the electron distribution is structured and influenced by the motion and turbulence of the neutral atmosphere and the interactions with larger ions. The electrons scatter electromagnetic waves. The radar signal captures turbulence at scales of half the wavelength of the radar (Rapp and Lübken, 2004). These constructive interferences lead to amplified back-scattered power and a narrower peak in the power spectrum compared to scenarios without PMSE. It is worth noting that in ionospheric regions with PMSE, the resulting power spectrum can exhibit both spectral signatures: the broader spectrum associated with regular incoherent scatter signals, as well as the narrower spectrum arising from coherent interferences. Figure 2.6 taken from the study by Rapp and Lübken (2004) shows on the left hand side the incoherent scatter spectrum from 12 February 1987, and on the right hand side coherent-scatter PMSE echoes. Both spectra were plotted using data from the EISCAT VHF radar near Tromsø. One can see that the incoherent scatter spectrum is noticeably wider in frequency compared to the PMSE coherent scatter spectrum which is much narrower.

2.3 Prior Research: Multilayers and Solar Cycle

In this section we will explore the previous research done on similar topics than the topic of this thesis. To do this, we will in particular explore the previous research of PMSE in relation to PMSE monolayers and multilayers as well as

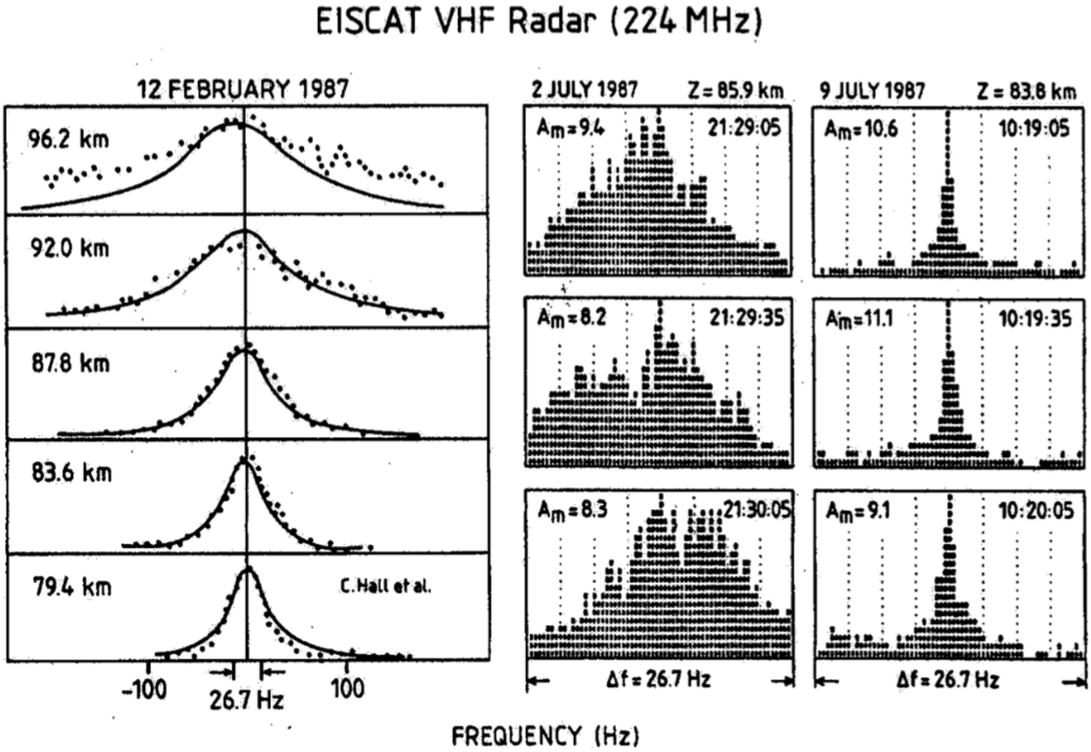

Figure 2.6: Left hand side : incoherent scatter spectrum from 12 February 1987. Altitude varies from 79.4 km to 96.2 km. Right hand side : coherent-scatter PMSE echoes from 2 July 1987 at 85.9 km altitude and from 9 July 1987 at 83.8 km altitude. All the spectra were plotted using data from the EISCAT VHF radar near Tromsø. This figure comes from the study by Rapp and Lübken (2004).

PMSE in relation to the solar cycle.

Previous research about PMSE multilayers

Hoffmann et al. (2005) conducted a study about PMSE layers, investigating their occurrence and mean altitude. To gain further insights, micro-physical model simulations were performed. The findings suggested that the presence of multiple PMSE layers can be primarily attributed to the layering of ice particles resulting from subsequent nucleation cycles. The study reported that monolayers were observed at an average altitude of 84.8 km. When multiple PMSE layers are present, the lower layer tends to occur at an average height of approximately 83.4 km, while the layer above it is typically found at an average height of around 86.3 km. During both solar maximum and minimum periods, monolayers accounted for 50.1% of the PMSE measurements. Double layers had an occurrence of 36.6%, and multilayers with more than 2 layers had an occurrence of 13.3%.

To gain understanding into the formation of PMSE, it can be helpful to comprehend the characteristics of gravity waves and their impact on the neutral atmosphere. In a study conducted by Li et al. (2016), they introduced a two-dimensional theoretical model to investigate the generation process of multi-layered PMSE. The primary focus of their model was to examine how gravity waves produce the movement of ice particles through collisions with the neutral atmosphere. The model assumes that the ice particles are spherical and their size remains constant throughout the simulations, neglecting factors such as growth, sedimentation, or sublimation. In their initial analysis, Li et al. (2016) kept the particle size fixed at 10 nanometers (nm) and varied the vertical wavelength of the gravity waves at 3km, 4km, and 5km. The results revealed a decrease in the number of layers as the vertical wavelength increased, accompanied by an increase in layer thickness. Furthermore, Li et al. (2016) made interesting findings regarding the preferred altitudes associated with multi-layer formations in their study. In fact, they found that specific particles sizes were associated with preferred altitudes. Also, Li et al. (2016) conducted another analysis in which they examined the influence of varying ice particle size while keeping the vertical wavelength of gravity waves fixed at 4 km. They considered particle sizes of 10 nm, 20 nm, and 30 nm and observed that as the particle size increased, the layers exhibited a more rapid decrease in altitude and faced greater challenges in formation. Additionally, once the turbulence subsided, larger ice particles took longer to return to a neutral homogeneous state.

Previous research about PMSE and the solar cycle

Considering the importance of electron density in the formation of PMSE, it is reasonable to anticipate a potential impact of the solar cycle on this phenomenon. While research exploring the relationship between multi-layered PMSE and the solar cycle remains limited, Shucan et al. (2019) identified a positive correlation between the occurrence ratios of PMSE single, double, and triple layers and the K index, which reflects geomagnetic activity and the possibility of particle precipitation. Furthermore, Shucan et al. (2019) noted a negative correlation between the occurrence ratio of PMSE triple layers and the F10.7 flux, which is an indicator for solar activity.

In a previous study by Zhao et al. (2020), a positive relationship between the mesopause temperature and the solar flux at 10.7 cm wavelength (F10.7 flux) was observed. Over an extensive 18-year investigation, they noted a gradual decline in the mesopause temperature (0 to -0.14 K/year), which might have implications for PMSE formation due to the requirement of ice particle formation. Additionally, they identified a decrease in the mesopause height at polar latitudes over time, which could potentially influence the height of PMSE.

In their study, Narayanan et al. (2022) found that there was a clear response in the power of the PMSE echoes during particle precipitation events: in all their cases, an increase in PMSE power was observed in association with particle precipitations. However, Narayanan et al. (2022) say that the particle precipitation does not seem to be related to the very existence of PMSE, and that there seems to be no linear relationship between both. Narayanan et al. (2022) utilized EISCAT VHF data and the Manda experiment, excluding dates when the Heating experiment was active. Their study focused on the 2019 summer season and identified five days, specifically July 15th-17th and August 9th-10th, where both PMSE and particle precipitation were observed simultaneously. To identify the particle precipitation, Narayanan et al. (2022) analyzed electron density measurements between 90 and 95 km, just above the typical altitude range of PMSE occurrence. Their findings suggest that preexisting dormant structures in the region are rapidly transformed into active scatterers by sudden influxes of electrons during particle precipitation events. This may explain the abrupt appearance of PMSE at certain altitudes during such events. Narayanan et al. (2022) note that the lack of a linear relationship between PMSE and particle precipitation may be attributed to variations in the other factors that control PMSE formation, such as the quantity of ice crystals, the extent of dormant structures, and temperature, as previously mentioned.

To explore the presence and layers of PMSE, it's essential to distinguish the PMSE signal from the background in EISCAT VHF radar data. To do this effectively, classification models were used. The following chapter will explain the principles of Linear Discriminant Analysis (LDA) and random forests, which were applied in this thesis.

Chapter 3

Methods for Classification

In order to examine the occurrence and layers of PMSE, it is necessary to separate the PMSE signal from the background in EISCAT VHF radar data. To achieve this, classification models were employed to make the process of analyzing data more efficient and faster. This chapter will describe the working principles of Linear Discriminant Analysis (LDA) and random forests, which were used in this thesis.

3.1 Linear Discriminant Analysis (LDA)

LDA is a method which consists of drawing a linear separation between categories of interest, by maximizing the separability between these known categories, (Hastie et al., 2001a). To better understand LDA, let's assume that we have two categories, ”blue” and ”green”, and that for these categories we use features X and Y to separate the data. LDA uses the information of both categories to create a new projection axis, and it projects the data onto this new axis to maximize the separation of the 2 categories. Figure 3.1(a) shows an example of a depiction of the ”blue” and ”green” categories, and the dashed black line is the corresponding projection axis used for separation.

Let's consider that the ”blue” category has a mean value μ_1 and a covariance Σ_1, and that the ”green” category has a mean value μ_2 and a covariance Σ_2. The separation criterion $J(w)$ is then defined as :

$$J(w) = \frac{w^T S_B w}{w^T S_W w'} \tag{3.1}$$

Where $J(w)$ is the ratio of the between classes and within classes variances. S_B and S_W represent the between class and within class scatter, w is a vector perpendicular to the discriminant plane, and T stands for the transpose. S_B and S_W are defines as follows, (Fisher, 1936) :

$$S_B = (\mu_1 - \mu_2)(\mu_1 - \mu_2)^T \tag{3.2}$$

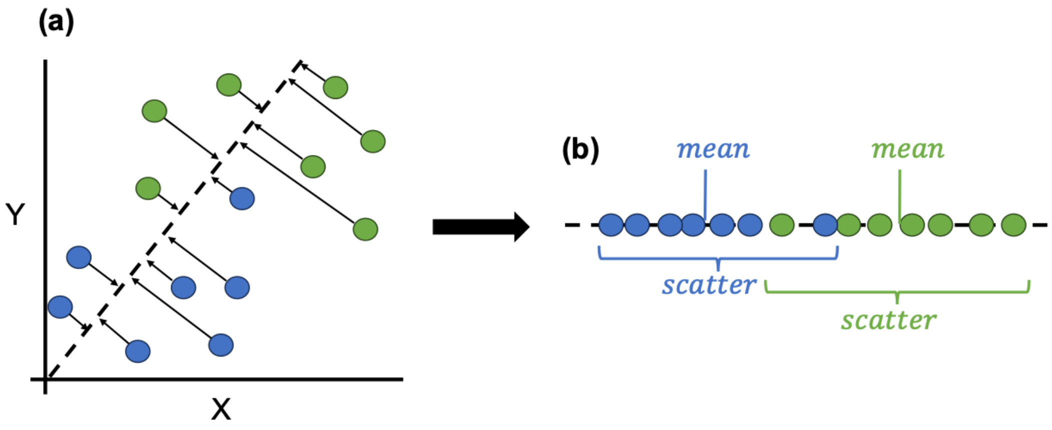

Figure 3.1: Illustration showing an example of separation between 2 categories, namely the ”blue” and the ”green” categories. **(a)** shows the plotted data-set using X and Y as parameters to separate the data. **(b)** shows the data after separation and therefore after projection on the new axis. The black dashed line represents the projection axis.

$$S_W = (\Sigma_1 + \Sigma_2) \tag{3.3}$$

The projection axis is created considering these two criteria as defined in equations 3.2 and 3.3. Equation 3.2 maximizes the distance between the two means. Equation 3.3 minimizes the scatter around the mean of each category. Figure 3.1(b) shows the result of the separation after the projection on the new axis, and it is possible to see the two means of both categories as well as the scatters corresponding to both categories. LDA works well when the class separability is linear (Theodoridis and Koutroumbas, 2006). For further details, please see Theodoridis and Koutroumbas (2006).

3.2 Random forests

A decision tree is a flow chart-like structure where each internal node represents a test on a variable, each branch represents an outcome of the test and each leaf or terminal node represents a class label or predicted value. Figure 3.2 shows an illustration of this chart-like structure. A single decision tree can present some disadvantages in the way that it is not robust to noise in data or could be dependent on a single strong feature (Hastie et al., 2001b). Random forests combine the ease of decision trees with increased flexibility, resulting in improved accuracy.

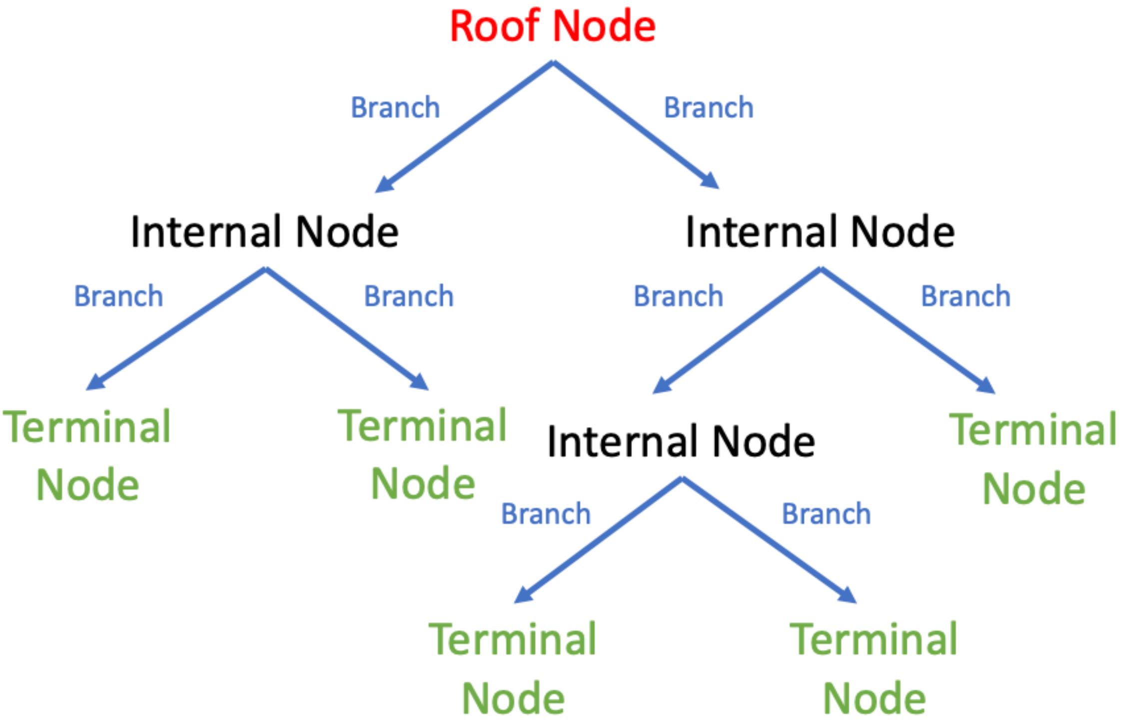

Figure 3.2: Schematic illustration of the flow chart-like structure of a decision tree. The roof node is represented in red, the internal nodes are represented in black, the branches are represented in blue and the terminal nodes, or leaves, are represented in green.

To create a random forest, the first step involves generating a bootstrap data-set. Let's assume a dataset that we want to classify into 3 different categories : ”blue”, ”green” and ”red”. For this, we use 4 variables: A, B, and C and D. To create a bootstrapped data-set, we randomly select samples from the original data-set. A sample can be selected multiple times, while some samples may remain unselected. This process allows for the creation of a diverse set of bootstrapped data-sets that still capture the variability within the original data-set.

Next, we create decision trees using the bootstrapped data-set, but with a random subset of variables at each step. For example, instead of considering all four variables mentioned earlier, let's say we only use two of them. To illustrate, suppose we randomly select B and D as candidate variables to decide the root node of the first decision tree. Let's assume that B separates the samples the most effectively. In the next node of the tree, since B has already been used, it won't be selected again. Instead, we randomly choose two other variables, such as C and D. This process continues until the tree is complete. In our study, we define the number of variables randomly selected at each step as $mtry$. In the study by Probst et al. (2019), it is suggested that $mtry$ for classification should have a default value of $\sqrt{p}$, where p is the total number of features. By using bootstrapped samples and considering only subsets of variables at each step, a diverse set of decision trees are generated. It is this diversity that contributes to the enhanced effectiveness of random forests compared to individual decision trees.

Now that the random forest has been constructed, let's consider a scenario where we encounter new data that the random forest has never encountered before. In this case, we don't have any prior knowledge about the categories the data actually belongs to. We input the first sample into the first decision tree that we created. Let's say the first tree classifies the data as belonging to the "green" category. Then, we input this same sample into the second tree, and so on, until we have gone through all the trees in the random forest. Finally, we examine all the results and gather the votes. We identify the option that received the most votes, and consider it to be the final decision for the category associated with our sample. The process is demonstrated in Figure 3.3, where we substituted our target categories or classes with those used in Paper2. These classes consist of PMSE, background noise, and ionospheric background. The illustration shows three instances of decision trees within the random forest, along with the class they predicted for a specific sample. For this sample, the majority of the trees in the forest classified it as belonging to the PMSE class. We repeat this process for all the samples in the data-set. This aggregation of results by considering the majority vote is known as "bagging," which involves bootstrapping the data and using the collective decisions of the individual trees. In short, when presented with new data, the random forest evaluates it through each decision tree and combines the outcomes to make a final prediction.

As mentioned earlier, there is a portion of the data that was not included in the bootstrapped data-set, known as the out-of-bag (OOB) data. Typically, around one third of the data-set is not selected into the bootstrapped data-set, or we can say that about one third of the data-set forms the OOB data-set. This means that there is a subset of the data for which we already know the outcome, and this data is not utilized during the creation of the random forest. Since the OOB data represents new and unseen samples for the random forest model, it provides an opportunity to evaluate the model's accuracy on unseen data. To do this, we pass all the OOB samples through the forest. The random forest will classify these samples as either correct or incorrect, providing us with valuable insights. The proportion of OOB samples that were incorrectly classified is known as the OOB error. In Paper 2, we used for classification the out-of-bag error rate defined as follows, (Cutler et al., 2012):

$$E_{oob} = \frac{1}{N}\sum_{i=1}^{N}\left(I(y_i \neq \hat{f}_{oob}(x_i))\right), \tag{3.4}$$

It assigns 0 to the OOB error for a correct classification and 1 for an incorrect classification. When we apply these equations to our data, x_i corresponds to a

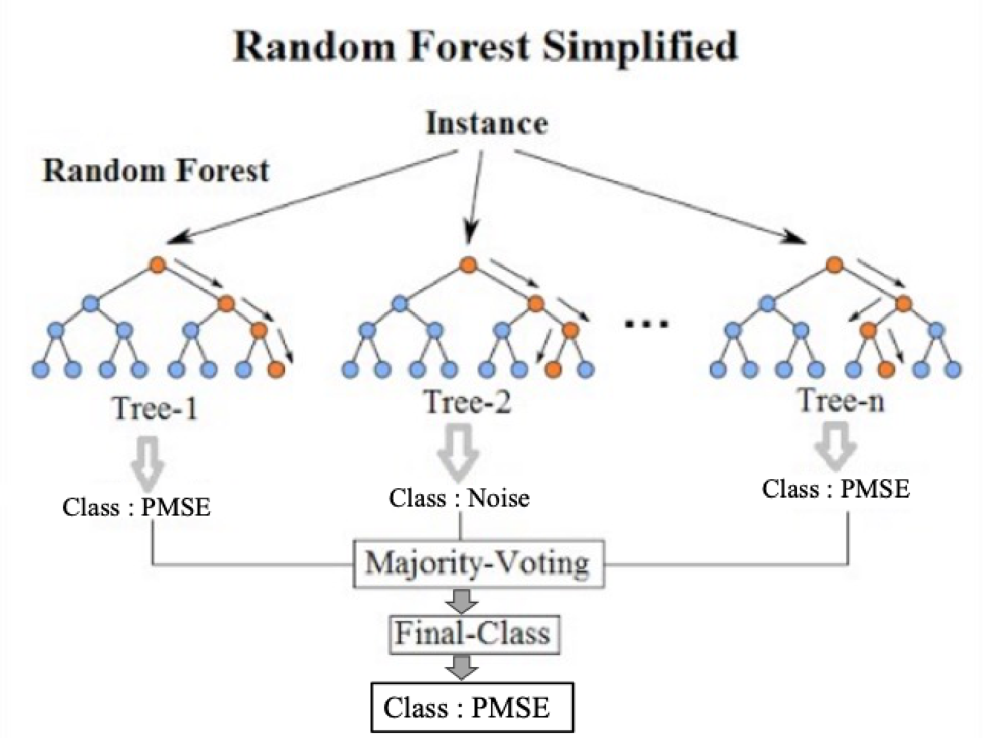

Figure 3.3: Illustration showing an example of a simplified random forest. In this example it is possible to see three examples of decision trees as well as their class predictions. Source of original illustration: Venkata (2021)

given sample i of our data-set, $\hat{f}_{oob}(x_i)$ is the out-of-bag prediction for bootstrap sample i, while y_i is the actual label of this sample, (Cutler et al., 2012), and N is the number of samples. Finally, $I(y_i \neq \hat{f}_{oob}(x_i))$ is a measure of how close y_i is to $\hat{f}_{oob}(x_i)$. It is a loss function defined to minimize the expected value of the loss.

For fine tuning a random forests model, we can experiment with adjusting the value of $mtry$ and observe how it affects the OOB error. Alternatively, we can also increase the number of trees in the forest, (Probst et al., 2019),(Grömping, 2009)

The findings of the second paper indicate that extracting the PMSE signal from the surrounding data is indeed feasible. This serves as a basis for the next chapter, where we apply the classification model to EISCAT VHF radar data.

Chapter 4

Investigation of PMSE multilayers

This chapter provides an overview of the EISCAT radar data utilized across all research papers. Then, an examination of the application of Linear Discriminant Analysis to PMSE will follow, as detailed in the first paper. Next, the segmentation of PMSE using random forest algorithms, as explored in the second paper, is discussed. Finally, the investigation of PMSE multilayers during both solar maximum and solar minimum, as presented in the third paper, is reviewed. Key findings from each study are summarized.

4.1 The radar : EISCAT VHF

For this study, data from the EISCAT VHF radar was used, operating at 224 MHz, located near Tromsø. This radar is particularly interesting to use in the scope of PMSE investigation. In fact, EISCAT VHF is a radar designed to measure incoherent scatter and not only provides information about the echo power at PMSE altitudes, but it also provides information about the ionisation levels above the PMSE, such as electron density information. As a comparison, typical MST radars observe the PMSE, but not incoherent scatter which allows to derive electron densities. Relevant features of the EISCAT VHF radar are listed in Table 4.1. The electron density parameter given by analyzing the scattered radar signal is proportional to the received back-scattered power, and therefore the strength of the PMSE. The EISCAT VHF radar utilizes many different experimental modes to collect data. The utilized pulse coding for the PMSE measurements we analyzed is referred to as ‘Manda’. The Manda code is specifically optimized for high-resolution measurements at altitudes corresponding to the D-region of the atmosphere, making it particularly well-suited for investigating PMSE layers within this region.

4.2 Application of LDA to PMSE

In this section, the application of LDA to PMSE for classification of PMSE and non-PMSE image data, which was the focus of the first paper, will be examined. In this study, a set of images containing PMSE and non-PMSE instances

Table 4.1: Relevant characteristics of the EISCAT VHF radar used in all three papers. More information about the EISCAT documentation and radar system parameters can be found on the EISCAT Scientific Association website.

EISCAT VHF parameters	
Frequency	223.4 MHz
Wavelength	1.34 m
Bragg scale	0.67 m
Peak power	1.2 MW
Transmitted pulse scheme	Manda v 4.0
Interpulse period	1.5 ms
Time resolution	4.8 s
Range resolution	360 m
Spectral resolution	2.6 Hz
Antenna Elevation	90 deg, zenith

were carefully selected. Initially, the data, which represents the back-scattered power per cubic meter, was normalized in the range [0,255]. In this grayscale representation, 0 indicated black pixels and 255 represented white pixels. Subsequently, the grayscale distributions of several image samples were plotted, targeting three specific regions of interest. A simplified example of such an image samples can be seen in Figure 4.1, as well as their corresponding grayscale distributions. The three regions of interest are respectively the PMSE, the ionospheric background and the background noise regions.

Based on the differences in the distributions, one can intuitively perceive that utilizing criteria such as mean or standard deviation could likely lead to successful separation of the data. By considering parameters like mean, standard deviation, skewness, and kurtosis of the samples, the image samples were classified into three distinct categories. The results indicate an accuracy of approximately 98 percent in distinguishing PMSE regions from the ionosphere and noise. A simplified example of this process is depicted in Figure 4.1(c), illustrating a two-dimensional separation of the data using mean and standard deviation as the criteria for separation. LDA involves drawing a linear separation between all three categories to optimize their distinction. The focus of LDA is to maximize separability among known categories. In the provided example (Figure 4.1(c)), one can observe that when employing only mean and standard deviation as the separating criteria, a majority of the samples are correctly classified into their respective categories. These misclassifications are discussed in more detail in Paper 1.

In this study, the main objective was to assess the feasibility of distinguishing

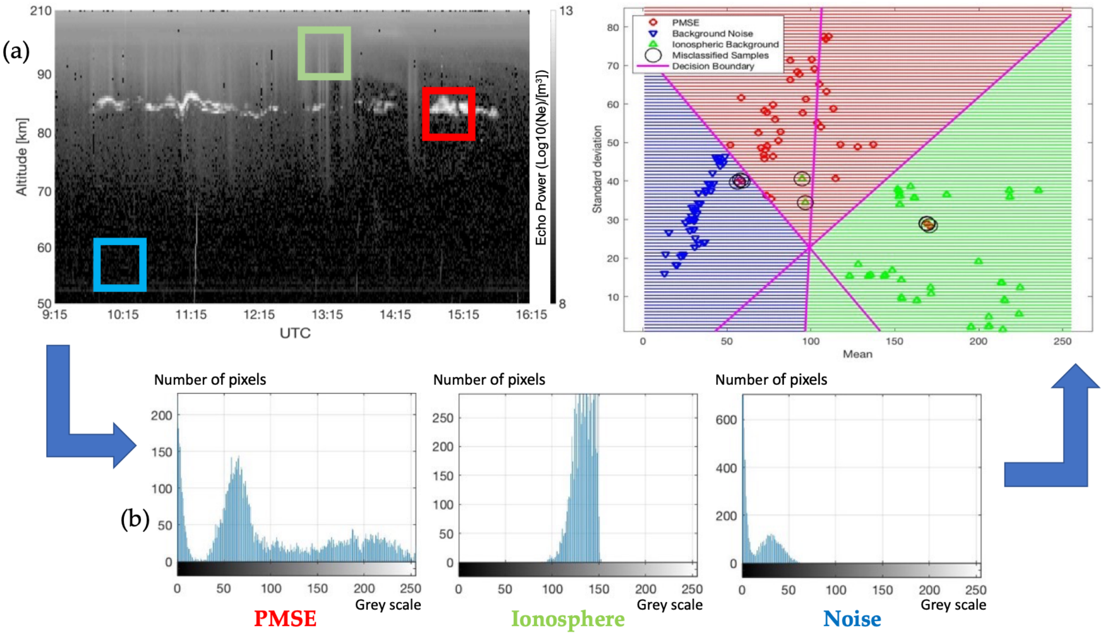

Figure 4.1: Simplified example of using LDA in the first paper to serapate the data. **(a)** shows an image containing the 3 regions of interest where the red, green and blue windows respectively correspond to the PMSE, Ionospheric background, and background noise. The corresponding grey scale distributions can be seen in image **(b)** Then, LDA is performed on the dataset and one can see the linear separations in pink color in image **(c)**. Here, the accuracy of the separation is 93.94. This figure is adapted from the study from Jozwicki et al. (2021).

images containing PMSE from other images using a simple machine learning method and a basic set of parameters. **The results of this paper reveal two findings.** Firstly, it is indeed possible to differentiate images that include PMSE from the remaining samples. Secondly, we can also determine that the remaining images correspond to either ionospheric background or background noise. These findings emphasize that LDA based approach can be used for classification of images into the three categories. Based on these results, segmenting the PMSE signal at pixel level from the rest of the data using random forests was focused on.

4.3 Segmenting PMSE using Random Forests

In this section, the segmentation of PMSE using random forests, which is the objective of the second paper, is discussed. It's purpose is to extend the work in Paper 1 by extracting the PMSE from the data through segmentation at pixel level. To accomplish this, random forests were employed. The process involved manually labeling the image data and assigning it to one of three categories: PMSE, ionospheric background, and background noise. Eighteen images out of the 30 were partially labeled, which corresponds to a total of 56250 samples (pixels). Sixty percent of the labeled data was used for training (33750 samples) and 40 percent for quantitative testing (22500 samples). The labels have been made publicly available on the DataverseNO database for easy access. For qualitative testing, all the images were used. In addition, qualitative analysis was done by visual inspection of the segmented images by a domain expert.

For random forests, a set of simple features was used. The various features were calculated for each pixel. These features include the: altitude derivative, time derivative, mean, standard deviation, median, minimum, and maximum within neighborhood sizes ranging from 3 by 3 to 11 by 11 pixels, centered around the respective pixel. The amplitude and altitude were additionally used as features. This generates a feature vector with 35 dimensions. It is worth noting that horizontal gradient operators calculate the time derivatives, and that vertical gradient operators calculate the altitude derivatives.

In this study, using quantitative testing, the best results in terms of classification error and OOB classification error are achieved when using a 7x7 filter size with an $mtry$ value of 9 and an 11x11 filter size with an $mtry$ value of 6, while considering weighted-down labels. On the other hand, the worst performance was observed when using all filter sizes with an $mtry$ value of 5, as well as the combination of a 9x9 filter size with an $mtry$ value of 3. For qualitative analysis, the 7x7 filter size with $mtry$ value of 9 was selected. A total of 30 images were used for the classification model, with 12 of them being new data. Figure 4.2(b) displays the predicted labels from the classification model using the 7x7 filter size and $mtry$ value of 9. The model's prediction of PMSE labels appears to be poor, indicating that altitude has a clear dominance over other features in predicting the labels.

For qualitative testing, the predicted labels were generated for all the 30 test images and for all the possible combinations of filter sizes and $mtry$ values. Although in the quantitative testing of the study by Jozwicki et al. (2022), the different metrics used to evaluate the performance of the random forest are the worst for the combination of all filter sizes with $mtry = 5$, this combination gave the best qualitative results for all the 30 images. Figure 4.2(c) illustrates the qualitative analysis for the 30 June 2008, showing the predicted labels that were observed with all filter sizes and $mtry = 5$.

The findings of the second paper indicate that extracting the PMSE signal from the surrounding data is indeed feasible. This serves as a basis for the next study, where we apply the classification model to EISCAT VHF radar data to investigate PMSE multilayers during solar maximum and solar minimum.

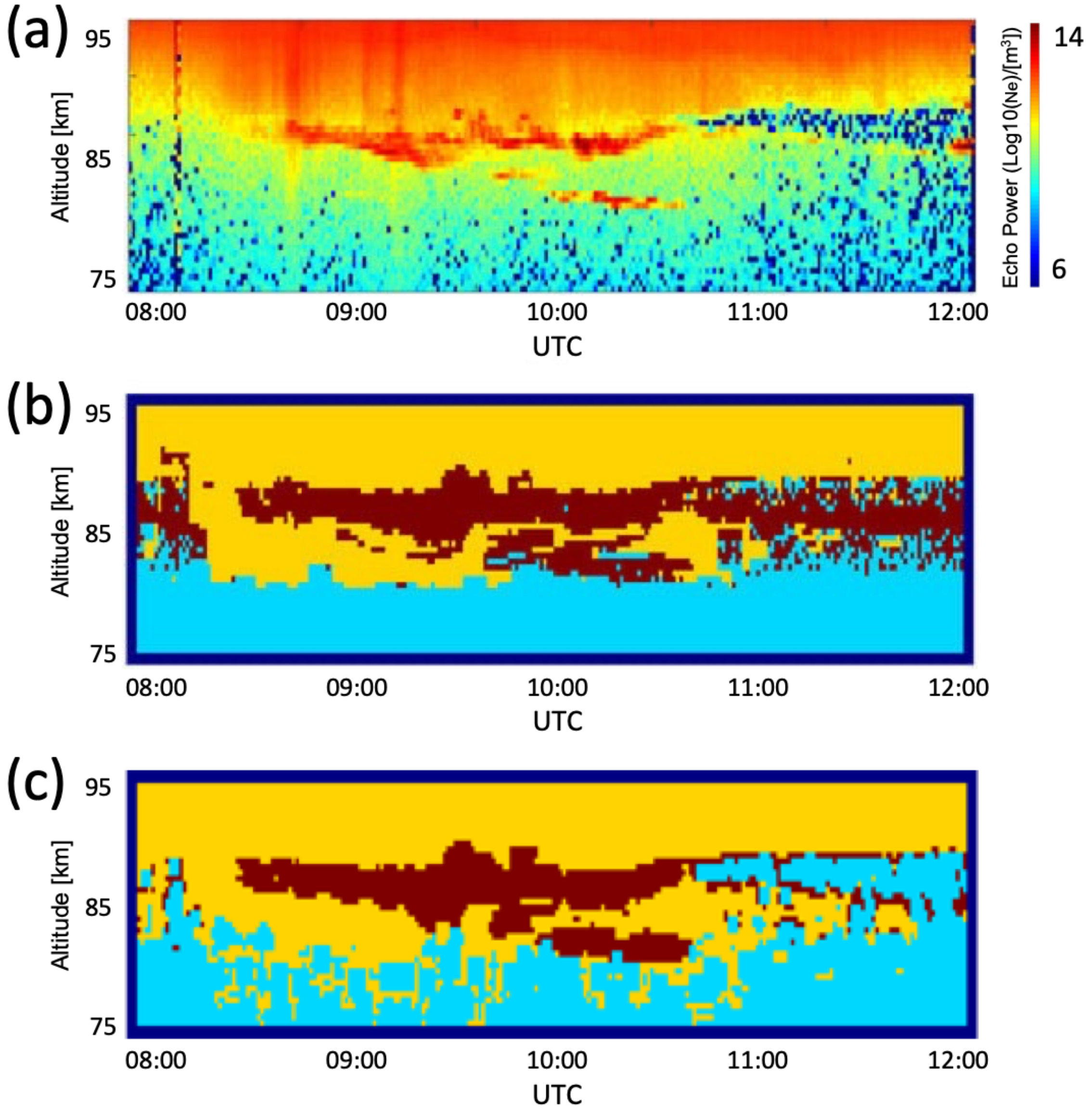

Figure 4.2: Illustration showing an example of results of segmentation using the random forests method. **(a)** shows a plot of the actual data from the 30 June 2008 where the color scale represents the echo power to the power of 10, per cubic meter. **(b)** shows the predicted labels using the 7x7 filter size, weighted-down labels, and $mtry = 9$. **(c)** shows the predicted labels using all filter sizes, weighted-down labels, and $mtry = 5$. Both images **(b)** and **(c)** represents the predicted labels where yellow, cyan and dark red represents respectively the the region of the image labeled as Ionospheric background, Background noise, and PMSE. The horizontal axis on both images represents the time which starts at 8:00 UTC and finishes at 12:00 UTC. The vertical axis represents the altitude which ranges from 75 km to 95 km. Figure adapted from the study by Jozwicki et al. (2022)

4.4 PMSE multilayers during Solar Maximum and Solar Minimum

This section focuses on the third and final paper, along with additional statistical analyses performed to validate its findings. The first subsection will cover the statistical tests used for validation, specifically the t-test and ANOVA, and will include a comparison and discussion of selected cases. The second subsection will discuss the data preprocessing steps, such as data selection and preparation. In the third subsection, the main results of Paper 3 will be presented, together with a discussion comparing its findings to those of other works, followed by a sub-subsection highlighting the key findings of the paper.

T-test and ANOVA

In the third paper, findings are initially confirmed employing the commonly used p-values derived from the statistical t-test. The p-value serves as a statistical measure to assess the significance of results or values. If the p-value is less than 0.05, it is typically considered statistically significant. However, for enhanced accuracy, this thesis re-evaluates all results from Paper 3 using Analysis of Variance (ANOVA). It was found that utilizing t-test p-values with a threshold of 0.0001 provides at least comparable accuracy to ANOVA p-values with the conventional threshold of 0.05. In the following paragraphs, several cases will be presented and compared. Then, later, when discussing the results of Paper 3, only those meeting the stricter threshold will be considered (0.0001 for t-test p-values and 0.05 for ANOVA p-values).

Similar trends are observed across all cases, including solar minimum, solar maximum, separated mono and multilayers, and all layers combined, when applying ANOVA with a threshold of 0.05 and t-test p-values with a significance threshold of 0.0001. Figure 4.3 and Figure 4.4 illustrate the altitude distribution of the data during solar maximum and solar minimum respectively, with different panels corresponding to varying numbers of layers, and Tables 4.2 and 4.3 show the T-test and ANOVA p-values corresponding to all the layer combinations in these figures. In a similar way, Tables 4.4 and 4.5 show the T-test and ANOVA p-values corresponding to all the possible combinations of different sets of multilayers for all the investigated parameters: electron density, echo power, thickness and altitude. In Table 4.3 and Table 4.5, values highlighted in red denote instances where the ANOVA p-value exceeds the 0.05 threshold, which consistently corresponds to red-highlighted t-test p-values in Table 4.2 and Table 4.4. Conversely, in Table 4.2 and Table 4.4, values highlighted in orange represent the few instances where layers are considered statistically significant by ANOVA (p-value below 0.05) but not by the t-test (p-value above 0.0001). In conclusion, using t-test p-values with a threshold of 0.0001 is at least as effective as using ANOVA with the conventional threshold of 0.05.

When evaluating the statistical significance, shown in Table 4.3 and Table 4.2, of the altitude distribution of the mono and multilayers shown in Figure 4.3 and Figure 4.4, it is crucial to recognize that the primary concern is the statistical significance of multilayers within the same group, regardless of whether we use the t-test or ANOVA. For instance, it is important that layers 1 of 4, 2 of 4, 3 of 4, and 4 of 4 are statistically significant, indicating sufficient differences within the group. Conversely, the significance of layers such as 1 of 2

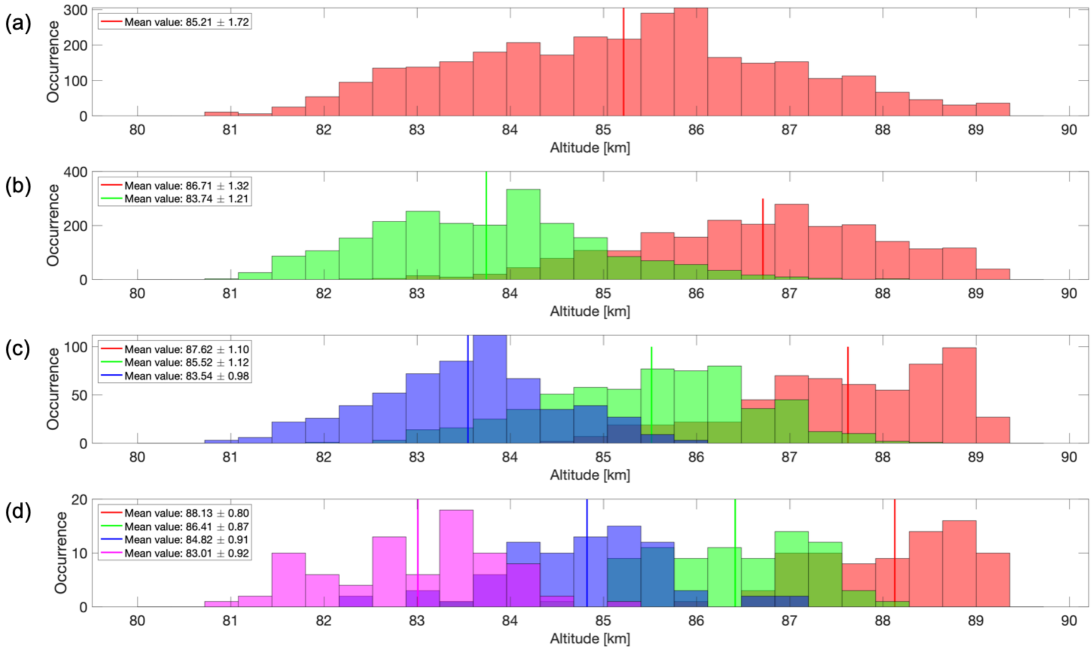

Figure 4.3: Altitude distribution of the data during solar maximum for **(a)** mono layers, **(b)** multi layers with 2 layers, **(c)** multi layers with 3 layers, and **(d)** multi layers with 4 layers. In each figure, the color scheme of the distributions indicates altitude order: red for the highest layer, green for the second highest, blue for the third highest, and magenta for the fourth highest. Intermediate colors represent overlapping altitude distributions. The legend displays the mean value and one standard deviation for each distribution.

Table 4.2: T-test P-Values for all combinations of layers during solar maximum and solar minimum of the altitude distribution of all the mono and multilayers shown in Fig. 4.3 and Fig. 4.4.

T-TEST		**Solar Minimum**									
		Mono Layers	Layers 1 of 2	Layers 2 of 2	Layers 1 of 3	Layers 2 of 3	Layers 3 of 3	Layers 1 of 4	Layers 2 of 4	Layers 3 of 4	Layers 4 of 4
Solar Maximum	Mono Layers		P <0.0001	P <0.0001	P <0.0001	0.3618	P <0.0001	P <0.0001	P <0.0001	0.0027	P <0.0001
	Layers 1 of 2	P <0.0001		P <0.0001	P <0.0001	P <0.0001	P <0.0001	P <0.0001	0.0268	P <0.0001	P <0.0001
	Layers 2 of 2	P <0.0001	P <0.0001		P <0.0001	P <0.0001	P <0.0001	P <0.0001	P <0.0001	P <0.0001	P <0.0001
	Layers 1 of 3	P <0.0001	P <0.0001	P <0.0001		P <0.0001	P <0.0001	0.0106	P <0.0001	P <0.0001	P <0.0001
	Layers 2 of 3	P <0.0001	P <0.0001	P <0.0001	P <0.0001		P <0.0001	P <0.0001	P <0.0001	P <0.0001	P <0.0001
	Layers 3 of 3	P <0.0001	P <0.0001	0.0002	P <0.0001	P <0.0001		P <0.0001	P <0.0001	P <0.0001	0.0001
	Layers 1 of 4	P <0.0001	P <0.0001	P <0.0001	0.0001	P <0.0001	P <0.0001		P <0.0001	P <0.0001	P <0.0001
	Layers 2 of 4	P <0.0001	0.0448	P <0.0001	P <0.0001	P <0.0001	P <0.0001	P <0.0001		P <0.0001	P <0.0001
	Layers 3 of 4	0.0411	P <0.0001	P <0.0001	P <0.0001	P <0.0001	P <0.0001	P <0.0001	P <0.0001		P <0.0001
	Layers 4 of 4	P <0.0001	P <0.0001	P <0.0001	P <0.0001	P <0.0001	P <0.0001	P <0.0001	P <0.0001	P <0.0001	

and 2 of 3 is less relevant. Notably, if two layers are not judged statistically significant by the ANOVA statistical test, as seen in Table 4.2 in the case of solar minimum for layers 3 of 3 and 4 of 4 (which are the last and lowermost layers of each group of multilayers), this lack of significance might suggest similarity between the layers. Interestingly, these layers coincide with the altitude of the NLC layers as reported by Fiedler et al. (2003) indicating that valuable information can be extracted even from non-significant values. Hence, while ANOVA and t-test are important, it is essential to carefully investigate the underlying data beyond mere statistical tests.

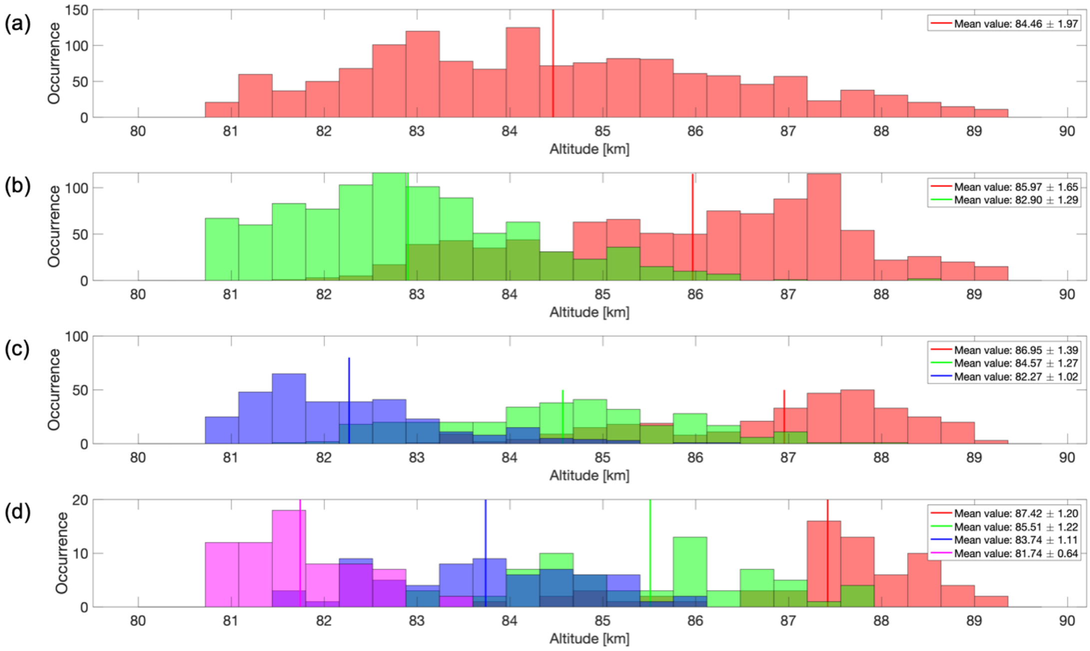

Figure 4.4: Altitude distribution of the data during solar minimum for **(a)** mono layers, **(b)** multi layers with 2 layers, **(c)** multi layers with 3 layers, and **(d)** multi layers with 4 layers. In each figure, the color scheme of the distributions indicates altitude order: red for the highest layer, green for the second highest, blue for the third highest, and magenta for the fourth highest. Intermediate colors represent overlapping altitude distributions. The legend displays the mean value and one standard deviation for each distribution.

Table 4.3: ANOVA P-Values for all combinations of layers during solar maximum and solar minimum of the altitude distribution of all the mono and multilayers shown in Fig. 4.3 and Fig. 4.4.

ANOVA		**Solar Minimum**									
		Mono Layers	Layers 1 of 2	Layers 2 of 2	Layers 1 of 3	Layers 2 of 3	Layers 3 of 3	Layers 1 of 4	Layers 2 of 4	Layers 3 of 4	Layers 4 of 4
Solar Maximum	Mono Layers		P=0	P=0	P=0	P=0.9875	P=0	P=0	P=5.4033e-06	P=0.0090	P=0
	Layers 1 of 2	P=0		P=0	P=0	P=0	P=0	P=1.2553e-11	P=0.4044	P=0	P=0
	Layers 2 of 2	P=0	P=0		P=0	P=0	P=2.0751e-08	P=0	P=0	P=0.0012	P=3.1852e-07
	Layers 1 of 3	P=0	P=0	P=0		P=0	P=0	P=0.4573	P=4.1542e-10	P=0	P=0
	Layers 2 of 3	P=4.6858e-05	P=0	P=0	P=0		P=0	P=0	P=3.7504e-04	P=0.0036	P=0
	Layers 3 of 3	P=0	P=0	P=0.0627	P=0	P=0		P=0	P=0	P=1.5944e-10	P=0.2801
	Layers 1 of 4	P=0	P=7.7069e-19	P=0	P=0.0675	P=0	P=0		P=1.0594e-10	P=0	P=0
	Layers 2 of 4	P=3.6118e-13	P=0.6698	P=0	P=4.7010e-12	P=2.0783e-06	P=0	P=7.4272e-14		P=3.4488e-09	P=0
	Layers 3 of 4	P=0.2608	P=0	P=1.8060e-10	P=0	P=9.6477e-04	P=1.3656e-13	P=0	P=8.2703e-12		P=9.0717e-12
	Layers 4 of 4	P=0	P=0	P=1.2174e-04	P=0	P=0	P=0.0356	P=0	P=0	P=9.0322e-16	

Now that the statistical significance has been addressed, the focus will shift to discussing the content of Paper 3 including the selection and pre-processing steps of the data, followed by the results of Paper 3.

Data pre-processing

In the third paper, the classification model that resulted from the previous study was applied to EISCAT VHF data. To conduct this study, data was obtained by downloading over 230 hours of recorded data from the Magridal website, resulting in a total of 17,930 data points.

Table 4.4: T-test p-values for all layer combinations during solar maximum (top panel) and solar minimum (middle panel). The bottom panel, labeled ”Sol Max.-Min.,” shows p-values comparing solar maximum and solar minimum for all layers combined. The four investigated parameters—electron density, echo power, layer thickness, and altitude distribution—are displayed across four columns. Altitude distribution data for solar maximum and minimum is omitted here, as it is detailed in Table 4.2

T-TEST		Electron Density	Echo Power	Thickness	
Solar Maximum	Layers 1-2	P <0.0001	P <0.0001	P <0.0001	
	Layers 1-3	P = 0.0003	P <0.0001	P <0.0001	
	Layers 1-4	P = 0.0831	P <0.0001	P <0.0001	
	Layers 2-3	P = 0.0804	P <0.0001	P <0.0001	
	Layers 2-4	P = 0.4000	P <0.0001	P <0.0001	
	Layers 3-4	P = 1.0000	P = 0.0012	P = 0.0002	
Solar Minimum	Layers 1-2	P <0.0001	P = 0.3483	P <0.0001	
	Layers 1-3	P <0.0001	P = 0.0009	P <0.0001	
	Layers 1-4	P <0.0001	P = 0.0001	P <0.0001	
	Layers 2-3	P <0.0001	P <0.0001	P <0.0001	
	Layers 2-4	P = 0.0091	P <0.0001	P <0.0001	
	Layers 3-4	P = 0.5707	P = 0.0728	P = 0.0002	Altitude
	Sol Max. - Min.	P <0.0001	P <0.0001	P <0.0001	P <0.0001

Table 4.5: ANOVA p-values for all layer combinations during solar maximum (top panel) and solar minimum (middle panel). The bottom panel, labeled ”Sol Max.-Min.,” shows p-values comparing solar maximum and solar minimum for all layers combined. The four investigated parameters—electron density, echo power, layer thickness, and altitude distribution—are displayed across four columns. Altitude distribution data for solar maximum and minimum is omitted here, as it is detailed in Table 4.3

ANOVA		Electron Density	Echo Power	Thickness	
Solar Maximum	Layers 1-2	P=1.3592e-10	P=1.4774e-14	P=0	
	Layers 1-3	P=2.1418e-04	P=0	P=0	
	Layers 1-4	P=0.1633	P=4.8691e-20	P=0	
	Layers 2-3	P=0.6188	P=1.2049e-09	P=1.8824e-21	
	Layers 2-4	P=0.9258	P=5.4994e-09	P=3.0912e-11	
	Layers 3-4	P=1.0000	P=0.0202	P=0.1314	
Solar Minimum	Layers 1-2	P=0	P=0.5867	P=1.4573e-07	
	Layers 1-3	P=0	P=0.0056	P=1.7687e-20	
	Layers 1-4	P=8.5420e-24	P=0.0013	P=9.4490e-17	
	Layers 2-3	P=8.1763e-06	P=2.4717e-05	P=9.7436e-06	
	Layers 2-4	P=0.0349	P=5.3577e-05	P=1.3591e-07	
	Layers 3-4	P=0.9981	P=0.3922	P=0.0514	Altitude
	Sol Max. - Min.	P=0	P=0	P=0	P=0

Typically, researchers employ a threshold on the echo power to pre-select PMSE data. However, this conventional method has certain drawbacks. While it is true that PMSE signals often exhibit higher back-scattered powers (referred to as echo power), there are instances where PMSE signals may have lower back-scattered powers. By using the traditional approach with a high echo power threshold, there is a risk of excluding these faint PMSE signals from the dataset, thereby losing valuable information and limiting the scope of PMSE analysis. This concern is particularly significant, as we will later discuss regarding the results of Paper 3, and see that an increase in the number of multilayers seems to result in decreased backscattered power within each individual layer. Consequently, monolayers generally exhibit the highest backscattered power, while multilayers tend to show lower backscattered powers. Therefore, retaining as many PMSE events as possible, including the faint ones, is crucial for a comprehensive understanding of the phenomenon of PMSE multi-layering.

In this study, the classification model served as a pre-selection tool, allowing a lower echo power threshold to be applied to the output of the pre-selected data. An example of raw data from 16 July 2015 is displayed in Figure 4.5(a). Figure 4.5(b) illustrates the data classified into three categories according to the output of the classification model, where the dark red color indicates data classified as PMSE. Subsequently, an echo power threshold is applied to the data classified as PMSE in Figure 4.5(b), resulting in Figure 4.5(c). This step effectively removes the non-PMSE data that may still remain after the classification model. Finally, the start and end of each PMSE layer are detected, as shown in Figure 4.5(d). The threshold technique without the initial classification filtering is also employed in other layer detection studies by Hoffmann et al. (2005), Rauf et al. (2018), and Shucan et al. (2019). In this approach, a layer commences whenever the echo power exceeds a predefined threshold, and it ends when the echo power drops below the specified threshold. Thanks to the use of a classification model in this thesis, this threshold could be lowered to $N_e > 3.2 \times 10^{10} m^{-3}$, which is equivalent to 10.5 in base 10 logarithmic units of the number of electrons per cubic meter. Consequently, this lower threshold ensured the inclusion of a larger amount of data, including faint PMSE signals. In comparison, other studies that do not utilize a classification model often employ higher thresholds, such as $N_e > 4.6 \times 10^{11} m^{-3}$ in the study by Rauf et al. (2018), or $N_e > 2.6 \times 10^{11} m^{-3}$ in the study by Shucan et al. (2019).

This is particularly crucial for the analysis of PMSE multilayers, as these layers do not consistently exhibit high echo powers. For example, in Figure 2.5, the red frame illustrates three layers, but only the lowermost layer demonstrates a significantly high echo power. The other two layers exhibit relatively low echo powers, which can be comparable to the back-scattered powers observed in the ionospheric background region. Consequently, employing the conventional method with a high echo power threshold would likely result in the exclusion of two out of three layers. Entire PMSE layers could be completely overlooked.

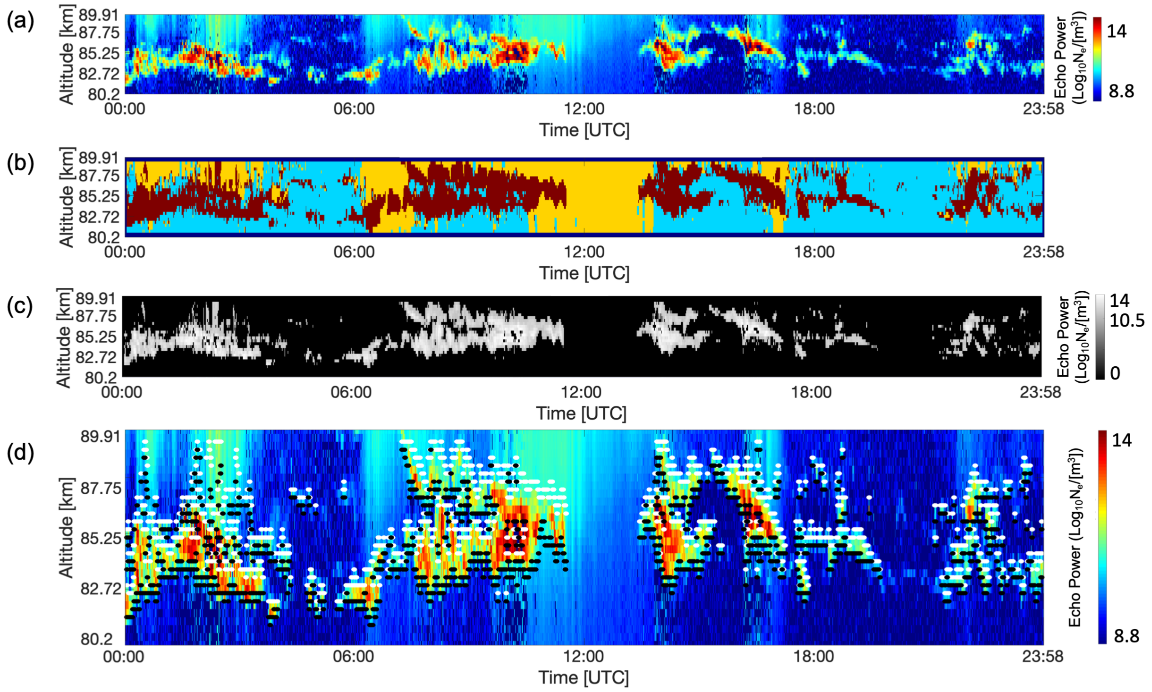

Figure 4.5: Figure illustrating the process of the layer detection. **(a)** shows the original data for the 16 July 2015 between 00:00 and 23:58. **(b)** shows the output from the classification model used from Jozwicki et al. (2022). Dark red represents areas labeled as PMSE, cyan represents areas of the data labeled as background noise and yellow represents areas labeled as ionospheric background. **(c)** represents the data labeled as PMSE in dark red from sub Figure 4.5 **(b)**, onto which an echo power threshold ($N_e > 3.2 \times 10^{10} m^{-3}$) was applied to make sure only PMSE data were left. Finally, **(d)** represents the detected beginning and end of layers respectively represented with white and black points, overlayed on the original data.

Therefore, this study allows for a more detailed analysis of PMSE. The approach enables the examination of the number of PMSE layers as well as their thickness, which was more challenging using previous methods. The echo power in the layers and the electron density at 92 km altitude is also investigated. Furthermore, the investigation of PMSE monolayers and multilayers in relation to the solar cycle was conducted. The selected dataset exclusively comprised data corresponding to either a solar maximum or a solar minimum. To investigate the influence of the solar cycle on PMSE monolayers and multilayers, dates from the most recent available solar maximum and minimum were selected, carefully avoiding times when the Heating experiment was running. The solar maximum phase of a solar cycle is characterized by an increased sunspot number and higher levels of ultraviolet radiation. The F10.7 cm flux is commonly used as a proxy for the amount of ultraviolet radiation, and therefore as a proxy for the level of solar activity. Figure 4.6 shows the monthly evolution of the smoothed sunspot number in blue, and the smoothed F10.7 cm flux in orange over the years 2005 to 2022. The time frames for data selection in Paper 3 are highlighted by the black frames. Further details of the data can be found in Table 1 of Paper 3. The utilization of EISCAT VHF data facilitated a direct comparison between the echo powers observed during PMSE events and the electron densities at ionospheric altitudes above the PMSE. In the following section, the results of Paper 3 will be presented, followed by a summary highlighting the key findings.

Results and Comparative Discussion

The results of the study conducted in Paper 3 suggest that on average, during solar maximum, PMSE layers exhibit higher altitude, echo power, and thickness compared to solar minimum. The electron density at 92 km, which is typically higher during solar maximum, also reflects this trend.

An analysis of individual layers within multilayer sets shows a consistent pattern: both during solar maximum and minimum, the altitude of the top layer increases with the number of multilayers. This trend can be seen in Figure 4.3 and Figure 4.4. This trend is also observed in the second and third highest layers.

The results of Paper 3 also support the conclusions drawn by Hoffmann et al. (2005) regarding the altitude and occurrence rate of both PMSE monolayers and multilayers. Additionally, the lowest layer in various multilayer sets generally corresponds with the NLC altitude of 83.3 km as reported by Fiedler et al. (2003) (cf. Figure 4.3 and Figure 4.4).

The study conducted by Vellalassery et al. (2024) investigates the variation of NLC across the solar cycle. By employing the Leibniz Institute Middle Atmosphere (LIMA) model and the Mesospheric Ice Microphysics and Transport (MIMAS) model, the study examines data from 1849 to 2019, encompassing 15 solar cycles. Their research reveals that NLC altitudes rise during solar maximum phases and fall during solar minimum phases. Additionally, a long-term decrease in NLC altitude was noted, attributed to the overall shrinking of the atmosphere. The results of Paper 3 corroborate these findings, as lower altitudes of the PMSE were observed during the solar minimum period (2019 and 2020) compared to the solar maximum period (2013 to 2015).

Another finding presented in Paper 3 is the observation that the thickness of PMSE layers decreases as the number of multilayers increases. This means that a single mono-layer tends to be thicker than layers in a two-layer set, which in turn are thicker than those in a three-layer set, and so on. This pattern is particularly evident for the first three layers during both solar maximum and minimum. Additionally, echo power decreases with more multilayers, but this trend is noticeable only during solar maximum, mainly affecting the first three layers. This suggests a possible relationship between the number of layers, echo power, and thickness.

These results align with those of Li et al. (2016), who found that the thickness of multilayers decreases as the number of layers increases. In fact, Li et al. (2016) observed that an increase in vertical wavelength of gravity waves corresponded to a decrease in the number of layers, while the thickness of the remaining layers increased. However, in their 2D model, Li et al. (2016) only considered one vertical wavelength of gravity waves and kept the particle size constant when varying the vertical wavelength. In reality, there can be different particle sizes at a given altitude, and gravity waves may also have varying wavelengths. Hence, the relationship between gravity waves and PMSE multilayer thickness and number is not as simple or direct. The findings of Li et al. (2016) also indicated that the formation of multilayer structures in their model exhibited preferred altitudes, which were influenced by the size of the ice particles. Additionally, they found that larger particles contributed to a more rapid decline in layer altitude and a slower formation process. Determining whether the thinner appearance of layers is solely due to reduced echo power is challenging. Even when looking at the raw data without applying any thresholds, mono layers consistently appear thicker and exhibit stronger echo power. Our segmentation method, combined with the thresholding process, accurately reflects this observation. Figure 2.4, for instance, illustrates this phenomenon: when several multilayers merge into a single monolayer between 06:00 UTC and 12:00 UTC, both the thickness and echo power increase. By comparing the results from Paper 3 with Li et al. (2016), a hypothesis was formulated that suggests a potential relationship between layer thickness and the vertical wavelength of gravity waves. It might be interesting to consider that longer wavelengths of gravity waves potentially result in thicker layers. Further investigations could explore this hypothesis and potentially utilize PMSE observations at these altitudes to infer the wavelength of gravity waves.

Results indicates a positive correlation between electron density at 92 km and layer thickness across all layers and solar conditions, except in the case of four multilayers during solar minimum. A similar correlation was also observed between electron density and echo power, especially for mono layers and during solar maximum, as noted by Rauf et al. (2018). This suggests that under these conditions, higher ionization levels at 92 km altitude could result in stronger PMSE, reflected in higher echo power. The correlation between electron density and layer thickness is high, except for sets of 4 multilayers during solar minimum. This correlation was highest for solar maximum and mono layers, indicating that thicker mono layers are common at higher ionization levels. Comparing the results with Li et al. (2016) suggests a hypothetical link between layer thickness and the vertical wavelength of gravity waves, where larger wavelengths could lead to thicker layers. Future research could explore this hypothesis further, possibly enabling the inference of gravity wave wavelengths from PMSE observations.

It remains challenging to determine whether the results presented here align with the hypothesis by Li et al. (2016) that gravity waves are the causal agent for PMSE, or if they support the counterargument proposed by Wilms et al. (2013). It is well established that both NLC and PMSE require the presence of ice particles to exist. Li et al. (2016) demonstrated a relationship between the vertical wavelength of gravity waves and the number and width of PMSE multilayers. Conversely, Wilms et al. (2013) argued that NLC do not depend on gravity waves for their formation. It is essential to remember that, despite their similarities, PMSE and NLC are distinct phenomena. NLC are visible to the naked eye and do not require radar for observation, whereas PMSE are detected only by radar. For PMSE detection, ice particles must be charged, and free electrons must be present at these altitudes, as the incoherent scatter radar detects the electrons. Additionally, the ice particles must be structured at the Bragg wavelengths of the radar. Gravity wave breaking can induce turbulence at mesopause altitudes, which can organize the ice particles in a way that allows PMSE to be observed by the radar. However, NLCs are composed of larger ice particles, providing a sufficiently large surface to reflect enough light to be visible to the naked eye. They can also be detected by LIDAR, (Schäfer et al., 2020). Not all conditions required for observing PMSE are necessary for NLC.

Both during solar maximum and minimum, mono layers showed the lowest average electron density for their respective periods, although this trend was weak. This might imply that higher ionospheric electron densities could be necessary for multi-layered PMSE formation, although this hypothesis requires further investigation.

A parallel can be made between the findings of Paper 3 and the study form Schäfer et al. (2020), where a similar occurrence rates were found for thick layer formation of more than 1 km thickness. The similarities between PMSE and NLC multi-layer formation suggest that insights from NLC research could inform PMSE studies.

While the formation mechanisms of PMSE are somewhat understood, the precise conditions leading to multi-layered PMSE formation remain unclear and would benefit from further research. Hoffmann et al. (2005) suggested that PMSE layering could be explained by the stratification of ice particles due to successive nucleation cycles near the mesopause, followed by growth and sedimentation. Other studies hypothesized links between PMSE multi-layers and gravity waves (Li et al., 2016), (Hoffmann et al., 2005). The formation of multi-layered PMSE is hypothesized to be influenced by gravity waves that transport particles into regions characterized by low temperatures and variable altitudes. Under these conditions, ice particles can form and grow. This process may affect the size of the ice particles, which in turn could impact their spatial distribution through sedimentation and potentially influence the formation of multiple layers. Consequently, future research could focus on exploring the relationships between multi-layered PMSE formation, winds, and gravity waves. For instance, gravity waves could be measured using the EISCAT radar, as suggested by Günzkofer et al. (2023).

The Manda code, specially designed by EISCAT to study PMSE, has an altitude resolution limit of 0.36 km. Considering the narrow altitude range of interest, which spans only 10 km from 80 km to 90 km, and the investigation of up to 4 multilayers within this interval, the resolution might have contributed to

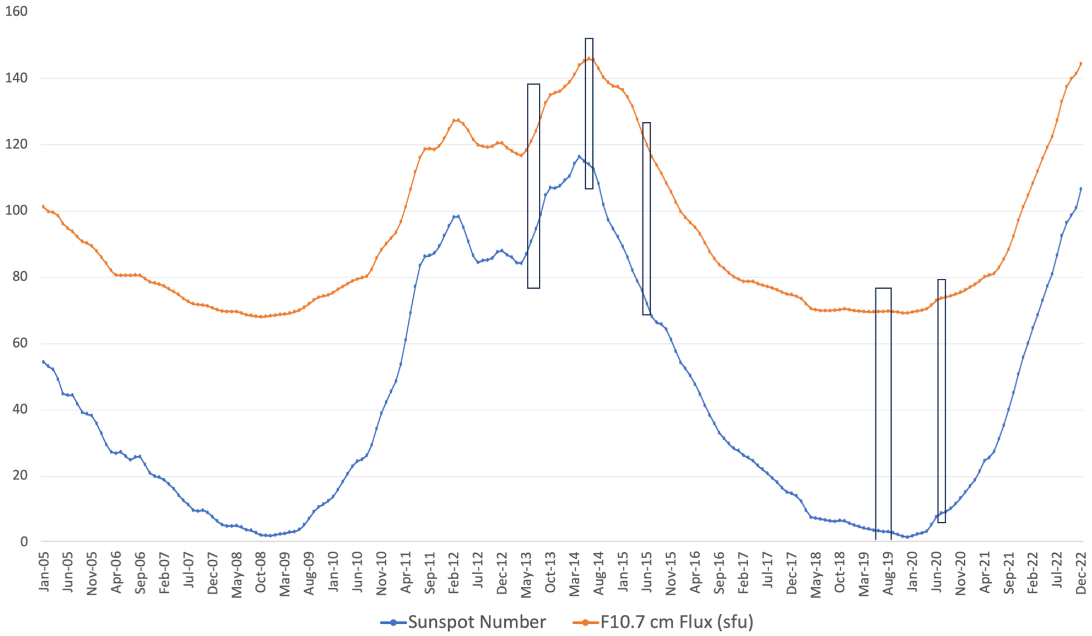

Figure 4.6: Representation of the monthly smoothed sunspot number in blue, and the F10.7 cm flux in orange over the years 2005 to 2022. The F10.7 flux is expressed in sfu, where $1sfu = 10^{-22}W.m^{-2}.Hz^{-1}$. The black frames represent the time periods from which the data for Paper 3 was selected. The data in the smoothed sunspot number graph are obtained from observed monthly mean sunspot numbers, both of which can be found on the Royal Observatory of Belgium website. The values in the smoothed F10.7 cm solar flux graph are derived from daily 10.7 cm solar flux values adjusted to 1 Astronomical Unit (A.U.) and can be found on the Australian Space Weather Forecasting Centre website. The observed monthly mean values in both graphs were obtained using a 13-month running filter for smoothing.

some p-values being above the relative threshold for statistical significance. For future research, utilizing a radar with better resolution at PMSE altitudes could provide more precise mean altitudes for each mono- and multilayer, enabling a more accurate comparison between them.

Gaining insights into the thermodynamic and fluid dynamic processes at altitudes of 80 to 90 km requires a thorough understanding of the complex interactions involved in PMSE formation. Although statistically significant differences are observed in data collected during solar maximum and solar minimum when considering all layers, further research is necessary to determine the underlying causes of these variations.

Key Findings of the Study

In summary, Paper 3 investigated PMSE, with a specific focus on the characteristics of multi-layered PMSE structures and their response to variations in the solar cycle, encompassing both solar maximum and minimum phases. Differences were identified between solar maximum and minimum conditions, alongside other significant findings discussed above. The key results are highlighted below.

- **Differences between Solar Maximum and Solar Minimum:** On average, PMSE layers exhibit higher altitude, echo power, and thickness during solar maximum compared to solar minimum. Additionally, lower altitudes of PMSE were observed during the solar minimum period (2019 and 2020) compared to the solar maximum period (2013 to 2015).

- **Altitude Patterns in Multilayer Sets:** An analysis of individual layers within multilayer sets shows a consistent pattern: both during solar maximum and minimum, the altitude of the top layer increases with the number of multilayers. On the other side, the lowest layer almost always aligns with the NLC altitude as reported by Fiedler et al. (2003) of 83.3 km.

- **Layer Thickness and Echo Power:** The analysis indicates that the thickness of PMSE layers decreases as the number of multilayers increases, accompanied by a reduction in echo power with more multilayers. This observation suggests a potential relationship between the number of layers, echo power, and thickness.

- **Correlation Between Electron Density and Layer Properties:** A positive correlation was observed between electron density at an altitude of 92 km and layer thickness. Similarly, a correlation was found between electron density and echo power. These findings suggest that higher ionization levels at this altitude may lead to stronger PMSE, as reflected in increased echo power.

- **Electron Density Variations:** During both solar maximum and minimum, mono layers exhibited the lowest average electron density for their respective periods, although this trend was relatively weak. This observation might imply that higher ionospheric electron densities are required for the formation of multi-layered PMSE, although further research is needed to confirm this hypothesis.

Chapter 5

Summary and future work

Exploring PMSE can help in climate change research as it offers insights into the water vapor and temperature within the mesosphere. PMSE have been largely investigated for decades, however the study of PMSE multilayers has received limited attention. A few studies such as those from Hoffmann et al. (2005) and Rauf et al. (2018) have investigated PMSE multilayers but the methods they used to identify PMSE data can be improved upon.

In this thesis project, a statistical analysis for identifying and segmenting PMSE from the EISCAT VHF data was implemented. In the past, PMSE detection methods employed threshold on back-scattered power in an altitude range of 80-90 km. The threshold-based approach has limitations; using a high threshold value for back-scattered power ensures that only PMSE data with high signal strength is considered, however, it also results in PMSE data with lower back-scattered power being ignored from the analysis. On the other hand, applying a lower threshold can potentially include non-PMSE data in the analysis.

To address these challenges, a classification model based on random forests with a set of parameters that enables the selection of PMSE data was employed. By using this model on EISCAT VHF data, PMSE data was obtained as the output. This output did not require a high back-scattered power threshold for filtering and allowed a larger number of data points for consideration in the analysis. Compared to threshold-based approaches, a larger number of PMSE radar echoes were classified by the proposed random forests based method. This enabled the finer details of PMSE to be explored by examining both monolayer and multilayer structures.

The random forest based classification model does suffer from occasional misclassifications. This happens when the back-scattered power of PMSE is low, or is of the same order of magnitude as the back scattered power of the ionospheric background. In this case, PMSE data can be misclassified as one of the backgrounds, or else the ionospheric background can be misclassified as PMSE. A possible way to address this in the future is to label more data with different ionospheric conditions, which could lead to a better classification.

The main focus of this thesis was the investigation of PMSE, with the central question being: how do the characteristics of PMSE multi-layered structures change between solar minimum and solar maximum. After applying the classification model to 230 hours of EISCAT VHF observations, encompassing both the solar maximum phase of the solar cycle (years 2013, 2014, and 2015), and the solar minimum phase (years 2019 and 2020), the findings indicated that on average, during solar maximum, PMSE exhibited higher values in altitude, echo power, and layer thickness as compared to solar minimum. As expected, the electron density at 92 km altitude is higher on average during solar maximum.

The results of this thesis project are consistent with the conclusions of Hoffmann et al. (2005), who examined the altitude and occurrence rates of both single and multiple layers. Furthermore, when focusing on the lowest layer within these multilayer sets, it generally matches the NLC altitude of 83.3 km, as reported by Fiedler et al. (2003). Additionally, recent work by Vellalassery et al. (2024) explores NLC variability throughout the solar cycle, and the results from Paper 3 are consistent with those findings.

The obtained results in the thesis project are also consistent with the findings of Li et al. (2016) where they found that the thickness of multi layers decreases with increasing number of multilayers.

The mechanism of the formation of PMSE might be presently well understood, however the exact conditions leading to multi-layered PMSE formation remains unclear, and further investigation is required. As discussed in Paper 3, other factors besides the sole influence of the solar cycle might play an important role in multilayer PMSE formation. As a suggestion for future research, it would be worth investigating the connections between multi-layered PMSE formation and winds and gravity waves rather than solely focusing on the solar cycle. A potential method for measuring gravity waves involves the use of the EISCAT radar, as discussed by (Günzkofer et al., 2023). This could offer a path for future measurements of gravity waves during PMSE events. While differences between the results from observations during solar maximum and during solar minimum considering all the layers together are statistically significant, the cause for the differences needs to be further investigated by future studies.

In order to gain more insight into the distinction of mean altitudes for multilayers during various solar cycle phases, alternative radars or operating modes offering a better resolution in the 80-90 km altitude range could be employed for investigation. Future studies could also explore the use of the classification model implemented in this thesis project on more data, potentially using the EISCAT 3D radar (McCrea et al., 2015) that is currently under construction to cover more than one solar cycle for a more comprehensive understanding of PMSE.

In summary, gaining insights into the processes occurring at altitudes ranging from 80 to 90 km requires a comprehensive understanding of the intricate interplay among various factors involved in PMSE formation. The findings presented in this thesis offer evidence suggesting potential relationships between PMSE properties and gravity wave vertical wavelength, ice particle size, and electron density. The utilized method can help in investigating PMSE phenomena in the future at a broader scale.

References

Andreassen, Ø., Wasberg, C. E., Fritts, D. C., and Isler, J. R.: Gravity wave breaking in two and three dimensions: 1. Model description and comparison of two-dimensional evolutions, Journal of Geophysical Research, 99, 8095–8108, doi: 10.1029/93JD03435, 1994.

Australian Space Weather Forecasting Centre: Space Weather Services website, https://www.sws.bom.gov.au/Solar/1/6, accessed: 2023-08-01.

Baumann, C.: Influences of meteoric aerosol particles on the lower ionosphere, Ph.D. thesis, Ludwig-Maximilians-Universität München, URL `http://nbn-resolving.de/urn:nbn:de:bvb:19-202427`, 2016.

Baumann, C., Rapp, M., and Kero, A.: Secondary electron emission from meteoric smoke particles inside the polar ionosphere, Annales Geophysicae, 34, 573–580, doi: 10.5194/angeo-34-573-2016, URL `https://angeo.copernicus.org/articles/34/573/2016/`, 2016.

Beynon, W. and Williams, P.: Incoherent scatter of radio waves from the ionosphere, Reports on Progress in Physics, 41, 909–956, doi: doi:10.1088/0034-4885/41/6/003, URL `http://iopscience.iop.org/0034-4885/41/6/003`, 1978.

Cutler, A., Cutler, D. R., and Stevens, J. R.: Random Forests, pp. 157–175, Springer US, Boston, MA, doi: 10.1007/978-1-4419-9326-7_5, URL `https://doi.org/10.1007/978-1-4419-9326-7\_5`, 2012.

Czechowsky, P. and Rüster, R.: VHF radar observations of turbulent structures in the polar mesopause region, Annales Geophysicae, 15, 1028–1036, doi: 10.1007/s00585-997-1028-8, URL `https://angeo.copernicus.org/articles/15/1028/1997/`, 1997.

Ecklund, W. L. and Balsley, B. B.: Long-term observations of the Arctic mesosphere with the MST radar at Poker Flat, Alaska, Journal of Geophysical Research, 86, 7775–7780, doi: 10.1029/JA086IA09P07775, 1981.

EISCAT Scientific Association: Documentation on experiments, https://eiscat.se/scientist/document/experiments/, accessed: 2023-08-02.

Fiedler, J., Baumgarten, G., and von Cossart, G.: Noctilucent clouds above ALOMAR between 1997 and 2001: Occurrence and properties, Journal of Geophysical Research: Atmospheres, 108, doi: https://doi.org/10.1029/2002JD002419, URL `https://agupubs.onlinelibrary.wiley.com/doi/abs/10.1029/2002JD002419`, 2003.

Fisher, R. A.: The use of multiple measurements in taxonomic problems, Annals of Eugenics, 7, 179–188, doi: https://doi.org/10.1111/j.1469-1809.1936.tb02137.x, URL `https://onlinelibrary.wiley.com/doi/abs/10.1111/j.1469-1809.1936.tb02137.x`, 1936.

Fritts, D. C., Miller, A. D., Kjellstrand, C. B., Geach, C., Williams, B. P., Kaifler, B., Kaifler, N., Jones, G., Rapp, M., Limon, M., Reimuller, J., Wang, L., Hanany, S., Gisinger, S., Zhao, Y., Stober, G., and Randall, C. E.: PMC Turbo: Studying Gravity Wave and Instability Dynamics in the Summer Mesosphere Using Polar Mesospheric Cloud Imaging and Profiling From a Stratospheric Balloon, Journal of Geophysical Research: Atmospheres, 124, 6423–6443, doi: https://doi.org/10.1029/2019JD030298, URL `https://agupubs.onlinelibrary.wiley.com/doi/abs/10.1029/2019JD030298`, 2019.

Grömping, U.: Variable Importance Assessment in Regression: Linear Regression versus Random Forest, The American Statistician, 63, 308–319, doi: 10.1198/tast.2009.08199, URL `https://doi.org/10.1198/tast.2009.08199`, 2009.

Günzkofer, F., Pokhotelov, D., Stober, G., Mann, I., Vadas, S. L., Becker, E., Tjulin, A., Kozlovsky, A., Tsutsumi, M., Gulbrandsen, N., Nozawa, S., Lester, M., Belova, E., Kero, J., Mitchell, N. J., and Borries, C.: Inferring neutral winds in the ionospheric transition region from atmospheric-gravity-wave traveling-ionospheric-disturbance (AGW-TID) observations with the EISCAT VHF radar and the Nordic Meteor Radar Cluster, Annales Geophysicae, 41, 409–428, doi: 10.5194/angeo-41-409-2023, URL `https://angeo.copernicus.org/articles/41/409/2023/`, 2023.

Hastie, T., Friedman, J., and Tibshirani, R.: Linear Methods for Classification, pp. 79–113, Springer New York, New York, NY, doi: 10.1007/978-0-387-21606-5_4, URL `https://doi.org/10.1007/978-0-387-21606-5\_4`, 2001a.

Hastie, T., Friedman, J., and Tibshirani, R.: Additive Models, Trees, and Related Methods, pp. 257–298, Springer New York, New York, NY, doi: 10.1007/978-0-387-21606-5_9, URL `https://doi.org/10.1007/978-0-387-21606-5\_9`, 2001b.

Hoffmann, P., Rapp, M., Serafimovich, A., and Latteck, R.: On the occurrence and formation of multiple layers of polar mesosphere summer echoes, Geophysical Research Letters, 32, doi: https://doi.org/10.1029/2004GL021409, URL `https://agupubs.onlinelibrary.wiley.com/doi/abs/10.1029/2004GL021409`, 2005.

Hunten, D. M., Turco, R. P., and Toon, O. B.: Smoke and Dust Particles of Meteoric Origin in the Mesosphere and Stratosphere, Journal of Atmospheric Sciences, 37, 1342 – 1357, doi: https://doi.org/10.1175/1520-0469(1980)037<1342:SADPOM>2.0.CO;2, URL `https://journals.ametsoc.org/view/journals/atsc/37/6/1520-0469_1980_037_1342_sadpom_2_0_co_2.xml`, 1980.

Jozwicki, D., Sharma, P., and Mann, I.: Investigation of Polar Mesospheric Summer Echoes Using Linear Discriminant Analysis, Remote Sensing, 13, doi: 10.3390/rs13030522, URL `https://www.mdpi.com/2072-4292/13/3/522`, 2021.

Jozwicki, D., Sharma, P., Mann, I., and Hoppe, U.-P.: Segmentation of PMSE Data Using Random Forests, Remote Sensing, 14, doi: 10.3390/rs14132976, URL `https://www.mdpi.com/2072-4292/14/13/2976`, 2022.

Jozwicki, D., Sharma, P., Huyghebaert, D., and Mann, I.: Polar mesospheric summer echo (PMSE) multilayer properties during the solar maximum and solar minimum, Annales Geophysicae, 42, 431–453, doi: 10.5194/angeo-42-431-2024, URL `https://angeo.copernicus.org/articles/42/431/2024/`, 2024.

Li, H., Wu, J., and Zhou, Z.: The formation of multiple layers of ice particles in the polar summer mesopause region, Annales Geophysicae, 34, 117–122, doi: 10.5194/angeo-34-117-2016, 2016.

Lübken, F.-J., Berger, U., and Baumgarten, G.: On the Anthropogenic Impact on Long-Term Evolution of Noctilucent Clouds, Geophysical Research Letters, 45, 6681–6689, doi: https://doi.org/10.1029/2018GL077719, URL `https://agupubs.onlinelibrary.wiley.com/doi/abs/10.1029/2018GL077719`, 2018.

McCrea, I., Aikio, A., Alfonsi, L., Belova, E., Buchert, S., Clilverd, M., Engler, N., Gustavsson, B., Heinselman, C., Kero, J., Kosch, M., Lamy, H., Leyser, T., Ogawa, Y., Oksavik, K., Pellinen-Wannberg, A., Pitout, F., Rapp, M., Stanislawska, I., and Vierinen, J.: The science case for the EISCAT_3D radar, Progress in Earth and Planetary Science, 2, doi: 10.1186/s40645-015-0051-8, 2015.

Megner, L., Rapp, M., and Gumbel, J.: Distribution of meteoric smoke - Sensitivity to microphysical properties and atmospheric conditions, Atmospheric Chemistry and Physics, 6, doi: 10.5194/acpd-6-5357-2006, 2006.

Narayanan, V. L., Häggström, I., and Mann, I.: Effects of particle precipitation on the polar mesospheric summer echoes observed by EISCAT VHF 224 MHz radar, Advances in Space Research, 69, 3350–3361, doi: https://doi.org/10.1016/j.asr.2022.02.015, URL `https://www.sciencedirect.com/science/article/pii/S0273117722001119`, 2022.

Probst, P., Wright, M. N., and Boulesteix, A.-L.: Hyperparameters and tuning strategies for random forest, WIREs Data Mining and Knowledge Discovery, 9, e1301, doi: https://doi.org/10.1002/widm.1301, URL `https://onlinelibrary.wiley.com/doi/abs/10.1002/widm.1301`, 2019.

Rapp, M. and Lübken, F.-J.: Polar mesosphere summer echoes (PMSE): Review of observations and current understanding, Atmospheric Chemistry and Physics, 4, 2601–2633, doi: 10.5194/acp-4-2601-2004, URL `https://acp.copernicus.org/articles/4/2601/2004/`, 2004.

Rapp, M. and Lübken, F.-J.: On the nature of PMSE: Electron diffusion in the vicinity of charged particles revisited, Journal of Geophysical Research: Atmospheres, 108, doi: https://doi.org/10.1029/2002JD002857, URL `https://agupubs.onlinelibrary.wiley.com/doi/abs/10.1029/2002JD002857`, 2003.

Rauf, A., Li, H., Ullah, S., Lin, M., Wang, B., and Wang, M.: Statistical study about the influence of particle precipitation on mesosphere summer echoes in polar latitudes during July 2013, Earth, Planets and Space, 70, doi: 10.1186/s40623-018-0885-6, 2018.

Royal Observatory of Belgium: WDC-SILSO, https://sidc.be/SILSO/home, accessed: 2023-08-01.

Schäfer, B., Baumgarten, G., and Fiedler, J.: Small-scale structures in noctilucent clouds observed by lidar, Journal of Atmospheric and Solar-Terrestrial Physics, 208, 105 384, doi: https://doi.org/10.1016/j.jastp.2020.105384, URL `https://www.sciencedirect.com/science/article/pii/S1364682620301942`, 2020.

Shucan, G., Li, H., Xu, T., Zhu, M., Wang, M., Lin, M., Ullah, S., and Rauf, A.: Characteristics of the layered polar mesosphere summer echoes occurrence ratio observed by EISCAT VHF 224 MHz radar, Annales Geophysicae, 37, 417–427, doi: 10.5194/angeo-37-417-2019, 2019.

Theodoridis, S. and Koutroumbas, K.: Pattern Recognition, Pattern Recognition, Elsevier Science, URL `https://books.google.no/books?id=gAGRCmp8Sp8C`, 2006.

Vellalassery, A., Baumgarten, G., Grygalashvyly, M., and Lübken, F.-J.: Long-Term Evolution in Noctilucent Clouds' Response to the Solar Cycle: A Model-Based Study, Atmosphere, 15, doi: 10.3390/atmos15010088, URL `https://www.mdpi.com/2073-4433/15/1/88`, 2024.

Venkata, J.: Random_forest_diagram_complete.png Random Forest Simplified, URL `https://commons.wikimedia.org/wiki/File:Random_forest_diagram_complete.png`, accessed: 2023-06-19, 2021.

Wilms, H., Rapp, M., Hoffmann, P., Fiedler, J., and Baumgarten, G.: Gravity wave influence on NLC: experimental results from ALOMAR, 69° N, Atmospheric Chemistry and Physics, 13, 11 951–11 963, doi: 10.5194/acp-13-11951-2013, URL `https://acp.copernicus.org/articles/13/11951/2013/`, 2013.

Zhao, X. R., Sheng, Z., Shi, H. Q., Weng, L. B., and Liao, Q. X.: Long-Term Trends and Solar Responses of the Mesopause Temperatures Observed by SABER During the 2002–2019 Period, Journal of Geophysical Research: Atmospheres, 125, e2020JD032 418, doi: https://doi.org/10.1029/2020JD032418, URL `https://agupubs.onlinelibrary.wiley.com/doi/abs/10.1029/2020JD032418`, e2020JD032418 2020JD032418, 2020.

PAPER I

Investigation of Polar Mesospheric Summer Echoes Using Linear Discriminant Analysis

Jozwicki, D. and Sharma, P. and Mann, I.: Investigation of Polar Mesospheric Summer Echoes Using Linear Discriminant Analysis, Remote Sensing, doi: 10.3390/rs13030522, 2021

remote sensing

Article

Investigation of Polar Mesospheric Summer Echoes Using Linear Discriminant Analysis

Dorota Jozwicki [1,*], **Puneet Sharma** [2] **and Ingrid Mann** [1]

[1] Department of Physics and Technology, UiT The Arctic University of Norway, Forskningsparken, Sykehusvegen 21, 9019 Tromsø, Norway; ingrid.b.mann@uit.no
[2] Department of Automation and Process Engineering, UiT The Arctic University of Norway, Teknologibygget, Klokkargårdsbakken 35, 9019 Tromsø, Norway; puneet.sharma@uit.no
* Correspondence: dorota.s.jozwicki@uit.no

Abstract: Polar Mesospheric Summer Echoes (PMSE) are distinct radar echoes from the Earth's upper atmosphere between 80 to 90 km altitude that form in layers typically extending only a few km in altitude and often with a wavy structure. The structure is linked to the formation process, which at present is not yet fully understood. Image analysis of PMSE data can help carry out systematic studies to characterize PMSE during different ionospheric and atmospheric conditions. In this paper, we analyze PMSE observations recorded using the European Incoherent SCATter (EISCAT) Very High Frequency (VHF) radar. The collected data comprises of 18 observations from different days. In our analysis, the image data is divided into regions of a fixed size and grouped into three categories: PMSE, ionosphere, and noise. We use statistical features from the image regions and employ Linear Discriminant Analysis (LDA) for classification. Our results suggest that PMSE regions can be distinguished from ionosphere and noise with around 98 percent accuracy.

Keywords: polar mesospheric summer echoes (PMSE); linear discriminant analysis (LDA)

Citation: Jozwicki, D.; Sharma, P.; Mann, I. Investigation of Polar Mesospheric Summer Echoes Using Linear Discriminant Analysis. *Remote Sens.* **2021**, *13*, 522. https://doi.org/10.3390/rs13030522

Received: 17 December 2020
Accepted: 29 January 2021
Published: 2 February 2021

1. Introduction

Radar observations at mid and high latitudes detect during the Arctic summer months echoes that originate from 80 to 90 km altitude, i.e., in the mesosphere [1]. These Polar Mesospheric Summer Echoes (PMSE) are radio waves scattered at spatial structures in the distribution of the free electrons which form in the presence of ice particles and neutral air turbulence [2,3]. The charging of ice particles influences the electron distribution and the radar echoes can in this way detect ice particles with small dimensions that are not or only partly observed with optical methods [3]. The larger among the ice particles are visible to the human eye in Noctilucent Clouds (NLC). NLC originate from larger particles than PMSE. Both PMSE and NLC form when the mesosphere is the coldest. We refer the reader to a detailed review of the early observations of PMSE [2] and to an overview of the understanding of this phenomenon [3].

Both PMSE and NLC occur at altitudes that are difficult to study due to poor accessibility. In situ measurements in the mesosphere can be made from rockets, but only during short time intervals. Radar measurements from the ground remain a good option for observational studied and can be made independently from weather conditions. Therefore, PMSE provide an interesting tool for local long-term studies of ice particles and their interactions in the mesosphere. For example, the 53.5 MHz Middle Atmosphere Alomar Radar System (MAARSY) on Andøya provides information on the occurrence rate of PMSE on a yearly and diurnal scale and their altitude [4].

The European Incoherent SCATter (EISCAT) radars are high-power, large-aperture radars and they also detect PMSE. They are, however primarily designed to study incoherent scatter, a process that depends on electron density and hence ionization in the upper atmosphere [5]. The ionization is influenced by sunlight, energetic particle precipitation, and other phenomena of the Arctic ionosphere that also influence the PMSE process. While it is interesting to study both phenomena at the same time, this complicates the analysis since the PMSE signal, and the incoherent scatter signal need to be separated. Figure 1 illustrates a typical EISCAT observation. The image displays PMSE in horizontal wavy layers between 80 and 90 km and incoherent scatter from the ionospheric electrons above. Figure 1 also shows that, for part of the observation a strong ionospheric signal extends down almost to 70 km. This illustrates that altitude is not a sufficient criterion to distinguish both components. While both signals can be distinguished by means of their different frequency distributions [3,5], those can only be studied involving additional data. We here attempt to make a separation based on data sets like the one shown in Figure 1. The separation of image regions is also of interest for future studies to compare the occurrence of PMSE and NLC [6]. We follow this recent work [6] to analyze NLC images and start by considering Linear Discriminant Analysis (LDA).

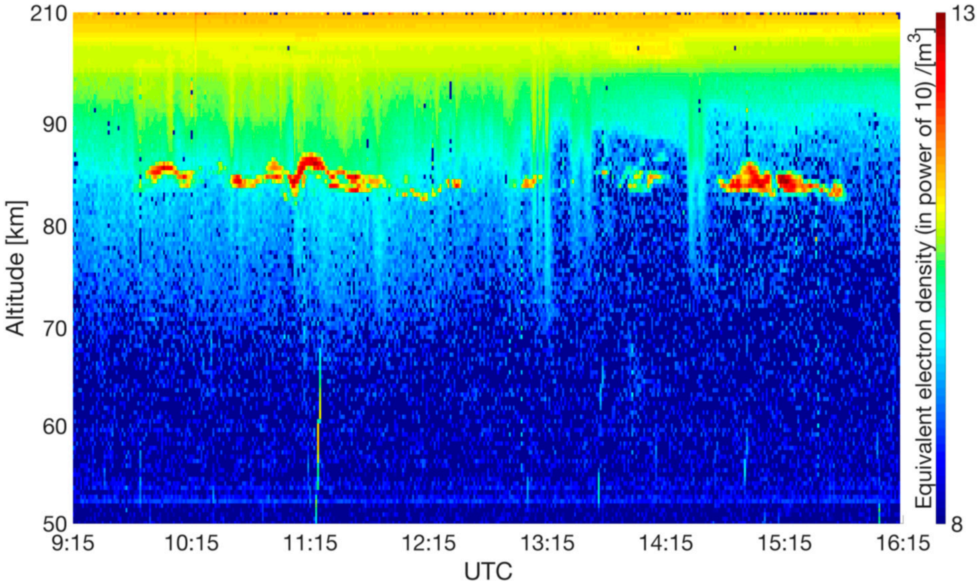

Figure 1. An example of a raw image with typical PMSE event analyzed with LDA in the latter part of this paper. The data used to plot this image is from the 10th of August 2015 over an altitude from 50 to 210 km altitude.

Our study investigates the separability of PMSE from noise background and ionospheric background regions in EISCAT observations. This study is further motivated because a new radar, EISCAT_3D [7] is at present under construction. It will allow us to observe PMSE in the same volume from three different sites and hence provide more information on the motion of the structures that form the PMSE [8]. Analysis tools need to be developed in order to compare the observations from the different sites. The EISCAT_3D can also be used for monitoring observations with the perspective to provide a large data set for statistical analysis.

We introduce the statistical methods applied in Section 2, describe the analysis process in Section 3, and present and discuss the results in Section 4. We draw a short conclusion (Section 5) and give additional information in the Appendix A.

2. Methods

2.1. *Linear Discriminant Analysis (LDA)*

LDA, also known as Fischer′s discriminant analysis [9] considers two classes of distributions, μ_1 and μ_2 and covariances Σ_1 and Σ_2, where the separation criterion $J(\boldsymbol{w})$ between the two is defined by the ratio of variance between classes and within classes as:

$$J(\boldsymbol{w}) = \frac{\boldsymbol{w}^T S_B \boldsymbol{w}}{\boldsymbol{w}^T S_W \boldsymbol{w}'} \tag{1}$$

In this expression, $\boldsymbol{w}$ is a vector that is normal to the discriminant hyperplane, T denotes the transpose and S_B and S_W describe between and within-class scatter respectively. They are:

$$S_B = (\mu_1 - \mu_2)(\mu_1 - \mu_2)^T, \tag{2}$$

$$S_W = (\Sigma_1 + \Sigma_2) \tag{3}$$

The results obtained from the two-class case can be extended to three and more classes. For more details, please see [10].

In order to analyze the separability of the three distinct classes corresponding to the PMSE, background noise, and ionospheric background, we selected smaller image regions or window sizes from the complete images as shown in Figure 2. We apply the LDA algorithm on these image windows; the features used for LDA are a combination of low-order statistics: mean and standard deviation and higher-order statistics: skewness and kurtosis.

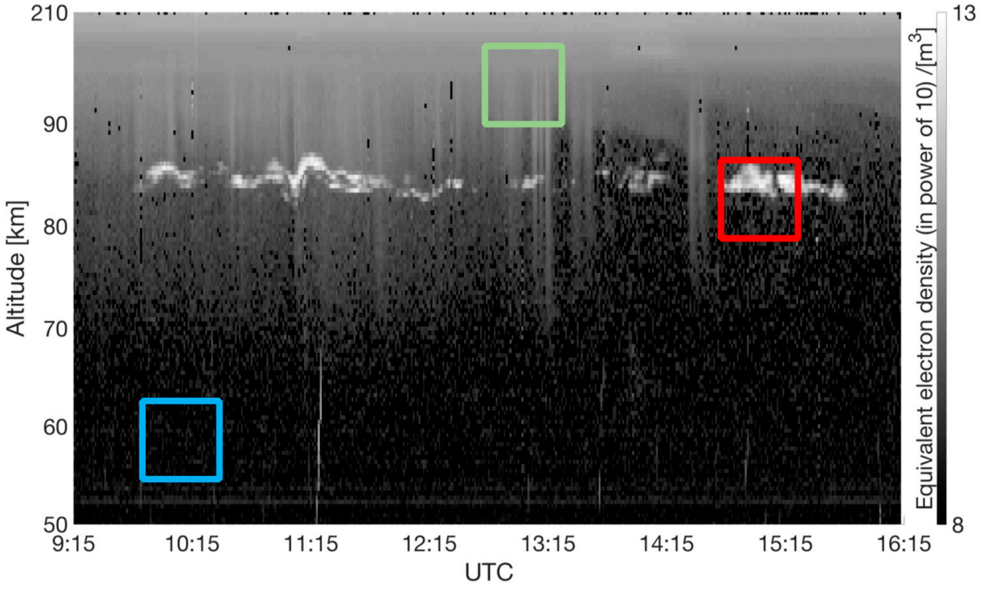

Figure 2. Figure showing the way windows are collected. The whole image is plotted in black and white. Targeted day (dd.mm.yyyy): 10.08.2015. Smaller image regions or window sizes are collected from the complete image, and correspond to the 3 different classes, respectively: Red window for the PMSE group; Blue window for the background noise group; Green window for the ionospheric background group.

2.2. *Skewness and Kurtosis*

Skewness is a measure of asymmetry or the extent to which a given distribution differs from a normal distribution [10]. For a random variable X, the skewness $S[X]$ is calculated by its standardized third central moment as [11],

$$S[X] = E\left[\left(\frac{X-\mu}{\sigma}\right)^3\right] \tag{4}$$

where μ is the mean, σ is the standard deviation, and E is the average or expected value. The values of $S[X]$ can be positive, negative, zero, or undefined.

Kurtosis is a measure of outliers in a distribution. For a random variable X, the kurtosis $K[X]$ is defined by its fourth standardized moment as [12],

$$K[X] = E\left[\left(\frac{X-\mu}{\sigma}\right)^4\right] \tag{5}$$

2.3. Input Data

In this study, we use 18 images taken during four different years with the EISCAT Very High Frequency (VHF, 224 MHz) radar located near Tromsø (69.58°N, 19.2272°E). The data which is given in ASCII format, denotes the electron density (NEL) in regions of incoherent scatter [13] and a signal proportional to the backscattered power in the PMSE [13]. The incoherent scatter can be described as the scattering of the electromagnetic waves at free electrons. As described in a theoretical work [14], it is possible to deduce the total amount of electrons in the targeted area based on the total energy received.

3. Procedure

The dataset consists of 18 images with PMSE observations in different time intervals. The details of the 18 selected observations for the study are listed in Table A1 in the appendix. For each group, eight image regions or windows are collected. This means that there are $8 \times 3 = 24$ windows for every image. Figure 2 shows the three different classes of an image: PMSE, background noise, and ionospheric background. We use default window size of 100 by 100 pixels (see Section 4).

As shown in Figure 3, the histograms′ grayscale distributions look different for the three classes. The one for the PMSE (Figure 3a) has the largest standard deviation. The one for the ionospheric background class (Figure 3b) has the lowest standard deviation and the highest mean. For the background noise, the mean value is the lowest of all, and the standard deviation is low as well. These differences in the three classes imply that they can be separated using mean and standard deviation. One can also notice that Figure 3a looks like a combination of the distributions seen in Figure 3b,c, and some high intensity grayscale values. PMSE occur at an altitude where background noise and ionospheric background are partially present, this means that the grayscale histogram distribution of PMSE (shown in Figure 3a) can vary depending on the window size and the proportional presence of background noise and ionospheric background. In Figure 3, the grayscale values are in the range [0–255], 0 being black and 255 being white.

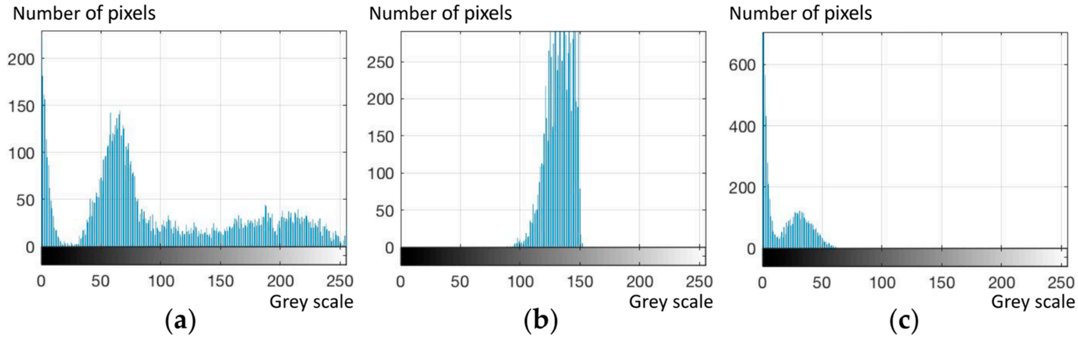

Figure 3. Selected histograms showing the differences in the grayscale distribution for the 3 different classes being: (**a**) PMSE; (**b**) ionospheric background; (**c**) background noise. Targeted day (dd.mm.yyyy): 10.08.2015. The grayscale values are in the range [0,255]. The vertical scale shows the number of pixels.

4. Results

The accuracy of classification is defined as the ratio of number of correctly predicted image regions to that of all the image regions used for testing. Table 1 shows the accuracies obtained by using a window size of 100 by 100 pixels and four different combinations of parameters: mean standard deviation, skewness, and kurtosis.

Table 1. This table shows the accuracies in percent of different LDA for a window size of 100 × 100 pixels and 4 different sets of parameters. Values written in bold font are the highest.

Window Size	M	M, Std [1]	M, Std, Sk [2]	M, Std, Sk, K [3]
100	93.26 ± 1.87	**97.05 ± 0.91**	96.21 ± 0.87	**97.05 ± 1.40**

[1] Std: Standard deviation. [2] Sk: Skewness. [3] K: Kurtosis.

From the complete dataset, 70 percent is used for training, i.e., 302 out of 432 samples, and 30 percent is used for testing i.e., 130 samples. The training and testing samples are randomly selected.

In Figure 4, we visualize the separation of the whole data into the three classes i.e., PMSE, background noise, and ionospheric background by using a window size of 100 by 100 pixels and mean and standard deviation as two dimensions for LDA. Furthermore, the results in the figure show that there are only 6 misclassifications out of 130 samples used for testing.

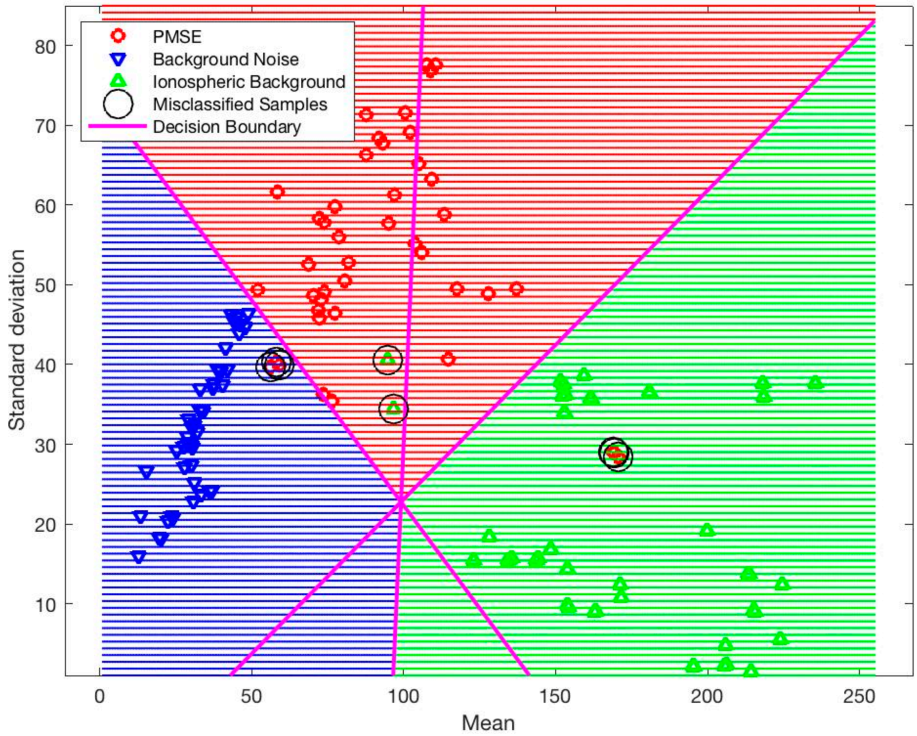

Figure 4. Plot representing the LDA using 30 percent of the whole dataset, used for predicting. Two dimensions are used here: mean and standard deviation. The different colored dots and correspondingly colored shaded areas represent the different classes. Blue symbols represent the background noise class, green symbols represent the ionospheric background class, and red symbols represent the PMSE class. The pink lines represent the linear separation between the 3 groups. Here, the accuracy of the separation is 93.94.

We also use LDA for different window sizes ranging from 60 to 200 pixels, the resulting variation of the accuracy is shown in Figure 5 (see also Table A2 in the Appendix A). We reach best accuracies within 90 percent for window sizes ranging from 100 to 180 pixels with the best value of 98.18 percent for window size of 160 by160 pixels and including all four parameters. We chose the window size of 100 by100 pixels as a compromise between size and accuracy.

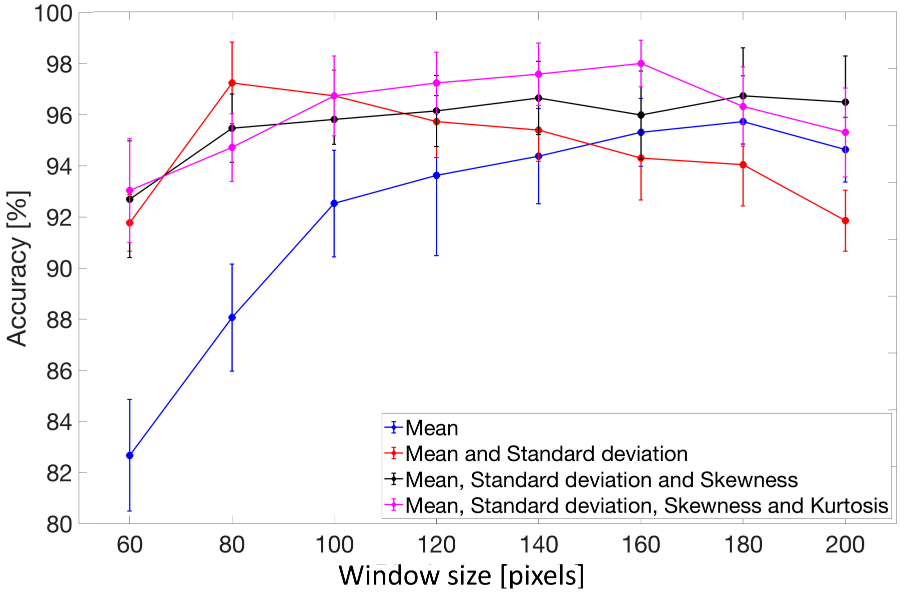

Figure 5. The plot represents the LDA′s different accuracies for all the different window sizes used and for all the different sets of dimensions used.

The results for accuracies pertaining to training and test data are shown in Table A3, we can observe that they show comparable accuracies. The classification accuracies shown in Figure 5 are obtained by taking an average over 10 iterations of randomly selecting the training and testing data from the dataset. We also test 10, 100 and 1000 iterations, the results are shown in Tables A4–A6, indicate that there are no significant differences in the accuracy values obtained from the different iterations.

5. Discussion

The best accuracies are obtained with two different sets of parameters as shown in Table 1. The first one is mean and standard deviation, and the second one is using all the four parameters: mean, standard deviation, skewness, and kurtosis.

In Figure 5, we can see that almost all the different sets of parameters are following a similar trend, i.e., the accuracy is improving with a larger window size up to 180 pixels, after which the accuracy starts to decrease. In this study, the time scale and the altitude scale of the images are not consistent, they are varying from one image to another without influencing the accuracy of the classification. In other words, a larger or smaller amount of background data does not change much the accuracy of classification, especially for two and more parameters.

We can notice in Figure 4, that a few PMSE got misclassified into either the ionospheric background class or the background noise class. This can be possibly attributed to the fact that the PMSE occurs at the boundary altitude between the ionospheric signal region and the background noise region. Therefore, if the PMSE is not strong, or if its intensity is close to the background noise intensity, it can get misclassified. Figures 6 and 7 show examples of PMSE events when misclassifications happened. In Figure 6, a few examples of samples belonging to the PMSE class were misclassified as belonging to the background noise class. Figure 7 shows a case where PMSE samples got misclassified as ionospheric background.

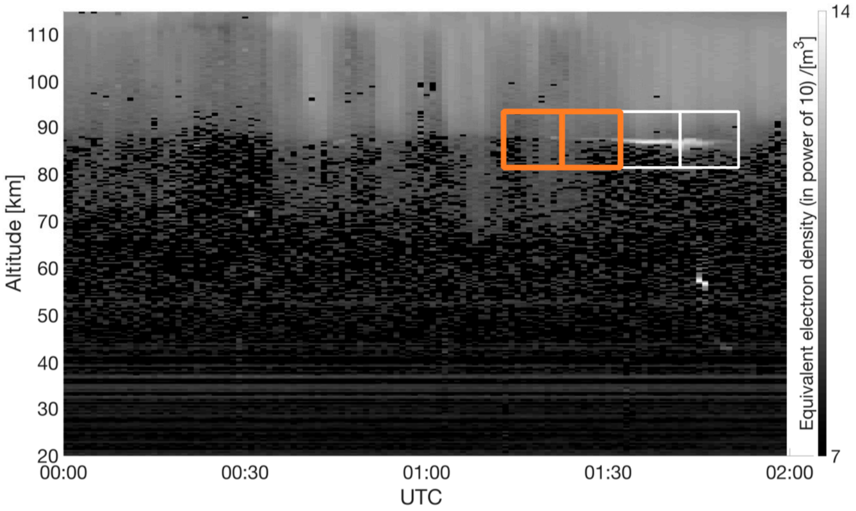

Figure 6. Case of a PMSE from the 20 of August 2015 during which a misclassification of a PMSE window as background noise happened. The white squares represent PMSE windows classified in the right group, while the orange windows represent examples of misclassifications containing a weaker PMSE signal.

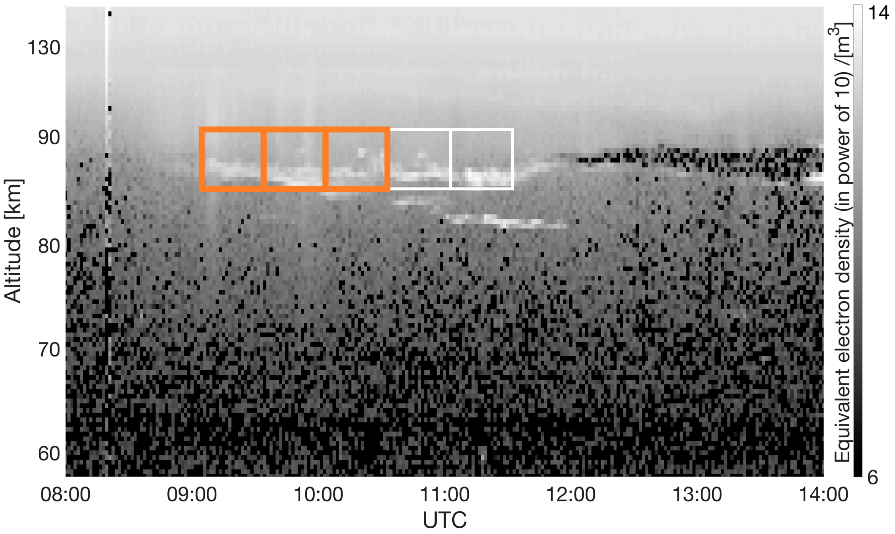

Figure 7. Case of a PMSE from the 30 of June 2008 during which a misclassification of a PMSE window as ionospheric background happened. The white squares represent PMSE windows classified in the right group during the LDA, while the orange windows represent examples of misclassifications where the PMSE signal looks almost as intense as the ionospheric background.

The ionospheric background class can also be misclassified as PMSE, but the background noise is never misclassified. One possible explanation for this is that the ionospheric background can vary from one image to another. Figure 8 presents two images (7 July 2010 and 10 August 2015) with very different ionospheric backgrounds. It is homogeneous in the 2010 image while in the 2015 image it displays vertical stripes, a curtain-like structure. This pattern extends lower down in altitude and overlaps with the PMSE altitude, possibly explaining the misclassification.

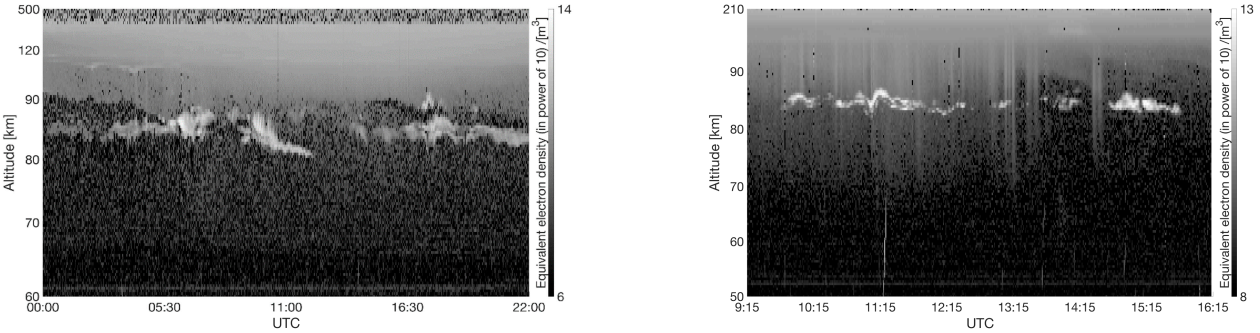

(**a**) (**b**)

Figure 8. Plots representing different ionospheric background conditions. Plot (**a**) is from the 7 July 2010. The ionospheric background looks homogeneous. Plot (**b**) is from the 10 of August 2015. The ionospheric background is not homogeneous anymore. It is possible to regularly distinguish curtain-like patterns along the time axis.

This study shows that LDA can be applied to distinguish PMSE regions in images from those with ionospheric incoherent scatter and with background noise. In comparison to more advanced methods that are applied for example to the analyses of NLC [6] and of radar observations at other, (HF) high frequency [15], it is more simple and computationally inexpensive. It is therefore suitable to preselect PMSE regions for further analysis.

6. Conclusions

This paper describes an analysis approach for PMSE observations made with an incoherent scatter radar. Our study shows that LDA can be used to distinguish image regions containing PMSE from those with noise or ionospheric background. We noted that samples belonging to the background noise class were not misclassified, however, samples belonging to the other categories were sometimes misclassified. This can be attributed to factors like the changes of the ionospheric background over the years. Our proposed method can be used to pre-select data for further analysis of the shape of the PMSE for which we will consider methods in the future; it can be used for simultaneous studies of PMSE and NLC; and it is suitable for analyzing large data sets like those from the EISCAT_3D [7] that is at present under construction.

Author Contributions: Conceptualization, D.J., P.S. and I.M.; programming, D.J.; investigation, D.J.; data curation, D.J.; writing—original draft preparation, D.J.; writing—review and comments, P.S. and I.M.; supervision, P.S. and I.M.; project administration, I.M.; funding acquisition, I.M. All authors have read and agreed to the published version of the manuscript.

Funding: This work is supported by a project funded by the Research Council of Norway, NFR 275503. The EISCAT International Association is supported by research organizations in Norway (NFR), Sweden (VR), Finland (SA), Japan (NIPR and STEL), China (CRIPR), and the United Kingdom (NERC).

Acknowledgments: The authors thank Anders Tjulin and Ingemar Häggström (both at the International EISCAT Scientific Association) for support on access and using EISCAT data and thank the anonymous referees for constructive comments that helped to improve the manuscript. DJ thanks Srishti Gautam (UiT) for support with using MATLAB.

Conflicts of Interest: The authors declare no conflict of interest. The funders had no role in the design of the study; in the collection, analyses, or interpretation of data; in the writing of the manuscript, or in the decision to publish the results.

Appendix A

The 18 images and therefore the 18 PMSE observations used for the study, their date, start and end time are listed in Table A1.

Table A1. This table lists the dates given in (*day. month. year*) that are used for the LDA and universal time (UTC) of observation given in (*hour: minutes: seconds*).

Dates (dd.mm.yyyy)	Start Time in UTC [1] (hh:mm:ss)	End Time in UTC (hh:mm:ss)
28.06.2008	07:58:33	08:36:18
30.06.2008	07:59:38	12:07:30
02.07.2008	10:24:30	11:59:02
10.06.2009	09:03:42	11:56:09
11.06.2009	09:03:42	11:59:12
14.07.2009	08:19:33	11:33:15
16.07.2009	08:47:30	10:06:26
17.07.2009	07:49:44	11:59:30
26.07.2009	08:00:29	11:59:22
30.07.2009	12:15:29	15:59:08
07.07.2010	00:00:30	21:59:27
08.07.2010	09:00:42	12:59:03
09.08.2015	00:00:26	01:59:26
10.08.2015	09:14:40	16:12:28
12.08.2015	20:04:40	23:59:28
13.08.2015	00:00:28	01:59:26
19.08.2015	00:00:28	01:59:26
20.08.2015	00:00:28	01:59:26

[1] Start time in UTC does not mean the start of a PMSE event. In fact, the observation time does not necessarily mean that a PMSE is happening during the whole time frame, nor that the PMSE is centered around the middle of the time frame. Nevertheless, there is a PMSE event in every image.

The detail of the testing accuracies used to plot Figure 5 is listed in the following Table A2.

Table A2. This table shows the testing accuracies in percent of different LDA that are conducted over the same dataset.

Window Size	M [1]	M, Std [2]	M, Std, Sk [3]	M, Std, Sk, K [4]
60	84.39 ± 1.96	92.58 ± 1.00	93.41 ± 2.05	93.71 ± 1.82
80	89.24 ± 1.88	97.50 ± 1.43	95.91 ± 1.20	95.23 ± 1.19
100	93.26 ± 1.87	97.05 ± 0.91	96.21 ± 0.87	97.05 ± 1.40
120	94.24 ± 2.82	96.14 ± 1.26	96.52 ± 1.25	97.50 ± 1.07
140	94.92 ± 1.68	95.83 ± 1.09	96.97 ± 1.29	97.80 ± 1.10
160	95.76 ± 1.20	94.85 ± 1.46	96.36 ± 1.55	98.18 ± 0.81
180	96.14 ± 1.61	94.62 ± 1.45	97.05 ± 1.69	96.67 ± 1.39
200	95.15 ± 1.14	92.65 ± 1.07	96.82 ± 1.63	95.76 ± 1.56

[1] M: Mean. [2] Std: Standard deviation. [3] Sk: Skewness. [4] K: Kurtosis.

The detail of the training accuracies used to plot Figure 5 is listed in the following Table A3.

Table A3. This table shows the training accuracies in percent of different LDA that are conducted over the same dataset.

Window Size	M [1]	M, Std [2]	M, Std, Sk [3]	M, Std, Sk, K [4]
60	84.53 ± 0.88	93.00 ± 0.68	93.63 ± 0.71	94.23 ± 0.79
80	88.50 ± 0.79	96.47 ± 0.53	95.93 ± 0.52	95.57 ± 0.59
100	92.57 ± 0.82	96.93 ± 0.49	97.00 ± 0.75	97.20 ± 0.63
120	94.67 ± 0.63	96.63 ± 0.33	96.60 ± 0.56	97.87 ± 0.45
140	94.80 ± 1.21	96.33 ± 0.59	96,67 ± 0.72	98.13 ± 0.42
160	95.57 ± 0.55	96.00 ± 0.44	96.87 ± 0.83	98.07 ± 0.52
180	95.73 ± 0.54	95.50 ± 0.95	97.10 ± 0.72	97.53 ± 0.59
200	95.40 ± 0.86	93.33 ± 0.80	96.57 ± 0.55	97.33 ± 0.52

[1] M: Mean. [2] Std: Standard deviation. [3] Sk: Skewness. [4] K: Kurtosis.

It is important to note that the steps in altitude are not equal between lower and higher altitudes. Figure A1 shows that the altitude scale is constant from altitudes 50 km to 100 km. From a 100 km altitude, the scale starts to be exponential. This graph describes the data taken 10 of August 2015, but all data sets used in this study show a similar feature.

Table A4 shows the averaged accuracies after 10 runs of the LDA, Table A5 shows the accuracies averaged after 100 runs and finally Table A6 shows the accuracies averaged over 1000 runs.

Table A4. This table shows the testing accuracies in percent, averaged over 10 runs of LDA.

Window Size	M [1]	M, Std [2]	M, Std, Sk [3]	M, Std, Sk, K [4]
60	85.53	92.58	93.64	94.70
80	89.39	96.67	95.91	95.08
100	92.88	96.29	97.05	97.20
120	94.55	96.67	96.52	97.50
140	95.00	95.83	96.44	97.50
160	95.53	95.91	96.59	97.58
180	95.91	95.15	97.12	96.59
200	94.70	92.50	97.42	96.89

[1] M: Mean. [2] Std: Standard deviation. [3] Sk: Skewness. [4] K: Kurtosis.

Table A5. This table shows the testing accuracies in percent, averaged over 100 runs of LDA.

Window Size	M [1]	M, Std [2]	M, Std, Sk [3]	M, Std, Sk, K [4]
60	84.71	92.62	92.89	93.98
80	88.17	96.72	95.86	95.37
100	91.88	96.83	96.54	96.90
120	94.25	96.72	96.43	97.53
140	95.05	96.14	96.39	97.55
160	95.45	95.50	96.80	97.73
180	95.88	94.90	96.82	96.91
200	95.23	92.88	96.37	96.63

[1] M: Mean. [2] Std: Standard deviation. [3] Sk: Skewness. [4] K: Kurtosis.

Table A6. This table shows the testing accuracies in percent, averaged over 1000 runs of LDA.

Window Size	M [1]	M, Std [2]	M, Std, Sk [3]	M, Std, Sk, K [4]
60	84.56	92.73	93.11	93.73
80	88.44	96.66	95.79	95.45
100	92.45	96.75	96.54	97.02
120	94.42	96.51	96.61	97.55
140	95.13	96.03	96.57	97.67
160	95.53	95.63	96.66	97.68
180	95.70	95.11	96.98	96.78
200	95.02	93.02	96.65	96.55

[1] M: Mean. [2] Std: Standard deviation. [3] Sk: Skewness. [4] K: Kurtosis.

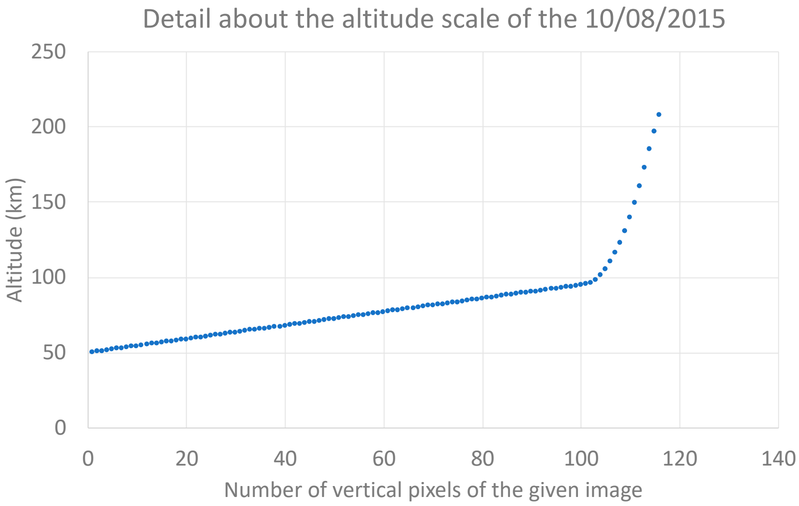

Figure A1. Plots representing the difference in altitude between each step or incrementation in vertical pixels in the image.

References

1. Ecklund, W.L.; Balsley, B.B. Long-term observations of the Arctic mesosphere with the MST radar at Poker Flat, Alaska. *J. Geophys. Res. Space Phys.* **1981**, *86*, 7775–7780. [CrossRef]
2. Cho, J.Y.N.; Röttger, J. An updated review of polar mesosphere summer echoes: Observation, theory, and their relationship to noctilucent clouds and subvisible aerosols. *J. Geophys. Res. Atmos.* **1997**, *102*, 2001–2020. [CrossRef]
3. Rapp, M.; Lübken, F.J. Polar mesosphere summer echoes (PMSE): Review of observations and current understanding. *Atmos. Chem. Phys.* **2004**, *4*, 2601–2633. [CrossRef]
4. Latteck, R.; Strelnikova, I. Extended observations of polar mesosphere winter echoes over Andøya (69° N) using MAARSY. *J. Geophys. Res. Atmos.* **2015**, *120*, 8216–8226. [CrossRef]
5. Röttger, J.; La Hoz, C. Characteristics of polar mesosphere summer echoes (PMSE) observed with the EISCAT 224 MHz radar and possible explanations of their origin. *J. Atmos. Terr. Phys.* **1990**, *52*, 893–906. [CrossRef]
6. Sharma, P.; Dalin, P.; Mann, I. Towards a Framework for Noctilucent Cloud Analysis. *Remote Sens.* **2019**, *11*, 2743. [CrossRef]
7. McCrea, I.; Aikio, A.; Alfonsi, L.; Belova, E.; Buchert, S.; Clilverd, M.; Engler, N.; Gustavsson, B.; Heinselman, C.; Kero, J.; et al. The science case for the EISCAT_3D radar. *Prog. Earth Planet. Sci.* **2015**, *2*, 21. [CrossRef]
8. Mann, I.; Häggström, I.; Tjulin, A.; Rostami, S.; Anyairo, C.C.; Dalin, P. First wind shear observation in PMSE with the tristatic EISCAT VHF radar. *J. Geophys. Res. Space Phys.* **2016**, *121*, 11271–11281. [CrossRef]
9. Fisher, R.A. The use of multiple measurements in taxonomic problems. *Ann. Eugen.* **1936**, *7*, 179–188. [CrossRef]
10. Koutroumbas, K.; Theodoridis, S. *Pattern Recognition*, 4th ed.; Wiley: Hoboken, NJ, USA, 2008.
11. Bera, A.K.; Premaratne, G. *Modeling Asymmetry and Excess Kurtosis in Stock Return Data*; Elsevier: Amsterdam, The Netherlands, 2000.
12. Westfall, P.H. Kurtosis as Peakedness, 1905–2014. R.I.P. *Am. Stat.* **2014**, *68*, 191–195. [CrossRef] [PubMed]
13. Lehtinen, M.S.; Huuskonen, A. General incoherent scatter analysis and GUISDAP. *J. Atmos. Terr. Phys.* **1996**, *58*, 435–452. [CrossRef]

14. Gordon, W.E. Incoherent Scattering of Radio Waves by Free Electrons with Applications to Space Exploration by Radar. *Proc. IRE* **1958**, *46*, 1824–1829. [CrossRef]
15. Wing, S.; Greenwald, R.A.; Meng, C.-I.; Sigillito, V.G.; Hutton, L.V. Neural networks for automated classification of ionospheric irregularities in HF radar backscattered signals. *Radio Sci.* **2003**, *38*, 1063. [CrossRef]

PAPER II

Segmentation of PMSE Data Using Random Forests

Jozwicki, D. and Sharma, P. and Mann, I. and Hoppe, U.-P.: Segmentation of PMSE Data Using Random Forests, Remote Sensing, doi: 10.3390/rs14132976, 2022

remote sensing

MDPI

Article

Segmentation of PMSE Data Using Random Forests

Dorota Jozwicki [1,*], Puneet Sharma [2], Ingrid Mann [1] and Ulf-Peter Hoppe [1]

[1] Department of Physics and Technology, UiT the Arctic University of Norway, 9019 Tromso, Norway; ingrid.b.mann@uit.no (I.M.); ulf-peter.hoppe@uit.no (U.-P.H.)
[2] Department of Automation and Process Engineering, UiT the Arctic University of Norway, 9019 Tromso, Norway; puneet.sharma@uit.no
* Correspondence: dorota.s.jozwicki@uit.no

Abstract: EISCAT VHF radar data are used for observing, monitoring, and understanding Earth's upper atmosphere. This paper presents an approach to segment Polar Mesospheric Summer Echoes (PMSE) from datasets obtained from EISCAT VHF radar data. The data consist of 30 observations days, corresponding to 56,250 data samples. We manually labeled the data into three different categories: PMSE, Ionospheric background, and Background noise. For segmentation, we employed random forests on a set of simple features. These features include: altitude derivative, time derivative, mean, median, standard deviation, minimum, and maximum values corresponding to neighborhood sizes ranging from 3 by 3 to 11 by 11 pixels. Next, in order to reduce the model bias and variance, we employed a method that decreases the weight applied to pixel labels with large uncertainty. Our results indicate that, first, it is possible to segment PMSE from the data using random forests. Second, the weighted-down labels technique improves the performance of the random forests method.

Keywords: space physics; upper atmosphere; random forests; segmentation

check for updates

Citation: Jozwicki, D.; Sharma, P.; Mann, I.; Hoppe, U.-P. Segmentation of PMSE Data Using Random Forests. *Remote Sens.* **2022**, *14*, 2976. https://doi.org/10.3390/rs14132976

Academic Editor: Michael E. Gorbunov

Received: 26 May 2022
Accepted: 16 June 2022
Published: 22 June 2022

1. Introduction

Polar Mesospheric Summer Echoes (PMSE) are radar echoes that form at about 75 to 95 km altitude at polar latitudes during the summer months. A recent long-term study of observations at 53.5 MHz made over two decades at 69 N (and many others) showed that they appear between mid-May and the end of August and are most likely to appear in June and July with an average occurrence of 95 percent [1].

Formation of PMSE requires the presence of turbulence, free electrons and charged aerosols. The charged aerosols themselves contain water ice and require the presence of very low temperature, the adequate water vapor [1–3], and nucleation centers to facilitate heterogeneous condensation. Meteor Smoke Particles (MSP) have been identified as the likely condensation nuclei. They result from meteor ablation and recondensation. In addition to them, the water vapor and the cold temperature at mid and high latitudes at the mesopause during the summer months allow the ice particles to form [4]. The combination of neutral air turbulence and the effect of negatively charged ice particles result in irregularities in the electron density distribution which generates the observed radar echoes, see, e.g., [1].

PMSE and Noctilucent Clouds (NLC) are observed during a similar time of the year and at similar heights and observations showed that the NLC tended to appear at the bottom of PMSE [2]. PMSE and NLC have the potential to reveal details about the atmosphere, including many changes during recent decades. An increase of NLC occurence over the years has already been noticed in observations from 1964 to 1988 [5] and one could argue that climate change may have reached the edge of space. To better understand this, systematic studies of PMSE over time can be helpful because they reveal the existence of water ice particles at the height where they are observed.

We aim to develop a method to investigate the thickness of PMSE, their shape, and the variation of PMSE height with time over the years. This requires the classification and segmentation of the radar images that contain PMSE. For our analysis, we employ random forests as a segmentation method. Next, we use a technique already developed by others [6] to select labeled data points. In this paper, we focus on segmenting PMSE signal in images of VHF (Very High Frequency) radar data from EISCAT (where EISCAT is the name of the research organization that operates the radar). The EISCAT VHF radar is located in Tromsø, Northern Norway and operates in the 224 MHz band. These images are time-height color plots of the radar data. For simplicity, we will employ the term "image" throughout this paper when referring to those plots. The parameter shown in all these images is the equivalent electron density, i.e., the number density of free electrons which would create an equivalent radar signal if it were due to incoherent scatter [7]. The equivalent electron density is very nearly proportional to the signal-to-noise ratio employed by many publications with PMSE observations [e.g., [8,9]]. For the purpose of this study, we have no use for any absolute value of PMSE strength. Therefore, we do not calibrate the data with all the steps which would be necessary to obtain an absolute radar reflectivity [10].

The paper is structured as follows: In Section 2, we outline the theory associated with the method used for segmentation of the PMSE signal and the metrics we used to evaluate its performance. In Section 3, we describe the procedure used for the segmentation of the PMSE signal. Section 4 highlights the results obtained from our analysis. In Section 5, we describe the results in detail and discuss key challenges. Finally, in Section 6, we outline the conclusions based on this study.

2. Theory

2.1. Random Forests

A way to characterize and segment data is to use a decision tree. A decision tree is represented as a directed graph $G = (V, E), E \subset V^2$, where V is a finite set of nodes split into three disjoint sets $V = D \cup C \cup T$, where D is decision node, C is chance node, and T is terminal or end node [11]. The different nodes represent different phases of a decision problem sequence [11]. In a decision node, based on observations about an item, we select an action. In Figure 1, there are two edges (d_1, c_1) and (d_1, d_2) originating from decision d_1 and one of edges lead to another decision node d_2. In a chance node which represents the probability of an outcome, we again select an edge randomly. In Figure 1, there are two edges (c_1, t_1) and (c_1, t_2) originating from chance node c_1 and two edges (c_2, t_3) and (c_2, t_4) originating from chance node c_2. Terminal or end nodes (t_1, t_2, t_3, and t_4) represent the outcome of a sequence of actions. For instance, it could be an items target value (regression) or its category (classification).

Several decision tree algorithms exist in the literature. Algorithms such as: ID3 [12], C4.5 [13] and C5.0 [14] employ information gain (which uses the concept of entropy) for deciding on the features to use for split at each step in building the tree, whereas another decision tree algorithm, e.g., CART [15] uses Gini impurity for the splitting criterion.

Decision tree-based methods are easy to understand and interpret; however, they are not robust. For instance, a small change in data or noise in the features can lead to large change in the tree and their associated outputs [16]. This implies that decision tree might not generalize well for unseen data.

Random forests is a decision tree-based ensemble learning method that has several advantages, such as having a built-in estimate of generalization error, depending only on one or two tuning parameters, and providing a measure of importance of different features of data [17].

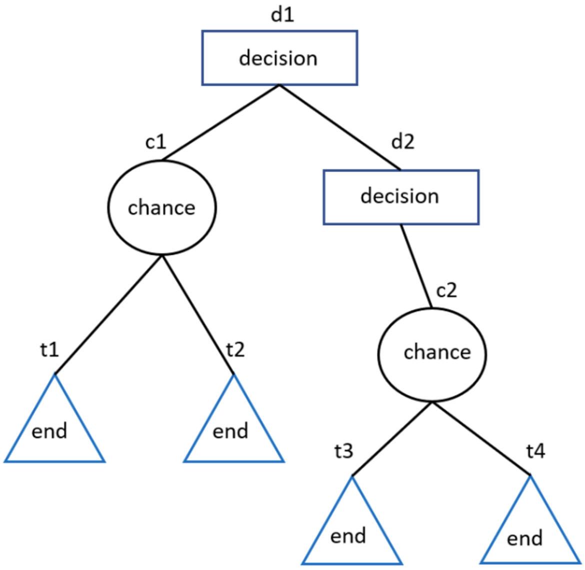

Figure 1. Example of a decision tree with decision, chance, and terminal or end nodes.

Random forests use Breiman's bootstrap aggregation or bagging technique in which several individual decision trees are trained on different subsets of the training dataset, also known as random sampling with replacement [17]. Furthermore, random forests use random subsets of available features for building the individual trees, also known as feature bagging. In the study by Probst et al. [18], it is suggested that the number of features to be randomly selected ($mtry$) for classification tasks usually have a default value of $\sqrt{p}$, where p is the total number of features. However, $mtry$ can be increased from its default value to improve the probability that at least one of randomly selected features is a strong predictor [18,19].

For regression, generalization error is measured using out-of-bag mean square error as:

$$MSE_{oob} = \frac{1}{N}\sum_{i=1}^{N}\left(y_i - \hat{f}_{oob}(x_i)\right)^2, \tag{1}$$

where $\hat{f}_{oob}(x_i)$ is out-of-bag prediction for bootstrap sample i, y_i is its actual outcome [17], and N is the number of samples. For classification, generalization error is measured using the out-of-bag error rate as:

$$E_{oob} = \frac{1}{N}\sum_{i=1}^{N}\left(I(y_i \neq \hat{f}_{oob}(x_i))\right), \tag{2}$$

i.e., it assigns 0 to error for a correct classification and 1 for an incorrect classification [17]. For example, if a PMSE sample is misclassified as a Noise sample, 1 is added to the sum in the out-of-bag error rate. If the PMSE sample is correctly classified as PMSE, 0 is added to the sum in the out-of-bag error rate. When we apply these equations to our data, x_i corresponds to a given sample i of our dataset. Then, $f(x_i)$ is the predicted label by the model for this given sample i, while y_i is the actual label of this sample. $\hat{f}_{oob}(x_i)$ means that we consider the predicted label by the model for the sample x_i in the out-of-bag dataset. Finally, $I(y_i \neq \hat{f}_{oob}(x_i))$ is a measure of how close y_i is to $\hat{f}_{oob}(x_i)$. It is a loss function defined to minimize the expected value of the loss. Bootstrapping ensures that individual decision trees are unique, which reduces the overall variance of the random forests method [20]. Finally, the prediction is obtained by aggregating the decisions of individual trees in the case of regression, or by taking the majority vote in the case of classification.

The importance of features is calculated based on the permutation importance method proposed by Breiman [21]. It is calculated as follows: first, we use out-of-bag samples for estimating the predictions from each tree with a selected feature f [17]. Second, the feature f is randomly permuted in out-of-bag samples and their predictions are calculated. Third, we calculate the difference between the prediction scores for the permuted and the original. Four, the average of differences over all trees within the random forest is an estimate of importance of the feature f.

Random forests methods are fast, simple, and easy to interpret via permutation importance [22]. They have been used in several applications such as: pattern recognition [23], object detection [24], remote sensing [25], and image segmentation [26].

2.2. Weighted-Down Technique

In their paper [6], Almeida et al. propose a novel method that can reduce both model bias and model variance. In their method, first, estimation of the pixel-wise label uncertainty of training data is performed. For instance, given a sample x_i with label y_i, its neighborhood uncertainty score is calculated as:

$$b_{x_i} = \frac{-C * \left(\frac{k_{y_i}}{k} \ln\left(\frac{k_{y_i}}{k} * \frac{k_{y_i}}{\sum d_{x_i}}\right)\right)}{-\sum_{j=1}^{C}\left(\frac{k_j}{k} \ln\left(\frac{k_j}{k} * \frac{k_j}{\sum d_j}\right)\right)}, \tag{3}$$

where C is the number of classes, k is the number of neighbors we consider for each sample (we employed $k = 11$ for our experiments), k_{y_i} is the number of neighbors with same label as x_i, k_j is the number of neighbors with class label y_j, and d_{x_i} represents a vector with normalized distances to the k_{y_i} neighbors with the same class label as x_i. For more details on the significance of the terms in the numerator and denominator of Equation (3), we refer the reader to the original paper [6]. Next, the training sample weights are adjusted such that the samples with high uncertainty are weighted-down and those with low uncertainty are weighted-up.

2.3. Metrics for Evaluation of Performance

In this section, we briefly discuss the different metrics used for evaluating the performance of methods used for data segmentation.

2.3.1. Classification Error

The classification error E is defined as the ratio of the number of misclassified samples, i.e., sum of the False Positives and False Negatives to that of the total number of samples. The values of classification error are in the range [0,1], where values closer to zero indicate fewer misclassifcations, hence better performance.

2.3.2. Logarithmic Loss

Logarithmic loss L is based on the predicted class probabilities and is considered to be a more refined metric than classification error [18,27]. Logarithmic loss is defined as:

$$L = \sum_{j=1}^{n} w_j log(1 + e^{-m_j}), \tag{4}$$

where n is number of samples, the weight for observation j is w_j and the weights are normalized to sum to 1, and m_j is scalar classification score [28].

2.3.3. Area Under ROC Curve (AUC)

A receiver operating characteristic (ROC) curve is a simple and visual way to summarize the performance of a classifier [29]. Assuming a two class prediction problem where the output is either positive or negative, an ROC curve is created by plotting true positive rate against false positive rate.

For the test samples, true positive rate is defined as the ratio of number of correct positive outcomes to that of all the positive samples [29]. The false positive rate is defined as the ratio of number of incorrect positive outcomes to that of all negative samples [29]. Finally, the area under the ROC Curve (AUC) gives us a scalar value in the range [0,1], which is used to measure the performance of a classifier. A random guessing classifier can give an AUC of 0.5; hence, any realistic classifier should have an AUC value more than 0.5 [29].

3. Method

In this section, we discuss the dataset used for our experiments. Next, we briefly explain the labeling procedure and the weighted-down technique employed in this study. After that, we explain the options used for random forests and finally the feature extracted from the data.

3.1. Dataset

The data we used for the analysis comes from EISCAT VHF radar located near Tromsø, Norway. The images contain measured backscattered power as a function of altitude and time. We use a height range of 75 to 95 km for our analysis, and observations typically last several hours. The height resolution is 0.30 to 0.45 km and the time resolution is of approximately one minute. We downloaded the data written in ASCII format from the Madrigal website. For further information about the 30 observation days used in this study, their dates and times are listed in Table 1.

Table 1. This table lists the observation dates, given in (day. month. year), that are used for this study. The observation time is given in Universal time (UTC) in the format (hour: minutes: seconds).

Dates	**Start Time in UTC**	**End Time in UTC**
(dd:mm:yyyy)	**(hh:mm:ss)**	**(hh:mm:ss)**
28 June 2008	07:58:33	08:36:18
30 June 2008	07:59:38	12:07:30
02 July 2008	10:24:30	11:59:02
10 June 2009	09:03:42	11:56:09
14 July 2009	08:19:33	11:33:15
16 July 2009	08:47:30	10:06:26
17 July 2009	07:49:44	11:59:30
30 July 2009	12:15:29	15:59:08
06 July 2010	07:00:30	23:59:30
07 July 2010	00:00:30	21:59:27
08 July 2010	09:00:42	12:59:03
09 July 2010	09:00:24	12:59:09
01 June 2011	08:34:31	10:02:07
08 June 2011	07:23:50	13:01:07
09 June 2011	08:01:45	12:59:26
12 June 2012	07:13:31	23:59:28
29 June 2012	10:21:57	10:30:04
11 July 2012	07:54:57	13:09:40
13 June 2013	07:12:33	08:59:26
28 June 2013	07:02:43	12:58:28
12 July 2013	00:00:28	21:58:28
27 July 2013	08:56:36	13:05:14
27 June 2014	09:03:48	12:59:38
01 July 2014	09:00:36	13:00:24
22 July 2014	22:26:33	23:59:28
23 July 2014	00:00:28	09:26:28
10 August 2015	09:14:40	16:12:28
12 August 2015	20:04:40	23:59:28
13 August 2015	00:00:28	01:59:26
20 August 2015	00:00:28	01:59:26

3.2. Labeling

We labeled the data manually and pixel by pixel, using the built-in Matlab Image Labeler App. In this way, a given labeled pixel belongs to one of three classes of interest, namely, PMSE, Ionospheric background, and Background noise. The regions of interest that are considered in this paper are discussed in more detail in our previous work [30]. The PMSE is characterized by a region where coherent scattering occurs, whereas the Ionosphere is a region where incoherent scattering occurs. The Noise region also displays incoherent scatter but because the signal is low the region has a lot of missing values (NaNs). As a result, it makes this region look different compared to the Ionosphere. The labeling was performed by visually recognizing a PMSE pattern. We based this on the fact that the amplitude of the PMSE looks greater than its surroundings, and it has a particular wavy structure that makes it different from the background. Figure 2 shows an example of the manual labeling process for a given image. We represented the original image as a heatmap, where the blue pixels represent the minimum values, the red pixels represent the maximum values, and the other colored pixels represent the values in between minimum and maximum. We use this same color code also later in this paper. This refers to the equivalent electron density from the standard GUISDAP analysis [31]. As for the labels part of Figure 2, the cyan colored pixels represent the Background noise, the yellow colored pixels belong to the Ionospheric background, and the dark red colored pixels represent the PMSE. Finally, the dark blue colored pixels represent unlabeled data. We partially labeled 18 images out of the 30, that contain a total of 56,250 samples (pixels). We used 60 percent of the labeled data for training (33,750 samples) and 40 percent for quantitative testing (22,500 samples). For qualitative testing, we used all the images. In addition, qualitative analysis was made by visual inspection of the segmented images by a domain expert.

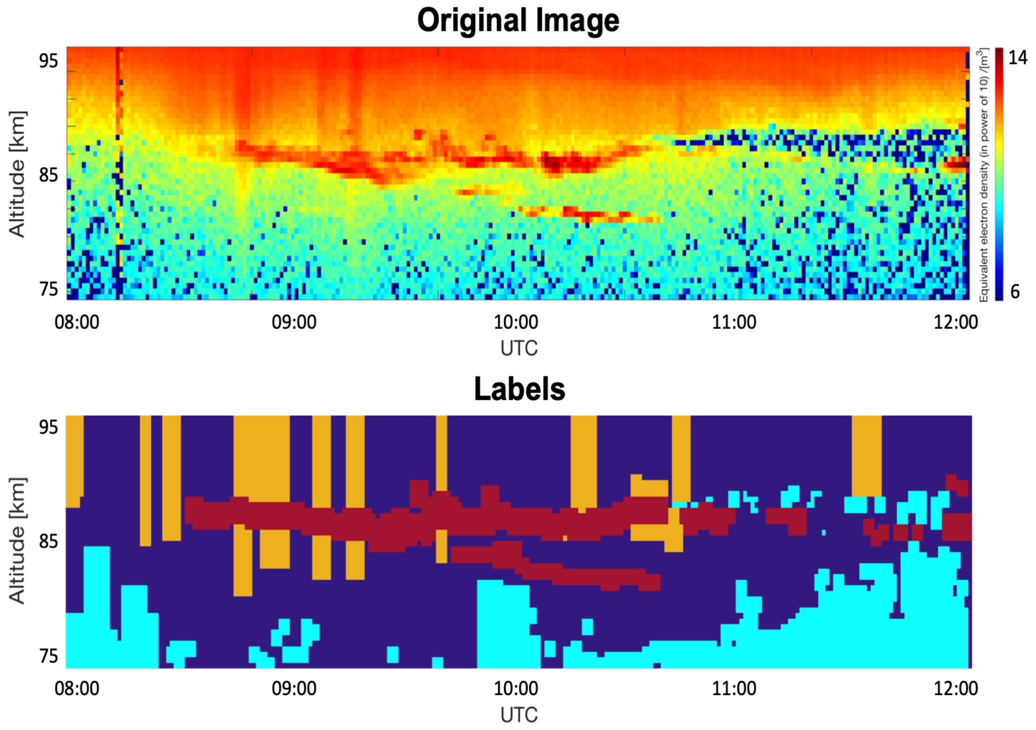

Figure 2. An example for manual labeling of the observations from 30 June 2008. The altitude range varies from 75 km to 95 km. The observation starts at 08:00 UTC and finishes at 12:00 UTC. The color scale in the original image represents the equivalent electron density to the power of 10, per cubic meter. In the labels part, the cyan, yellow and dark red color represent, respectively, the Background noise, Ionospheric background, and PMSE classes. The dark blue color represents unlabeled data.

3.3. Labels with Reduced Weighting

Next, we use the weighted-down technique described in Section 2.2 that aims to reduce both model bias and variance by reducing the weighting for pixel labels with large uncertainty and increasing it for labels with small uncertainty. For this, as a first step on the manually labeled data, for instance as shown in Figure 3a, we apply edge erosion to obtain a set of pixel labels that should be given lesser weight. As the labels we used in our experiment do not overlap, the edge erosion step generates a set of pixel labels along the label boundaries, as shown in Figure 3b. Finally, we calculate uncertainty scores based on Equation (3) in Section 2.2 for these pixel labels, and any pixel labels with non zero uncertainty scores are not kept for further analysis. Figure 3c shows the pixel labels after removing pixel labels with uncertainty, and Figure 3d shows the pixel labels that are removed from further analysis.

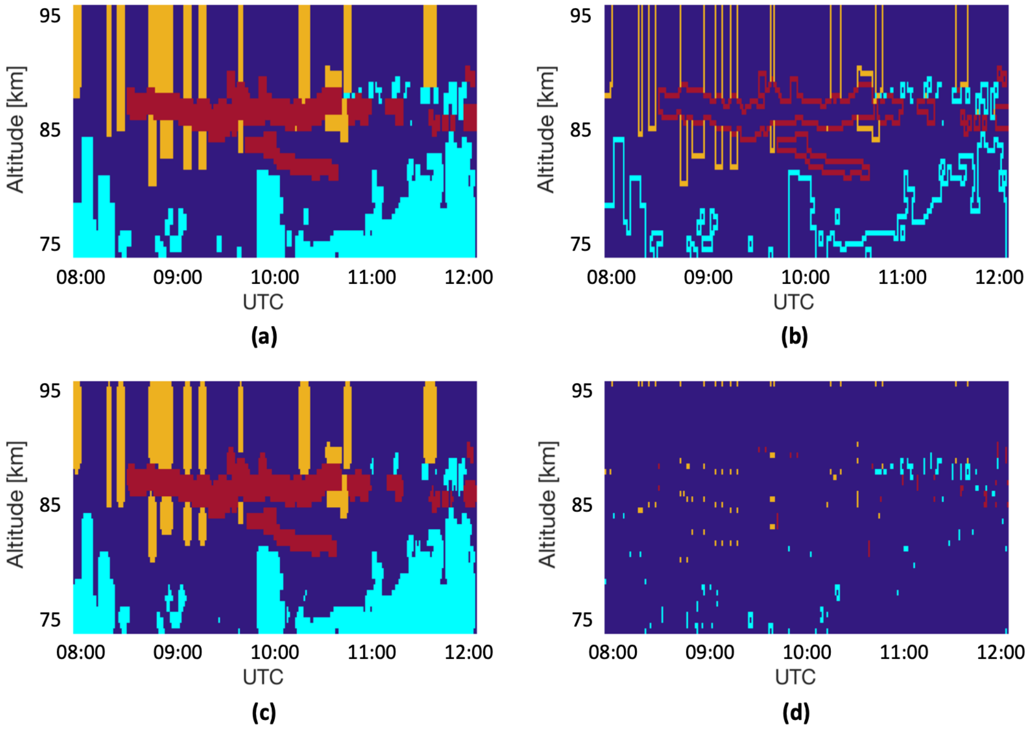

Figure 3. Prepossessing step with the labels: (**a**) shows the original labels, (**b**) shows the contours of the labels, (**c**) shows the image after removing the labeled pixels using weighted-down labels technique, and (**d**) shows the removed labeled pixels. For all four images, the red colored pixels belong to the PMSE class, the yellow pixels represent the Ionospheric background, and the cyan pixels belong to the Background noise class. Finally, the dark blue pixels represent unlabeled data. All of the plots have the same axes: the horizontal axis represents the time which starts at 8:00 UTC and finishes at 12:00 UTC. The vertical axis represents the altitude which ranges from 75 km to 95 km. The chosen observation day is 30 June 2008.

3.4. Random Forests Application

For our experiments, we employ random forests for training and evaluating the performance of data segmentation. For this we use MATLAB. The training is performed on an ensemble of bagged classification trees where number of trees in the forest is 500. In line with the study by Probst et al. [18] the number of trees is kept high, i.e., 500, samples are drawn with replacement, and p-value is used as the splitting rule. In addition, we enable surrogate decision split in order to allow the random forests to make a decision in case of missing data. This is done to accommodate for instances where we obtain missing amplitude values, i.e., NaNs in the data.

3.5. Feature Extraction

For each pixel, we extracted a dataset of features which is used as input together with its label. For each pixel we calculate features such as: mean, standard deviation, median, minimum and maximum values associated with neighborhoods ranging in sizes 3 × 3, 5 × 5, 7 × 7, 9 × 9, and 11 × 11 pixels where the pixel is at the center. In addition, we compute vertical and horizontal Gradient magnitudes using Sobel kernels for filter sizes 3 × 3, 5 × 5, 7 × 7, and 9 × 9, see [32]. Horizontal gradient operators calculate the time derivatives, and vertical gradient operators calculate the altitude derivatives. Furthermore, for each pixel its altitude and amplitude are included as features. This generates a feature vector with 35 dimensions. We plotted the different features extracted from the data in Figure 4 for the given observation day, 30 June 2008, except for altitude which is not illustrated in this figure. In the figure, the image in the first row and column represents the normalized amplitude. Then, from left to right and from top to bottom, the four next images represent the vertical gradient magnitudes for filter sizes of 3 × 3, 5 × 5, 7 × 7, and 9 × 9 pixels. The following four images represent the horizontal gradient magnitudes for the same filter sizes. The next five images represent the mean values for filters filter sizes of 3 × 3, 5 × 5, 7 × 7, 9 × 9, and 11 × 11 pixels. In a similar way, we represent the median values, the standard deviation, the minimum values, and finally the maximum values for the same filter sizes ranging from 3 × 3 to 11 × 11 pixels.

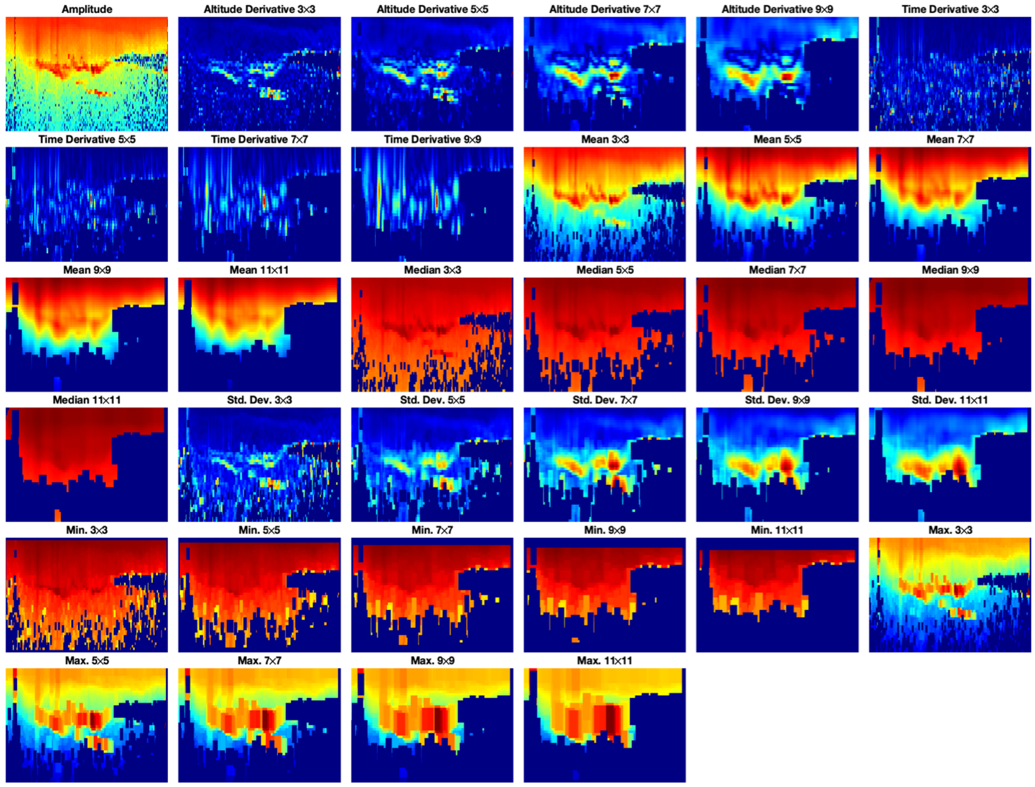

Figure 4. Visualization of the different features extracted from the data (with the exception of altitude) in the form of heat maps where red pixels correspond to highest values, blue pixels correspond to lowest values, and yellow pixels represent the values in between. The rows in the figure represent the different features, and the columns represent the different filter sizes that were used. All 34 plots have the same axes: the horizontal axis represents the time which starts at 8:00 UTC and finishes at 12:00 UTC. The vertical axis represents the altitude which ranges from 75 km to 95 km. The observation day chosen in this figure is 30 June 2008.

4. Results

The performance of random forests based on segmentation methods using different combinations of features, i.e., filter sizes, number of randomly selected features *mtry*, can be seen in Tables 2 and 3. While the results from using original labels are outlined in Table 2, the results we obtained using weighted-down labels (discussed in Section 3.3) are shown in Table 3. We evaluate the performance in terms of classification error for the test data, classification error for the out-of-bag (OOB) data samples, logarithmic error for the test data, logarithmic error for the out-of-bag (OOB) samples, Area under the ROC Curves (AUCs) for PMSE, Ionospheric background, and Noise. Note that for each filter size in the table, we use the following features: altitude derivative, time derivative, mean, median, standard deviation, minimum, and maximum. Additionally, we also use other features such as altitude and amplitude. This means that for each filter size, the feature vector has nine dimensions. At the filter size 11 × 11, the gradient filter is 9 × 9. For one filter size, e.g., 3 × 3 we use *mtry* = 3, 6, 9. After that, we use all filter sizes and select *mtry* = 5, 10, 15, 20, 25, 30 and 35, where 35 is the total length of the feature vector obtained from using all filter sizes.

The results for original labels can be seen in in Table 2 and the results for weighted-down labels can be found in Table 3. In both cases, the logarithmic error and logarithmic error OOB have the best performance for a filter size of 7 × 7 pixels with *mtry* = 9, and the worst one for all filter sizes and an *mtry* = 5. The classification error and the classification error OOB have the best results for the filter size 3 × 3 associated with *mtry* = 3 for original labels, or the filter size 7 × 7 associated with *mtry* = 9 and the filter size 11 × 11 with *mtry* = 6 for the weighted-down labels. The worst performance on the other hand was obtained in the case using all filter sizes and *mtry* = 5, and the filter size 9 × 9 in combination with *mtry* = 3. Almost all the AUC curves had the best performance for the combination of the filter size 6 × 6 with an *mtry* = 6. The only exception is the AUC Ion. Back. metric with original labels, for which the best performance was obtained for a filter size of 5 × 5 pixels with *mtry* = 6. We see that for all filter sizes, i.e., 35-dimensional feature vector and *mtry* = 5, 10, 15, 20, there are slight improvements in the performance for the scores associated with different evaluation metrics. This can possibly indicate that the performance of the random forests algorithm benefits from multi-resolution features extracted using the different filter sizes. However, the performance decreases when all the filter sizes are used and an *mtry* equal to 35.

Based on the results obtained in Tables 2 and 3, we choose the filter size 7 × 7 and *mtry* = 9 for qualitative analysis. We used this classification model on 30 images, out of which 12 were new data for the model. Figures 5–8 show the predicted labels for the classification model (with a filter size 7 × 7 and *mtry* = 9). In all four cases, the prediction of PMSE labels by the model looks poor. Figure 9 shows the predictor importance for both original (a) and weighted-down (b) labels. We can see that in both cases, the altitude is clearly dominating over the other features. The importance value in the vertical axis is using an arbitrary scale, and the results were averaged over 10 iterations. The error bars represent one standard deviation from the average.

For qualitative testing, the predicted labels were generated for all the 30 test images and for all the cases (all filter sizes and all *mtry* values) shown in both Tables 2 and 3. Although in Tables 2 and 3, the values of classification error, classification error OOB, logarithmic error and logarithmic error OOB are worse for all filter sizes and *mtry* = 5, these parameters gave us the best predicted labels. To illustrate our qualitative analysis, we use four examples. The predicted labels that we observed were the best (all filter sizes and *mtry* = 5) are shown in Figures 10–13. These figures show the predicted labels for the same time and dates as Figures 5–8. Figures 14 and 15 show the corresponding predictors importance for, respectively, original labels and weighted-down labels in the case of using all filter sizes together with *mtry* = 5. The results were averaged over 10 iterations, and the error bars represent one standard deviation from the average.

Table 2. Results of the classification using original labels. These values are obtained after five iterations of each experiment. Each field contains the mean over these five iterations, followed by one standard deviation.

		Logarithmic Error		**Logarithmic Error OOB**		**Classification Error**		**Classification Error OOB**		**AUC Ion. Back.**		**AUC Noise**		**AUC PMSE**	
Filter Size	***mtry***	**Mean**	**Std**	**Mean**	**Std**	**Mean**	**Std**	**Mean**	**Std**	**Mean**	**Std**	**Mean**	**Std**	**Mean**	**Std**
3 × 3	3	0.39468	0.00115	0.39455	0.00112	0.10498	0.00018	0.10926	0.00058	0.98396	0.00041	0.98103	0.00039	0.97001	0.00035
3 × 3	6	0.37179	0.00093	0.37093	0.00095	0.11519	0.00096	0.11285	0.00223	0.98883	0.00020	0.98663	0.00013	0.97768	0.00017
3 × 3	9	0.37161	0.00004	0.37035	0.00003	0.13725	0.00035	0.13305	0.00016	0.98667	0.00005	0.96972	0.00005	0.96404	0.00009
5 × 5	3	0.41333	0.00176	0.41349	0.00171	0.12525	0.00424	0.12593	0.00332	0.98593	0.00033	0.97600	0.00035	0.96480	0.00079
5 × 5	6	0.38747	0.00062	0.38795	0.00059	0.11493	0.00062	0.11739	0.00042	0.98933	0.00009	0.98159	0.00057	0.97461	0.00010
5 × 5	9	0.36193	0.00011	0.36262	0.00013	0.11379	0.00026	0.11519	0.00011	0.98901	0.00012	0.98134	0.00018	0.97612	0.00033
7 × 7	3	0.42243	0.00114	0.42247	0.00114	0.12452	0.00366	0.12899	0.00226	0.98280	0.00025	0.97158	0.00029	0.96459	0.00121
7 × 7	6	0.39271	0.00126	0.39313	0.00128	0.11445	0.00099	0.11632	0.00052	0.98836	0.00014	0.98084	0.00022	0.97499	0.00013
7 × 7	9	0.36027	0.00005	0.36120	0.00006	0.10833	0.00076	0.11041	0.00042	0.98652	0.00008	0.98213	0.00005	0.97406	0.00008
9 × 9	3	0.42842	0.00069	0.42829	0.00070	0.14273	0.00432	0.13902	0.00356	0.98083	0.00033	0.96983	0.00027	0.95969	0.00123
9 × 9	6	0.38914	0.00147	0.38861	0.00150	0.12105	0.00097	0.11740	0.00070	0.98594	0.00020	0.98062	0.00057	0.97007	0.00010
9 × 9	9	0.36235	0.00004	0.36162	0.00005	0.11938	0.00031	0.11632	0.00026	0.98276	0.00022	0.97944	0.00012	0.96780	0.00010
11 × 11	3	0.42290	0.00061	0.42310	0.00064	0.12776	0.00066	0.12760	0.00057	0.98121	0.00029	0.97027	0.00042	0.96548	0.00061
11 × 11	6	0.37492	0.00113	0.37509	0.00118	0.11085	0.00025	0.10928	0.00042	0.98337	0.00053	0.98262	0.00028	0.97105	0.00051
11 × 11	9	0.36253	0.00003	0.36265	0.00005	0.11887	0.00065	0.11831	0.00046	0.98089	0.00016	0.97877	0.00008	0.96882	0.00009
All Sizes	5	0.43433	0.00164	0.43477	0.00165	0.13891	0.01048	0.13772	0.00575	0.98039	0.00056	0.97096	0.00076	0.95898	0.00072
All Sizes	10	0.41768	0.00102	0.41817	0.00101	0.10884	0.00035	0.11096	0.00079	0.98535	0.00008	0.97749	0.00077	0.96591	0.00058
All Sizes	15	0.40385	0.00124	0.40429	0.00122	0.11200	0.00479	0.10980	0.00438	0.98752	0.00014	0.98091	0.00016	0.96857	0.00042
All Sizes	20	0.39397	0.00142	0.39433	0.00142	0.12100	0.00198	0.11975	0.00159	0.98850	0.00021	0.98234	0.00017	0.97017	0.00019
All Sizes	25	0.38476	0.00107	0.38505	0.00108	0.12963	0.00031	0.12798	0.00038	0.98852	0.00008	0.98334	0.00012	0.97092	0.00005
All Sizes	30	0.37788	0.00076	0.37810	0.00077	0.12929	0.00015	0.12834	0.00004	0.98817	0.00011	0.98329	0.00014	0.97074	0.00042
All Sizes	35	0.37096	0.00004	0.37113	0.00007	0.12963	0.00018	0.12967	0.00055	0.98651	0.00014	0.97192	0.00016	0.96238	0.00096

Table 3. Results of the classification using weighted-down labels. These values are obtained after five iterations of each experiment. Each field contains the mean over these five iterations, followed by one standard deviation.

		Logarithmic Error		**Logarithmic Error OOB**		**Classification Error**		**Classification Error OOB**		**AUC Ion. Back.**		**AUC Noise**		**AUC PMSE**	
Filter Size	***mtry***	**Mean**	**Std**	**Mean**	**Std**	**Mean**	**Std**	**Mean**	**Std**	**Mean**	**Std**	**Mean**	**Std**	**Mean**	**Std**
3 × 3	3	0.38950	0.00162	0.38927	0.00162	0.09828	0.00050	0.09697	0.00054	0.98806	0.00039	0.98300	0.00093	0.97536	0.00047
3 × 3	6	0.36683	0.00040	0.36659	0.00039	0.10360	0.00182	0.10437	0.00153	0.99176	0.00016	0.98826	0.00015	0.98212	0.00009
3 × 3	9	0.36459	0.00004	0.36427	0.00007	0.11532	0.00022	0.11578	0.00041	0.99063	0.00006	0.97384	0.00008	0.97110	0.00024
5 × 5	3	0.41009	0.00097	0.40947	0.00101	0.10974	0.00501	0.10625	0.00234	0.98778	0.00034	0.97695	0.00019	0.97437	0.00089
5 × 5	6	0.38508	0.00056	0.38407	0.00060	0.10504	0.00023	0.10131	0.00043	0.99152	0.00004	0.98119	0.00087	0.98128	0.00058
5 × 5	9	0.36253	0.00018	0.36111	0.00016	0.10598	0.00023	0.10088	0.00035	0.99095	0.00009	0.97723	0.00026	0.97715	0.00036
7 × 7	3	0.41946	0.00203	0.42020	0.00200	0.11242	0.00602	0.11725	0.00443	0.98662	0.00047	0.97677	0.00038	0.97086	0.00129
7 × 7	6	0.38950	0.00128	0.39053	0.00126	0.10166	0.00063	0.10692	0.00086	0.99168	0.00010	0.98475	0.00013	0.97987	0.00014
7 × 7	9	0.35469	0.00007	0.35640	0.00008	0.09460	0.00039	0.10087	0.00040	0.98998	0.00002	0.98615	0.00006	0.97921	0.00068
9 × 9	3	0.42364	0.00314	0.42302	0.00314	0.11726	0.00428	0.11962	0.00382	0.98395	0.00041	0.97341	0.00063	0.96720	0.00155
9 × 9	6	0.38314	0.00176	0.38282	0.00173	0.10587	0.00037	0.10529	0.00046	0.98849	0.00033	0.98271	0.00028	0.97598	0.00030
9 × 9	9	0.35714	0.00002	0.35719	0.00002	0.10516	0.00026	0.10440	0.00031	0.98648	0.00013	0.98298	0.00012	0.97465	0.00010
11 × 11	3	0.41998	0.00261	0.41864	0.00259	0.11798	0.00039	0.11496	0.00037	0.98394	0.00048	0.97410	0.00019	0.96995	0.00030
11 × 11	6	0.37212	0.00042	0.37113	0.00042	0.09978	0.00030	0.09628	0.00007	0.98557	0.00026	0.98462	0.00010	0.97410	0.00010
11 × 11	9	0.35753	0.00004	0.35661	0.00002	0.10448	0.00025	0.10290	0.00031	0.98402	0.00008	0.98029	0.00005	0.97274	0.00007
All Sizes	5	0.43022	0.00128	0.43013	0.00129	0.12580	0.01500	0.12236	0.00691	0.98521	0.00048	0.97142	0.00144	0.96726	0.00061
All Sizes	10	0.41479	0.00193	0.41452	0.00195	0.10435	0.00043	0.10037	0.00059	0.98886	0.00012	0.97768	0.00084	0.97209	0.00045
All Sizes	15	0.40186	0.00152	0.40145	0.00156	0.10167	0.00621	0.09960	0.00439	0.99041	0.00025	0.98078	0.00013	0.97444	0.00032
All Sizes	20	0.39105	0.00107	0.39054	0.00106	0.11213	0.00276	0.10939	0.00199	0.99138	0.00015	0.98215	0.00007	0.97609	0.00015
All Sizes	25	0.38112	0.00227	0.38047	0.00232	0.11830	0.00013	0.11614	0.00013	0.99157	0.00007	0.98331	0.00009	0.97686	0.00021
All Sizes	30	0.37277	0.00038	0.37199	0.00041	0.11913	0.00015	0.11693	0.00028	0.99121	0.00007	0.98287	0.00022	0.97694	0.00041
All Sizes	35	0.36581	0.00003	0.36490	0.00003	0.11985	0.00008	0.11747	0.00011	0.98922	0.00016	0.97259	0.00018	0.96867	0.00028

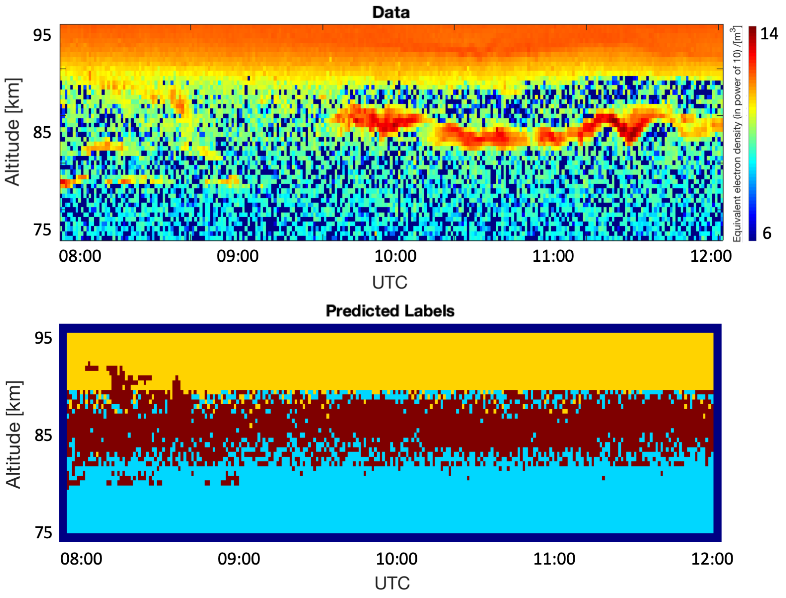

Figure 5. Results of segmentation using the random forests method with the 7 × 7 filter size, weighted-down labels, and $mtry = 9$. The weighted-down labels technique is taken from the study by [6]. The data are obtained from the observation day, 17 July 2009. The image on the top illustrates the original image where the color scale represents the equivalent electron density to the power of 10, per cubic meter. The image at the bottom represents the predicted labels. Yellow, cyan and dark red represents, respectively, the region of the image labeled as Ionospheric background, Background noise, and PMSE. The horizontal axis on both images represents the time which starts at 8:00 UTC and finishes at 12:00 UTC. The vertical axis represents the altitude which ranges from 75 km to 95 km.

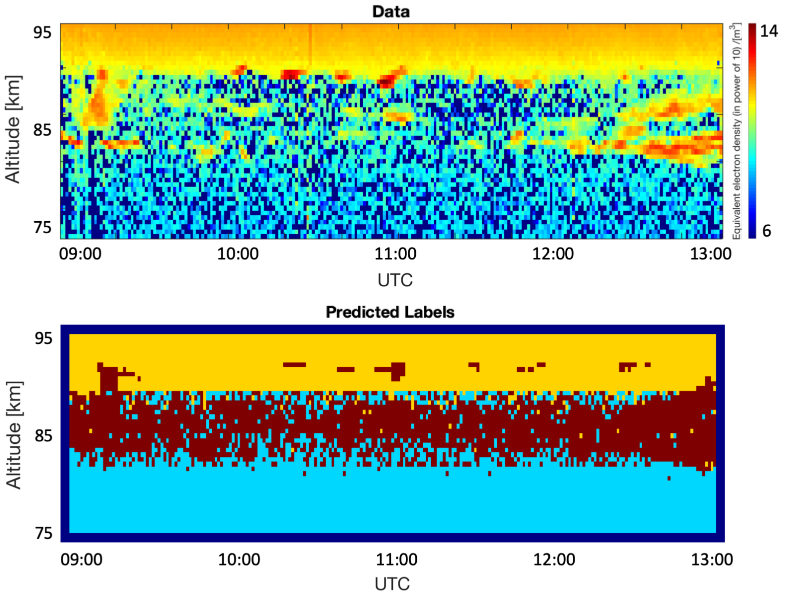

Figure 6. Results of segmentation using the random forests method with the 7 × 7 filter size, weighted-down labels, and $mtry = 9$. The weighted-down labels technique is taken from the study by [6]. The data are obtained from the observation day, 8 July 2010. The image on the top illustrates the original image where the color scale represents the equivalent electron density to the power of 10, per cubic meter. The image at the bottom represents the predicted labels. Yellow, cyan and dark red represents, respectively, the region of the image labeled as Ionospheric background, Background noise, and PMSE.The horizontal axis on both images represents the time which starts at 9:00 UTC and finishes at 13:00 UTC. The vertical axis represents the altitude which ranges from 75 km to 95 km.

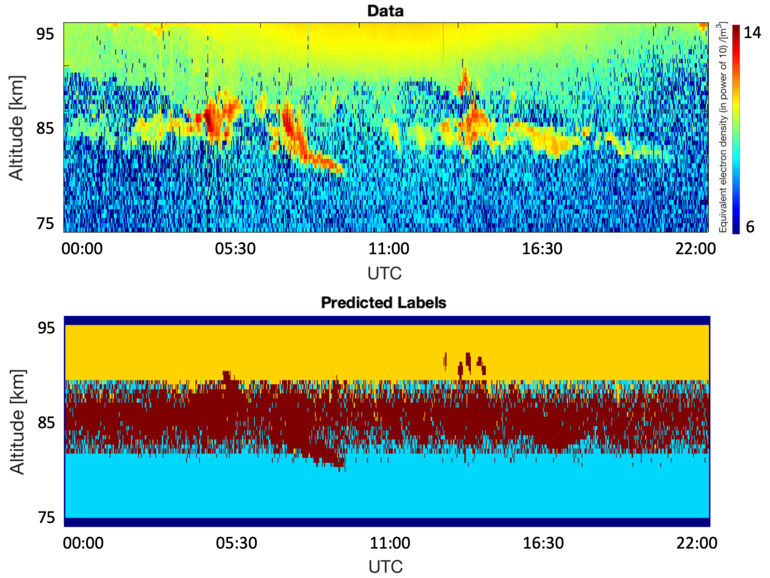

Figure 7. Results of segmentation using the random forests method with the 7 × 7 filter size, weighted-down labels, and $mtry = 9$. The weighted-down labels technique is taken from the study by [6]. The data are obtained from the observation day, 7 July 2010. The image on the top illustrates the original image where the color scale represents the equivalent electron density to the power of 10, per cubic meter. The image at the bottom represents the predicted labels. Yellow, cyan and dark red represents, respectively, the region of the image labeled as Ionospheric background, Background noise, and PMSE.The horizontal axis on both images represents the time which starts at 00:00 UTC and finishes at 22:00 UTC. The vertical axis represents the altitude which ranges from 75 km to 95 km.

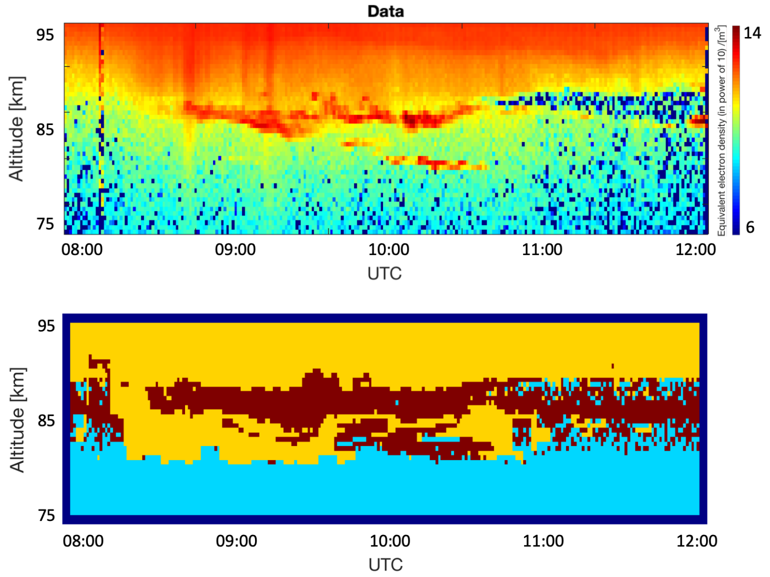

Figure 8. Results of segmentation using the random forests method with the 7 × 7 filter size, weighted-down labels, and $mtry = 9$. The weighted-down labels technique is taken from the study by [6]. The data are obtained from the observation day, 30 June 2008. The image on the top illustrates the original image where the color scale represents the equivalent electron density to the power of 10, per cubic meter. The image at the bottom represents the predicted labels. Yellow, cyan and dark red represents, respectively, the region of the image labeled as Ionospheric background, Background noise, and PMSE.The horizontal axis on both images represents the time which starts at 8:00 UTC and finishes at 12:00 UTC. The vertical axis represents the altitude which ranges from 75 km to 95 km.

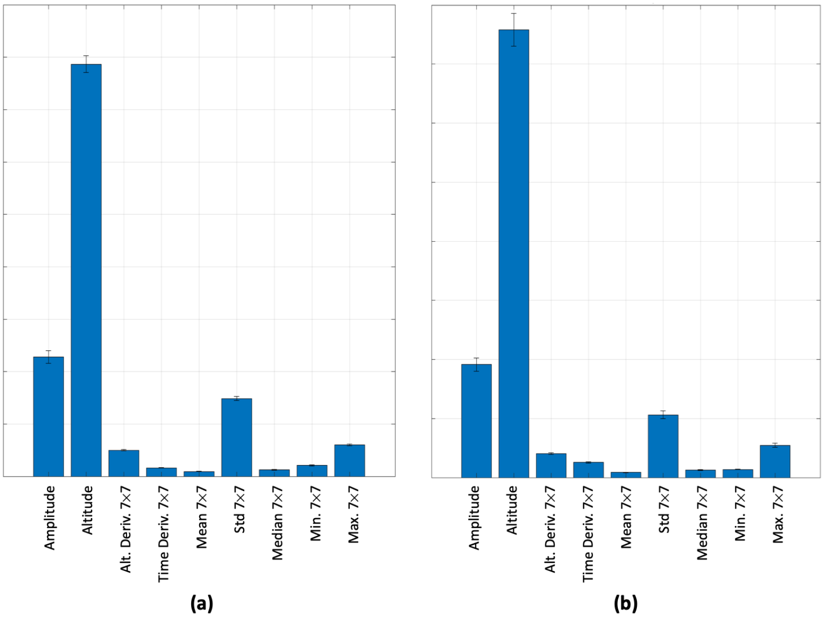

Figure 9. Predictor importance for random forests used on original (**a**) and weighted-down (**b**) labels with a 7 × 7 filter size and $mtry = 9$. The horizontal axis lists all the predictors, and the vertical axis shows their importance using an arbitrary scale. Higher values mean that the algorithm assigned to them a higher importance to classify the data efficiently. These values are averaged over 10 iterations, and the error bars represent one standard deviation from the average.

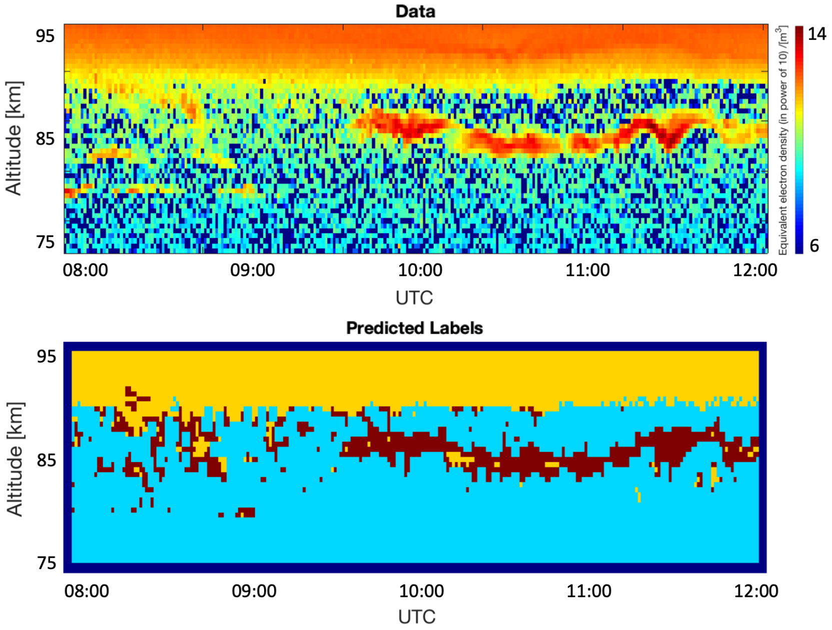

Figure 10. Results of segmentation using the random forests method ($mtry = 5$) and weighted-down labels technique from the study by [6]. The data are obtained from the observation day on the 17 July 2009. The image on the top illustrates the original image where the color scale represents the equivalent electron density to the power of 10, per cubic meter. The image at the bottom represents the predicted labels. Yellow, cyan and dark red represents, respectively, the region of the image labeled as Ionospheric background, Background noise, and PMSE.The horizontal axis on both images represents the time which starts at 7:50 UTC finishes at 12:00 UTC. The vertical axis represents the altitude which ranges from 75 km to 95 km.

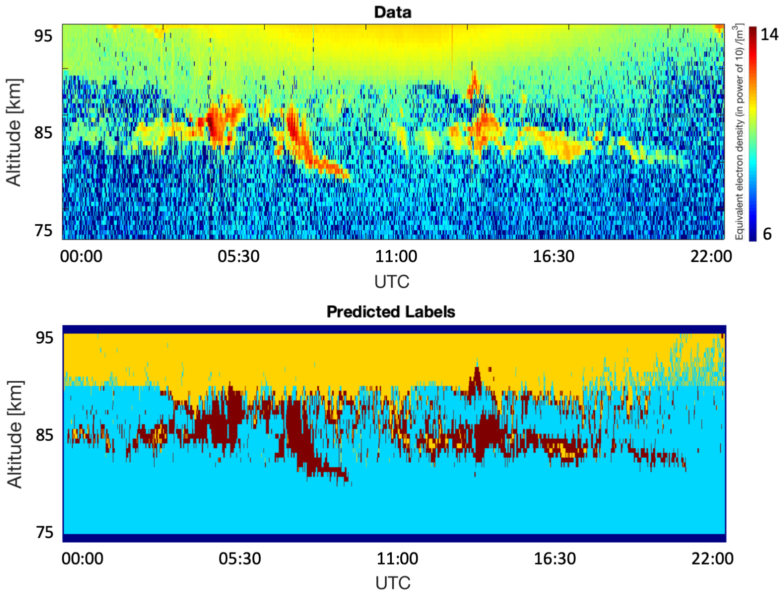

Figure 11. Results of segmentation using the random forests method ($mtry = 5$) and weighted-down labels technique from the study by [6]. The data are obtained from the observation day, 7 July 2010. The image on the top illustrates the original image where the color scale represents the equivalent electron density to the power of 10, per cubic meter. The image at the bottom represents the predicted labels. Yellow, cyan and dark red represent, respectively, the region of the image labeled as Ionospheric background, Background noise, and PMSE.The horizontal axis on both images represents the time which starts at 00:00 UTC and finishes at 22:00 UTC. The vertical axis represents the altitude which ranges from 75 km to 95 km.

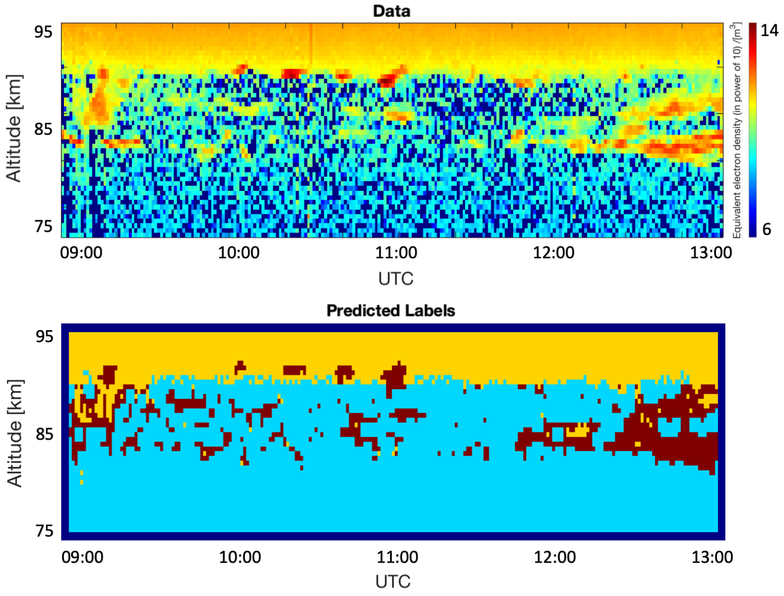

Figure 12. Results of segmentation using the random forests method ($mtry = 5$) and weighted-down labels technique from the study by [6]. The data are obtained from the observation day of 8 July 2010. The image on the top illustrates the original image where the color scale represents the equivalent electron density to the power of 10, per cubic meter. The image at the bottom represents the predicted labels. Yellow, cyan and dark red represents, respectively, the region of the image labeled as Ionospheric background, Background noise, and PMSE. The horizontal axis on both images represents the time which starts at 09:00 UTC and finishes at 13:00 UTC. The vertical axis represents the altitude which ranges from 75 km to 95 km.

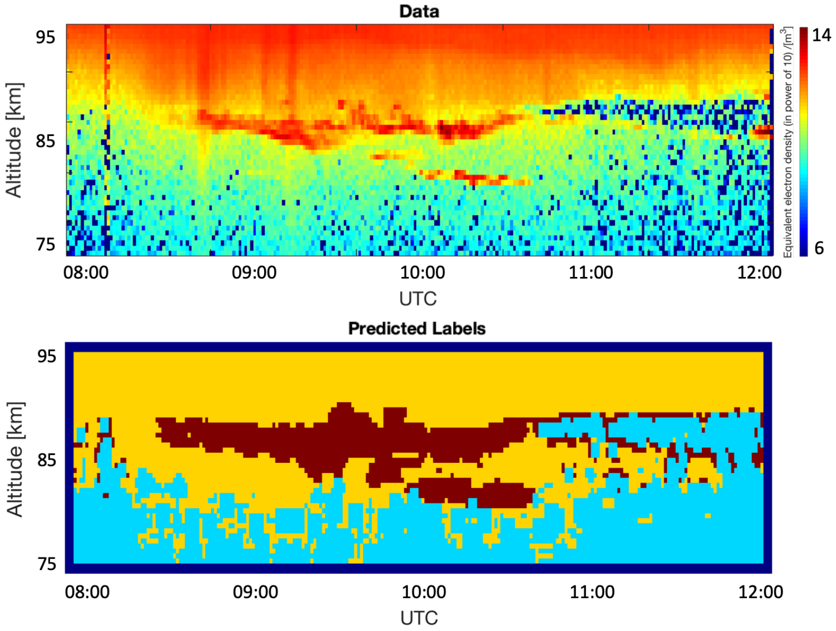

Figure 13. Results of segmentation using the random forests method ($mtry = 5$) and weighted-down labels technique from the study by [6]. The data are obtained from the observation day, 30 June 2008. The image on the top illustrates the original image where the color scale represents the equivalent electron density to the power of 10, per cubic meter. The image at the bottom represents the predicted labels. Yellow, cyan and dark red represents, respectively, the region of the image labeled as Ionospheric background, Background noise, and PMSE.The horizontal axis on both images represents the time which starts at 8:00 UTC and finishes at 12:00 UTC. The vertical axis represents the altitude which ranges from 75 km to 95 km.

In Table 3, the evaluation scores for all combinations of filter sizes are slightly better than the evaluation scores in Table 2. This can imply that by employing weighted-down labels (discussed in Section 3.3), we can achieve a reduction in both model bias and variance, hence, leading to an improved performance. Although the performance gain achieved using weighted-down labels technique from the study by [6] is marginal, for further studies involving data labels beyond the three categories used in this paper, the gains achieved using the weighted-down labels technique could be significant.

When all 35 features are used as predictors, i.e., $mtry = 35$, one can see that their importance is varying with different filter sizes. We can note that when original labels are used for the random forests algorithm, the predictor importance is different (as shown in Figure 14) as compared to when we use the weighted-down labels (as shown in Figure 15). The importance of all the different predictors is plotted on an arbitrary scale which is linear and relative. One can note that in Figure 14, the most important feature is altitude which is something that is also used in practice to determine if a signal is PMSE. After that, the second most important feature is the 11 × 11 minimum value, followed by the 9 × 9 minimum value, and then the 11 × 11 mean value, and so on. The importance of features is similar for the weighted-down labels case as shown in Figure 15, where the first 6 predictors are the same. After that, the order is slightly different. This implies that features extracted across multiple scales, i.e., ranging from 3 × 3 to 11 × 11 can play an important role in improving the prediction of the random forests. Finally, one can see that in Figure 15, the error bars are slightly smaller using weighted-down labels compared to Figure 14, where original labels are used.

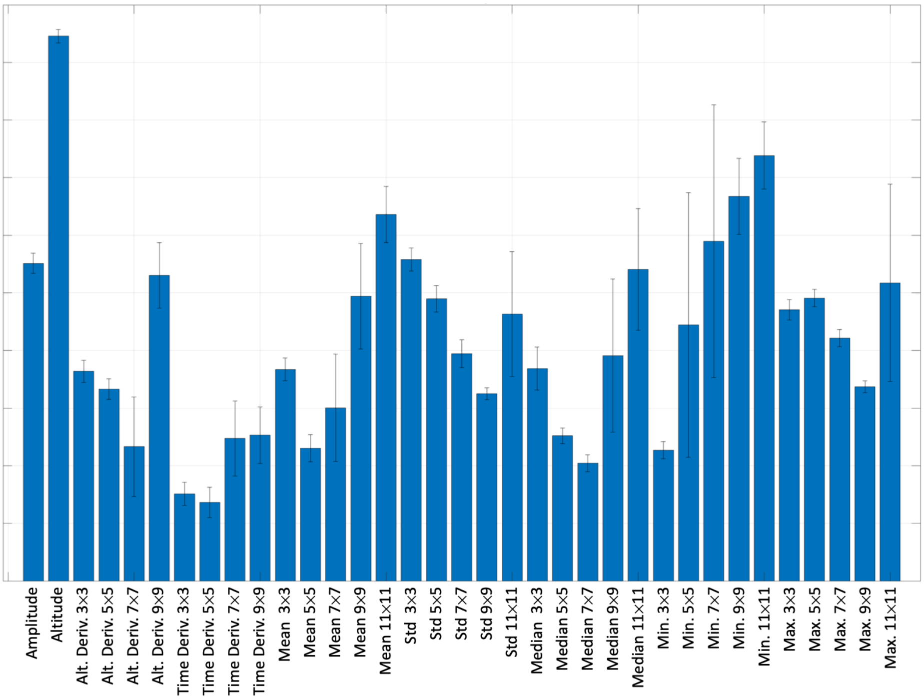

Figure 14. Predictor importance for random forests used on original labels with all filter sizes and $mtry = 5$. The horizontal axis lists all the predictors, and the vertical axis shows their importance using an arbitrary scale.Higher values mean that the algorithm assigned to them a higher importance to classify the data efficiently. These values are averaged over 10 iterations, and the error bars represent one standard deviation from the average.

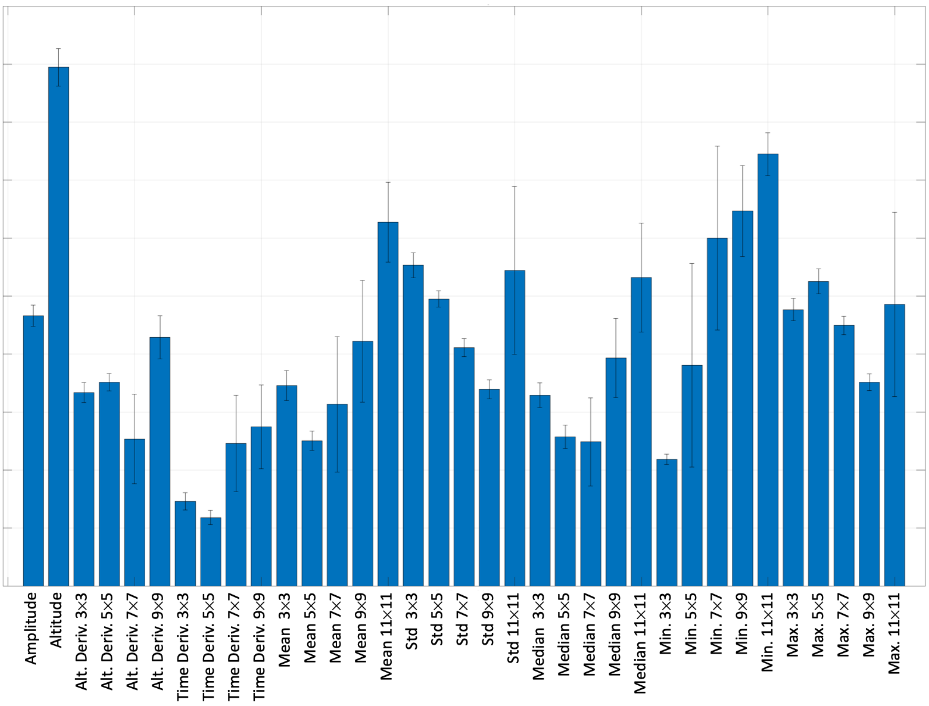

Figure 15. Predictor importance for random forests used on weighted-down labels with all filter sizes and $mtry = 5$. The horizontal axis lists all the predictors, and the vertical axis shows their importance using an arbitrary scale. Higher values mean that the algorithm assigned to them a higher importance to classify the data efficiently. These values are averaged over 10 iterations, and the error bars represent one standard deviation from the average.

5. Discussion

In the case with the filter size 7 × 7 and $mtry = 9$ which quantitatively gives the best results, the segmentation results as shown in Figures 5–8 are worse. This could be due to its poor generalization to new unseen data. Based on the segmentation results obtained in Figures 10–13, we can note that using the random forests for all filter sizes with $mtry = 5$ and weighted-down labels technique from the study by Almeida et al. [6], it is possible to segment the data into the three different categories of interest. Furthermore, $mtry = 5$ is in line with the study by Probst et al. [18], which suggests that the recommended number of predictors is approximately equal to the square root value of the total number of features, which is 35 in our case.

In one of the images used for qualitative testing, for instance Figure 13, we notice an unusual case where part of the PMSE signal is not accurately segmented. We observe that some pixels were classified as PMSE at the border between the Ionospheric background and the Background noise. This happens around 11:00 to 12:00 UTC, while we can clearly see that there is no PMSE at that time on the original image above. We think this is the result of the fact that PMSE are usually having a pattern elongated horizontally. Because of this, the model might make the horizontal patterns stand out more, and therefore give more importance to the vertical gradients, hence to the altitude derivatives. This is something that Figures 14 and 15 confirm, where altitude derivatives were given more importance than the time derivatives. In the future, we aim to use this segmentation approach to extract the PMSE signal from the vast dataset of EISCAT observations in order to analyze in detail the structures of the PMSE signals and compare the PMSE signals from different time periods in the solar cycle.

6. Conclusions

This study outlines a framework to segment PMSE from the Ionospheric background and the Background noise in images obtained from EISCAT VHF radar data. We manually labeled the data into three different categories: PMSE, Ionospheric background, and Background noise, representing in total a dataset of 56,250 labeled samples. For segmentation, we employed random forests on a set of simple features. These features include: altitude derivative, time derivative, mean, median, standard deviation, minimum, and maximum values corresponding to neighborhood sizes ranging from 3 by 3 to 11 by 11. We also used the amplitude and altitude additionally as features. Next, we used a weighting-down technique on the data labels to reduce the model bias and variance.

First, our results show that it is possible to extract PMSE signal from the data, when using all sizes for feature extraction and $mtry = 5$. Second, by employing the weighted-down labels technique, we note an improvement in the performance of random forests.

For future studies, PMSE could be investigated over a broader dataset comprising several years of observations for one complete solar cycle. Information such as the thickness or shape of PMSE over the years could also be analyzed to gain further understanding of its origin and evolution.

Author Contributions: Conceptualization, D.J., P.S., I.M. and U.-P.H.; Data curation, D.J.; Funding acquisition, I.M.; Investigation, D.J. and P.S.; Project administration, I.M.; Software, D.J. and P.S.; Supervision, P.S., I.M. and U.-P.H.; Validation, P.S., I.M. and U.-P.H.; Writing—original draft, D.J.; Writing—review & editing, D.J., P.S., I.M. and U.-P.H. All authors have read and agreed to the published version of the manuscript.

Funding: This work was carried out within a project funded by Research Council of Norway, NFR 275503. The Norwegian participation in EISCAT and EISCAT3D is funded by Research Council of Norway, through research infrastructure grant 245683. The EISCAT International Association is supported by research organizations in Norway (NFR), Sweden (VR), Finland (SA), Japan (NIPR and STEL), China (CRIPR), and the United Kingdom (NERC).

Data Availability Statement: EISCAT VHF and UHF data are available under http://www.eiscat.se/madrigal/ (accessed on 15 June 2022).

Acknowledgments: The authors thank the Research Council of Norway for the funding and the EISCAT International Association which is supported by research organizations in Norway (NFR), Sweden (VR), Finland (SA), Japan (NIPR and STEL), China (CRIPR), and the United Kingdom (NERC) for making the data easily accessible.

Conflicts of Interest: The authors declare no conflict of interest. The funders had no role in the design of the study; in the collection, analyses, or interpretation of data; in the writing of the manuscript, or in the decision to publish the results.

References

1. Latteck, R.; Renkwitz, T.; Chau, J.L. Two decades of long-term observations of polar mesospheric echoes at 69°N. *J. Atmos. Sol.-Terr. Phys.* **2021**, *216*, 105576. [CrossRef]
2. Cho, J.Y.N.; Röttger, J. An updated review of polar mesosphere summer echoes: Observation, theory, and their relationship to noctilucent clouds and subvisible aerosols. *J. Geophys. Res. Atmos.* **1997**, *102*, 2001–2020. [CrossRef]
3. Rapp, M.; Lübken, F.J. Polar mesosphere summer echoes (PMSE): Review of observations and current understanding. *Atmos. Chem. Phys.* **2004**, *4*, 2601–2633. [CrossRef]
4. Avaste, O. Noctilucent clouds. *J. Atmos. Terr. Phys.* **1993**, *55*, 133–143. [CrossRef]
5. Gadsden, M. A secular change in noctilucent cloud occurrence. *J. Atmos. Terr. Phys.* **1990**, *52*, 247–251. [CrossRef]
6. Almeida, M.; Zhuang, Y.; Ding, W.; Crouter, S.E.; Chen, P. Mitigating Class-Boundary Label Uncertainty to Reduce Both Model Bias and Variance. *ACM Trans. Knowl. Discov. Data* **2021**, *15*, 27. [CrossRef]
7. Mann, I.; Häggström, I.; Tjulin, A.; Rostami, S.; Anyairo, C.C.; Dalin, P. First wind shear observation in PMSE with the tristatic EISCAT VHF radar. *J. Geophys. Res. Space Phys.* **2016**, *121*, 11271–11281. [CrossRef]
8. Ecklund, W.L.; Balsley, B.B. Long-term observations of the Arctic mesosphere with the MST radar at Poker Flat, Alaska. *J. Geophys. Res. Space Phys.* **1981**, *86*, 7775–7780. [CrossRef]
9. Hoppe, U.P.; Hall, C.; Röttger, J. First observations of summer polar mesospheric backscatter with a 224 MHz radar. *Geophys. Res. Lett.* **1988**, *15*, 28–31. [CrossRef]
10. Hocking, W.; Rüster, R.; Czechowsky, P. Absolute reflectivities and aspect sensitivities of VHF radio wave scatterers measured with the SOUSY radar. *J. Atmos. Terr. Phys.* **1986**, *48*, 131–144. [CrossRef]
11. Kaminski, B.; Jakubczyk, M.; Przemyslaw, S. A framework for sensitivity analysis of decision trees. *Cent. Eur. J. Oper. Res.* **2018**, *26*, 135–159. [CrossRef] [PubMed]
12. Quinlan, J.R. Induction of Decision Trees. *Mach. Learn.* **1986**, *1*, 81–106. [CrossRef]
13. Quinlan, J.R. *C4.5: Programs for Machine Learning*; Morgan Kaufmann Publishers Inc.: San Francisco, CA, USA, 1993.
14. Kuhn, M.; Johnson, K. *Applied Predictive Modeling*; Springer: New York, NY, USA, 2013.
15. Breiman, L.; Friedman, J.H.; Olshen, R.A.; Stone, C.J. *Classification and Regression Trees*; Chapman and Hall/CRC: Monterey, CA, USA, 1984.
16. James, G.; Witten, D.; Hastie, T.; Tibshirani, R. *An Introduction to Statistical Learning: With Applications in R*; Springer Publishing Company, Incorporated: New York, NY, USA, 2014.
17. Cutler, A.; Cutler, D.R.; Stevens, J.R. Random Forests. In *Ensemble Machine Learning: Methods and Applications*; Zhang, C., Ma, Y., Eds.; Springer: Boston, MA, USA, 2012; pp. 157–175. [CrossRef]
18. Probst, P.; Wright, M.N.; Boulesteix, A.L. Hyperparameters and tuning strategies for random forest. *WIREs Data Min. Knowl. Discov.* **2019**, *9*, e1301. [CrossRef]
19. Grömping, U. Variable Importance Assessment in Regression: Linear Regression versus Random Forest. *Am. Stat.* **2009**, *63*, 308–319. [CrossRef]
20. Karpievitch, Y.V.; Hill, E.G.; Leclerc, A.P.; Dabney, A.R.; Almeida, J.S. An Introspective Comparison of Random Forest-Based Classifiers for the Analysis of Cluster-Correlated Data by Way of RF++. *PLoS ONE* **2009**, *4*, e7087. [CrossRef]
21. Breiman, L. Random Forests. *Mach. Learn.* **2001**, *45*, 5–32. [CrossRef]
22. Tyralis, H.; Papacharalampous, G.; Langousis, A. A Brief Review of Random Forests for Water Scientists and Practitioners and Their Recent History in Water Resources. *Water* **2019**, *11*, 910. [CrossRef]
23. Ristin, M.; Guillaumin, M.; Gall, J.; Van Gool, L. Incremental Learning of Random Forests for Large-Scale Image Classification. *IEEE Trans. Pattern Anal. Mach. Intell.* **2016**, *38*, 490–503. [CrossRef]
24. Gall, J.; Razavi, N.; Van Gool, L. An Introduction to Random Forests for Multi-class Object Detection. In *Outdoor and Large-Scale Real-World Scene Analysis*; Dellaert, F., Frahm, J.M., Pollefeys, M., Leal-Taixé, L., Rosenhahn, B., Eds.; Springer: Berlin/Heidelberg, Germany, 2012; pp. 243–263.
25. Belgiu, M.; Drăguţ, L. Random forest in remote sensing: A review of applications and future directions. *ISPRS J. Photogramm. Remote Sens.* **2016**, *114*, 24–31. [CrossRef]
26. Mahapatra, D. Analyzing Training Information From Random Forests for Improved Image Segmentation. *IEEE Trans. Image Process.* **2014**, *23*, 1504–1512. [CrossRef]
27. Probst, P.; Boulesteix, A.L. To Tune or Not to Tune the Number of Trees in Random Forest. *J. Mach. Learn. Res.* **2017**, *18*, 6673–6690.

28. MathWorks. Available online: https://se.mathworks.com/help/stats/compactclassificationensemble.loss.html (accessed on 8 July 2021).
29. Fawcett, T. An introduction to ROC analysis. *Pattern Recognit. Lett.* **2006**, *27*, 861–874. [CrossRef]
30. Jozwicki, D.; Sharma, P.; Mann, I. Investigation of Polar Mesospheric Summer Echoes Using Linear Discriminant Analysis. *Remote Sens.* **2021**, *13*, 522. [CrossRef]
31. Lehtinen, M.S.; Huuskonen, A. General incoherent scatter analysis and GUISDAP. *J. Atmos. Terr. Phys.* **1996**, *58*, 435–452. [CrossRef]
32. Doug Morris, R.R. Sobel gradient kernels (3 × 3, 5 × 5, 7 × 7, 9 × 9). Available online: https://imagej.nih.gov/nih-image/download/user-macros/slowsobel.macro (accessed on 11 May 2021).

PAPER III

Polar Mesospheric Summer Echo (PMSE) Multilayer Properties During Solar Maximum and Solar Minimum

Jozwicki, D. and Sharma, P. and Huyghebaert, D. and Mann, I.: Polar mesospheric summer echo (PMSE) multilayer properties during the solar maximum and solar minimum, Annales Geophysicae, doi: 10.5194/angeo-42-431-2024, 2024

Ann. Geophys., 42, 431–453, 2024
https://doi.org/10.5194/angeo-42-431-2024

Annales Geophysicae
Open Access

Polar mesospheric summer echo (PMSE) multilayer properties during the solar maximum and solar minimum

Dorota Jozwicki[1], **Puneet Sharma**[2], **Devin Huyghebaert**[1], **and Ingrid Mann**[1]

[1]Department of Physics and Technology, UiT the Arctic University of Norway, 9019 Tromsø, Norway
[2]Department of Automation and Process Engineering, UiT the Arctic University of Norway, 9019 Tromsø, Norway

Correspondence: Dorota Jozwicki (dorota.s.jozwicki@uit.no)

Received: 15 May 2023 – Discussion started: 1 June 2023
Revised: 25 July 2024 – Accepted: 26 August 2024 – Published: 11 November 2024

Abstract. Polar mesospheric summer echoes (PMSEs) are radar echoes that are measured in the upper atmosphere during the summer months and that can occur in several layers. In this study, we aimed to investigate the relationship between PMSE layers ranging from 80 to 90 km altitude and the solar cycle. We investigated 230 h of observations from the EISCAT very high frequency (VHF) radar located near Tromsø, Norway, from the years 2013, 2014 and 2015 during the solar maximum and the years 2019 and 2020 during the solar minimum and applied a previously developed classification model to identify PMSE layers. Our analysis focused on parameters such as the altitude, thickness and echo power in the PMSE layers, as well as the number of layers present. Our results indicate that the average altitude of PMSEs, the echo power in the PMSEs and the thickness of the layers are, on average, higher during the solar maximum than during the solar minimum. In the considered observations, the electron density at 92 km altitude and the echo power in the PMSEs are positively correlated with the thickness of the layers except for four multilayers at solar minimum. We infer that higher electron densities at ionospheric altitudes might be necessary to observe multilayered PMSEs. We observe that the thickness decreases as the number of multilayers increases. We compare our results with previous studies and find that similar results regarding layer altitudes were found in earlier studies using observations with other VHF radars. We also observed that the bottom layer in the different sets of multilayers almost always aligned with the noctilucent cloud (NLC) altitude reported by previous studies at 83.3 km altitude. Also, an interesting parallel is seen between the thickness of NLC multilayers and PMSE multilayers, where both NLCs and PMSEs have a similar distribution of layers greater than 1 km in thickness. Future studies that include observations over longer periods would make it possible to distinguish the influence of the solar cycle from possible other long-term trends.

1 Introduction

During the summer months, radars can measure a phenomenon in the upper atmosphere called polar mesospheric summer echoes (PMSEs). PMSEs are strong radar echoes that typically form at heights between 80 and 90 km and in regions of extremely cold temperatures. They are observed at mid-latitudes and high latitudes, and their height and thickness varies over time (Rapp and Lübken, 2004). Figure 1 shows a typical example of a PMSE event where these variations can be seen. The PMSE formation is linked to the presence of turbulence, free electrons and charged aerosols. The charged aerosols contain water ice, which requires the presence of low temperatures, sufficient water vapor and nucleation centers to foster heterogeneous condensation (Latteck et al., 2021; Cho and Röttger, 1997; Rapp and Lübken, 2004). The mesopause, which marks the boundary between the mesosphere and the thermosphere, is characterized by the lowest temperatures in the atmosphere. Such low temperatures at PMSE altitudes are conducive to ice formation. Meteor smoke particles (MSPs), produced by meteor ablation and recondensation have been proposed to be potential condensation nuclei along with several other potential nuclei (Rapp and Thomas, 2006). In addition to nucleation centers, the presence of water vapor and the low temperatures at the mid- and high-latitude mesopause during the summer months create conditions favorable for ice particle formation (Avaste, 1993). Cold temperatures and water ice are known to be at the origin of another phenomenon called noctilucent cloud (NLC) (Schäfer et al., 2020) that are, due to light, scattered at the ice particles observed from the ground. More generally, and when observed from space, the clouds of ice particles are denoted as polar mesospheric clouds (Fritts et al., 2019).

The PMSEs are formed through a process that involves the electrical charging of the ice particles and is, for instance, discussed by Rapp and Lübken (2004) and Latteck et al. (2021). They are strong radar echoes, and they result from reflections at inhomogeneities in the electron density when their spatial scales are of sizes comparable to half of the radar wavelength. Constructive interferences of the reflections result in high backscattered power and narrowly peaked power spectra. Such strong echoes are typically from turbulence in the partially ionized upper atmosphere. The PMSEs are, in addition, influenced by the presence of charged ice particles. The ice particles are spatially structured by the turbulence, and as the ice particles collect ambient electrons when they are charged, they cause electron gradients to last longer and to form on smaller scales. The neutral atmospheric motion and dissipation of gravity waves at these altitudes are causes for the turbulence. The radar echoes in PMSEs are stronger compared to normal incoherent scattering.

The EISCAT very high frequency (VHF) radar used in our study is designed to measure the incoherent scatter, which comes from the small-scale fluctuations in electrons in the ionospheric plasma. As the ionospheric electrons are exposed to the electromagnetic wave transmitted by the radar, the Thomson scattering scatters a small fraction back. The backscattered power is proportional to the electron density and the electron oscillations, which in turn are influenced by ion interactions. As a result, the spectra measured from incoherent scatter allow one to derive from the observed signal the electron density and electron and ion temperatures (Beynon and Williams, 1978). In their study, Rapp and Lübken (2004) elucidate the difference to PMSEs, where PMSEs are typically stronger than incoherent scatter located at the same altitude and their spectra are more narrow. Observations with radars that also detect incoherent scatter offer the opportunity to measure the electron density in the vicinity of the PMSEs.

Multilayered polar mesospheric summer echoes have been the focus of several investigations (Hoffmann et al., 2005; Li et al., 2016; Shucan et al., 2019). To simplify the exploration of PMSE multilayers, Jozwicki et al. (2021) conducted a study demonstrating the feasibility of distinguishing between images containing PMSEs and those that do not employing linear discriminant analysis (LDA). Subsequently, in Jozwicki et al. (2022), a model built on a random forest was employed to segment the PMSE signal from the incoherent scatter signal based on the power return in altitude. This model is utilized in the current paper for the pre-selection of data. An example of a PMSE occurrence with three distinct layers is depicted in Fig. 1 inside of the red frame. Given the significance of electron density in PMSE formation, it is reasonable to expect a potential influence of the solar cycle in it. Limited research has been conducted to examine the connection between multilayered PMSEs and the solar cycle.

We investigate PMSE observations with EISCAT VHF during the recent years. Our objective is to analyze the number of PMSE layers and their thickness, altitude and general behavior during the solar maximum and minimum and to determine possible correlations between these variables and the electron density at ionospheric heights above PMSEs. The study is organized as follows: in Sect. 2, we describe the methods and theories related to the pre-selection of the PMSE data, as well as the correlation coefficients employed to assess the significance of obtained results. In Sect. 3, we present and discuss the results. Finally, in Sect. 4, we summarize the conclusions drawn from this study.

2 Methods and theory

In this section, we describe our methodology for data selection, including the tools utilized. Furthermore, we present the criteria used for identifying the different PMSE layers and the metrics employed for analyzing the collected data. In this study, we use recorded data from the EISCAT VHF radar located in Tromsø that operates at 224 MHz. The geographical coordinates of the EISCAT VHF radar are 69°35′ N and 19°14′ E; its geomagnetic latitude and longitude are, respectively, 66.73 and 102.18°.

2.1 Data selection

The Grand Unified Incoherent Scatter Design and Analysis Package (GUISDAP) is a software package used for processing and analyzing data from the EISCAT VHF incoherent scatter radar (Lehtinen and Huuskonen, 1996). The GUISDAP analysis fits the observed frequency spectrum received from each height with an incoherent scatter profile. The analysis returns the electron density based on the backscattered power, independently from the scattering process. The electron density parameter given by the analysis is proportional to the received echo power and therefore the strength of the PMSEs.

We downloaded over 230 h of recorded data via the Madrigal website. This corresponds to 17 930 data points, with the details provided in Table 1. The EISCAT VHF radar utilizes many different experimental modes to collect data. The utilized pulse coding for the PMSE measurements we analyzed is referred to as “Manda”. Some parameters of the EISCAT VHF radar using the Manda experiment are listed in Table 2. Detailed information regarding this experiment can be found on the EISCAT website (https://eiscat.se/scientist/document/experiments/, last access: 1 January 2023). For this study, we specifically analyzed data obtained using the Manda experi-

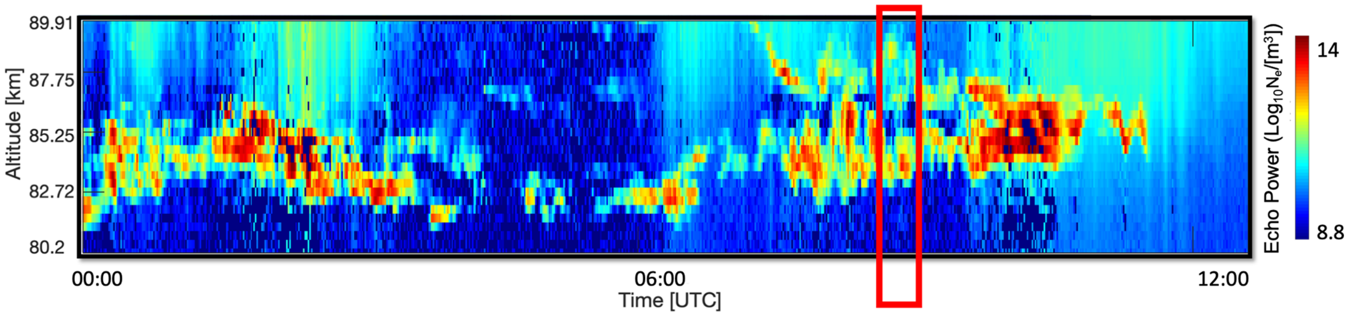

Figure 1. Data from EISCAT VHF from 16 July 2015 from 00:00 to 12:00 showing an example of a PMSE event that contains three multilayers in the red frame.

Table 1. The dataset used for this study. The upper part of the table displays the dates and times selected for the solar maximum, and the lower part of the table is dedicated to the solar minimum. For each date, the corresponding sunspot number and the F10.7 cm flux is displayed. The F10.7 cm solar flux is given in $\mathrm{W\,m^{-2}\,Hz^{-1}}$. The date and time format are given, respectively, in DD/MM/YYYY format and in hours and minutes.

	F10.7 cm flux	Sunspot number	Year	Date	Start time	End time	Observation hours per day	Observation hours per year	Observation hours per solar max or min	Total of observation hours
Solar maximum	9.95000E-21	90.9	2013	27/06/2013	07 h 02 min	10 h 58 min	03 h 56 min	57 h 52 min	130 h 18 min	230 h 32 min
	1.01000E-20	90.9		28/06/2013	07 h 02 min	12 h 58 min	05 h 56 min			
	1.19900E-20	94.6		09/07/2013	00 h 00 min	00 h 00 min	24 h 00 min			
	1.17900E-20	94.6		10/07/2013	00 h 00 min	00 h 00 min	24 h 00 min			
	9.91000E-21	112.6	2014	23/07/2014	00 h 00 min	09 h 26 min	09 h 26 min	09 h 26 min		
	1.01000E-20	68.3	2015	15/07/2015	08 h 00 min	00 h 00 min	16 h 00 min	63 h 00 min		
	9.96000E-21	68.3		16/07/2015	00 h 00 min	00 h 00 min	24 h 00 min			
	9.74000E-21	68.3		17/07/2015	00 h 00 min	23 h 00 min	23 h 00 min			
Solar minimum	6.70000E-21	3.7	2019	18/06/2019	06 h 59 min	00 h 00 min	17 h 00 min	59 h 13 min	100 h 14 min	
	6.80000E-21	3.7		19/06/2019	00 h 00 min	12 h 59 min	12 h 59 min			
	6.80000E-21	3.5		04/07/2019	07 h 07 min	12 h 21 min	05 h 14 min			
	6.70000E-21	3.4		20/08/2019	00 h 00 min	00 h 00 min	24 h 00 min			
	6.90000E-21	9.0	2020	06/07/2020	07 h 58 min	09 h 08 min	01 h 06 min	41 h 01 min		
	6.80000E-21	9.0		07/07/2020	00 h 00 min	11 h 59 min	11 h 59 min			
	6.70000E-21	9.0		08/07/2020	00 h 00 min	11 h 59 min	11 h 59 min			
	6.90000E-21	9.0		09/07/2020	00 h 00 min	11 h 58 min	11 h 58 min			
	6.90000E-21	9.0		10/07/2020	08 h 00 min	11 h 59 min	03 h 59 min			

ment because it is designed to detect low-altitude signals and layers in the mesosphere. We chose a time resolution of 60 s and a height resolution of 0.360 km.

We employed EISCAT VHF frequencies over UHF frequencies due to the latter exhibiting a lower recorded amount of PMSEs compared to VHF frequencies. As the Heating experiment is known to influence the backscattered power (also known as echo power) of the PMSEs (Belova et al., 2003), we carefully selected data from the days when the Heating experiment was not performed. This enabled us to compare electron densities at 92 km altitude alongside echo power at PMSE altitudes.

The data were carefully selected to encompass the solar maximum and solar minimum phases of the solar cycle. For the purpose of this study, we do not require an absolute value of PMSE strength; thus, we do not perform all the steps that would be necessary to obtain the absolute radar reflectivity as per the study by Hocking et al. (1986).

To investigate the behavior of the ionosphere in relation to PMSEs, we compared the echo power for PMSE altitudes between 80 and 90 km, with the electron density at 92 km ionospheric altitude. We used the electron density at 92 km altitude as a reference as it was the closest to the PMSE altitudes and the results were similar for altitudes of 92, 95 and 100 km.

2.2 Data processing

In this paper, we consider two variables: echo power and electron density. Both are measured in base-10 logarithmic units of the number of electrons per cubic meter. The number of electrons per cubic meter is proportional to the backscattered power for incoherent scatter, where the backscattered

Table 2. Some parameters of the EISCAT VHF radar, the source of data for this paper. More information about the EISCAT documentation and radar system parameters can be found at https://eiscat.se/scientist/document/experiments/, last access: 1 January 2023.

EISCAT VHF parameters	
Frequency	223.4 MHz
Wavelength	1.34 m
Bragg scale	0.67 m
Peak power	1.2 MW
Transmitted pulse scheme	Manda v 4.0
Interpulse period	1.5 ms
Time resolution	4.8 s
Range resolution	360 m
Spectral resolution	2.6 Hz
Antenna elevation	90°, zenith

power is defined as the amount of power in the scattered signal received by the antenna. We define the backscattered power at 92 km altitude as electron density. The backscattered power at PMSE altitudes, between 80 and 90 km altitude, is defined as echo power.

We selected the PMSE data between 80 and 90 km altitude using a segmentation model from the study by Jozwicki et al. (2022). The segmentation model used a random forest on a set of handcrafted features to segment the PMSE data from the background. Random forest is a machine learning algorithm used for both classification and regression. In this algorithm, a number of decision trees are used during training phase to make predictions. On the output from the segmentation model, we applied a threshold to ensure that only PMSE data were retained for further analysis. This thresholding technique was also employed in the study by Shucan et al. (2019), where they used an echo power threshold of $N_\mathrm{e} > 2.6 \times 10^{11}\,\mathrm{m}^{-3}$, and in the study by Rauf et al. (2018b), where the authors used a threshold $N_\mathrm{e} > 5.0 \times 10^{10}\,\mathrm{m}^{-3}$. We were able to use a lower threshold of $N_\mathrm{e} > 3.2 \times 10^{10}\,\mathrm{m}^{-3}$ (which is equivalent to 10.5 in base-10 logarithmic units of the number of electrons per cubic meter) as the segmentation model from the study by Jozwicki et al. (2022) had successfully removed almost all non-PMSE data. This enabled us to retain a large amount of PMSE data per number of hours of observation in comparison to the findings of Shucan et al. (2019) and Rauf et al. (2018b).

2.3 Detection of PMSE multilayers

After processing the data at PMSE altitudes as described in Sect. 2.2, we aimed to detect the start and end of each PMSE layer in altitude. To achieve this, we utilized a method used in the study by Hoffmann et al. (2005) and Shucan et al. (2019). This method involves defining the start of a layer each time the threshold for echo power is exceeded and the end of the layer when the echo power falls below the given threshold. The time intervals and the corresponding altitude intervals associated with the start and end of each layer were recorded. During solar maximum conditions, we observed a maximum of six layers. In this study, we decided to ignore multilayers with more than four layers as their occurrence rates were low. For instance, we observed 13 occurrences of five multilayers in the whole dataset and two occurrences of six multilayers. In Table 3, we show the occurrences of monolayer and multilayer PMSE events, observed during solar minimum and solar maximum phases, with each occurrence corresponding to a 1 min interval.

2.4 Data analysis

In this study, we perform comparisons between the different mono- and multilayers of PMSEs using a number of parameters. The parameters included the starting and ending altitude intervals of the layer, the layer thickness (calculated as the difference between the start and end altitude interval), the mean altitude interval that corresponds to the middle of the layer, the echo power in the mean altitude interval inside the PMSEs, the altitude of the mean altitude interval, the layer's time interval, the UTC time associated with the time interval, the number of layers present in the time interval, and the electron density at 92 km altitude.

In order to investigate different PMSE properties, we use the Pearson correlation coefficient and the Spearman rank correlation coefficient to calculate the correlations between the different parameters (Wilks, 1995; Myers and Well, 2003). The Pearson correlation coefficient is used to measure how strong and in what direction two variables are related in a linear way (Wilks, 1995). For two random variables X and Y, the Pearson correlation coefficient is defined as follows (Wilks, 1995):

$$r_\mathrm{Pearson}(X,Y) = \frac{\mathrm{cov}(X,Y)}{\sigma_X \sigma_Y}, \tag{1}$$

where σ_X and σ_Y are the respective standard deviations of X and Y and cov is the covariance.

The Spearman rank correlation coefficient is a measure of the strength and direction of the relationship between two variables. It is similar to the Pearson correlation, but instead of measuring the linear relationship between two variables, it measures the monotonic relationship between them. The Spearman rank correlation coefficient is obtained by calculating the Pearson correlation between the ranked values of the variables (Myers and Well, 2003). To compute the Spearman correlation coefficient, for a sample size n, the raw scores X_i and Y_i are converted into their rank values, rg_X and rg_Y. After that, the Spearman correlation coefficient is computed as follows:

$$r_\mathrm{Spearman} = \frac{\mathrm{cov}\,(rg_X, rg_Y)}{\sigma_{rg_X} \sigma_{rg_Y}}, \tag{2}$$

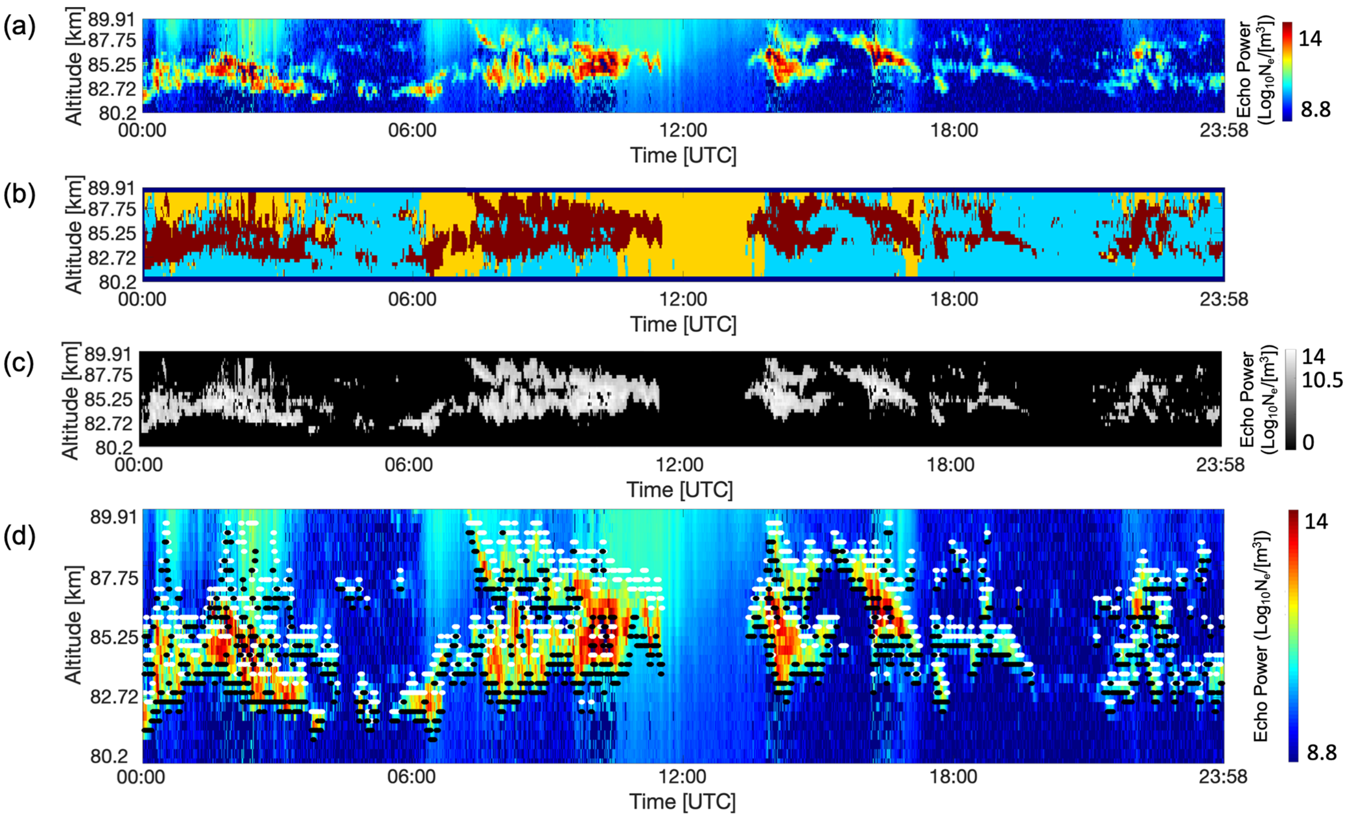

Figure 2. Figure illustrating the process of the layer detection. **(a)** The original data for the 16 July 2015 between 00:00 and 23:58. **(b)** The output from the classification model used from Jozwicki et al. (2022). Dark red represents areas labeled as PMSEs, cyan represents areas of the data labeled as background noise and yellow represents areas labeled as ionospheric background. Panel **(c)** represents the data labeled as PMSEs in dark red from sub **(b)** onto which we applied the threshold described in Sect. 2.2 to make sure we only have PMSE data left. Finally, panel **(d)** represents the detected beginning and end of layers, respectively, represented with white and black points and overlayed on the original data.

where σ_{rg_X} and σ_{rg_Y} are the standard deviations of the rank variables, and $\mathrm{cov}(rg_X, rg_Y)$ is the covariance of those rank variables.

In this analysis, we calculated the statistical significance of our results using the P value (t test), which is listed in Tables B2, B3 and B4 in the Appendix. P values are used to determine whether the obtained results are different enough to be judged as statistically significant or not, using the means, variances and populations of the given variables. If the P value falls below the significance level (alpha), the given result is considered to be statistically significant. Testing the statistical significance of results comes with various confidence levels (90 %, 95 % and 99 %), which depend on the chosen significance level (with corresponding significance levels of 0.1, 0.05 and 0.01). It is commonly accepted that a P value below $\alpha = 0.05$ is indicative of statistical significance. However, in this study, we are analyzing a multiparameter dataset, which is why we chose a lower threshold of $\alpha = 0.0001$ that is 2 orders of magnitude more selective.

3 Results and discussion

In this section, we discuss our results, which are organized into multiple parts. Firstly, we discuss the distributions of a few variables, which are presented using histograms. Subsequently, we analyze the correlation coefficients that we have computed for the different variables.

3.1 Height distribution of PMSE layers

Our study focuses on observations from the summer mesopause during the solar maximum in years 2013 to 2015 and the solar minimum in years 2020 and 2021. The average peak altitude of PMSE height distribution, considering all PMSE detections, is higher during the solar maximum than during the solar minimum (see Fig. 3). The averaged mean altitude values of all the separate layers in the different sets of two multilayers, three multilayers and four multilayers are shown in the Appendix in Figs. A1 and A2.

When considering the mean altitude values of individual layers within the sets of two, three and four multilayers, a

Table 3. The number of occurrences and approximate percentage of occurrence for each of the mono- and multilayers in our dataset. The data are separated according to solar maximum and solar minimum. For both solar maximum and solar minimum, the approximate percentage of occurrence for five multilayers or more is below 1,%. Therefore, the analysis in this study is limited to PMSEs with up to four multilayers.

		Number of occurrences	Total number of occurrences per solar max or min	Approximate percentage of Occurrence
Solar maximum	Monolayers	3077	5996	51
	Two multilayers	2233		37
	Three multilayers	597		10
	Four multilayers	81		1
	Five multilayers	6		< 1
	Six multilayers	2		< 1
	Seven multilayers	0		0
Solar minimum	Monolayers	1399	2736	51
	Two multilayers	935		34
	Three multilayers	328		12
	Four multilayers	67		2
	Five multilayers	7		< 1
	Six multilayers	0		0
	Seven multilayers	0		0

trend is seen in Figs. 4 and 5. In these figures, the color scheme has the red distribution representing the highest-altitude layer (the topmost layer) followed by the green distribution for the second-highest layer, the blue distribution for the third-highest layer and the magenta distribution for the fourth-highest layer. Additionally, when two layers' altitude distributions overlap, an intermediate color arises to represent this overlap. The P values for all possible combinations of these individual layers, as shown in Figs. 4 and 5, can be found in Table B1 in the Appendix. Upon decomposing the multilayer sets into individual layers, one can see that in both solar maximum and solar minimum conditions, the altitude of the top layer increases as the number of multilayers increases. This pattern holds true for the second- and third-highest layers as well.

Our study confirms the findings of Hoffmann et al. (2005) regarding the altitude of the observed mono and multiple layers. Hoffmann et al. (2005) examined the occurrence and mean altitude of PMSE layers and performed microphysical model simulations. They proposed that the observed multiple-PMSE-layer structures are mainly caused by the layering of ice particles due to subsequent nucleation cycles. They reported that monolayers occurred at an average altitude of 84.8 km, and our results show that the mean altitude of monolayers was 85.21 km for the solar maximum and 84.46 km for the solar minimum. Our mean altitude of 84.83 km is consistent with the results of Hoffmann et al. (2005). Furthermore, they observed that in a set of two multilayers, the lower layer occurs at a mean altitude of 83.4 km and the upper layer occurs at a mean height of about 86.3 km, which is consistent with our findings. In fact, we found that in a set of two multilayers, the lower layer happens at a mean altitude of 83.74 km for the solar maximum and 82.90 km for the solar minimum, which results in an average of 83.32 km. Additionally, the upper layer occurs at an average altitude of 86.71 km for the solar maximum and 85.97 km for the solar minimum, which results in an average altitude of 86.34 km over the whole solar cycle. For this reason, we can note a similar observation to that in the study of Hoffmann et al. (2005) which claims that the altitude of the lower layer is in good agreement with the mean altitude of NLCs from lidar observations made by Fiedler et al. (2003) at Arctic Lidar Observatory for Middle Atmosphere Research (ALOMAR; at 69°16′42.0″ N, 16°00′29.0″ E, i.e., close to EISCAT), where the mean altitude of NLCs was found to be about 83.3 km. When examining the lowest layer in various multilayer sets in Figs. 4 and 5 (not limited to a set of just two multilayers, as discussed earlier), one can notice that the lowest layer almost always aligns with the NLC altitude as reported by Fiedler et al. (2003). Finally, Hoffmann et al. (2005) observed that monolayers occurred 50.1 %, double layers 36.6 % and multilayers with more than two layers 13.3 % of the time, during both solar maximum and minimum periods. Our study indicates that monolayers were observed at a rate of 51 % in both solar maximum and minimum, while double layers occurred at a rate of 37 % in solar maximum and 34 % in solar minimum. Furthermore, we found that the occurrence rate for multilayers with three and four layers combined was more than 11 % in the solar maximum and more than 14 % in the solar minimum.

The solar maximum phase is characterized by an increased number of sunspots and higher levels of ultraviolet radiation compared to the solar minimum phase. The F10.7 flux is often used as a proxy for the level of solar activity and,

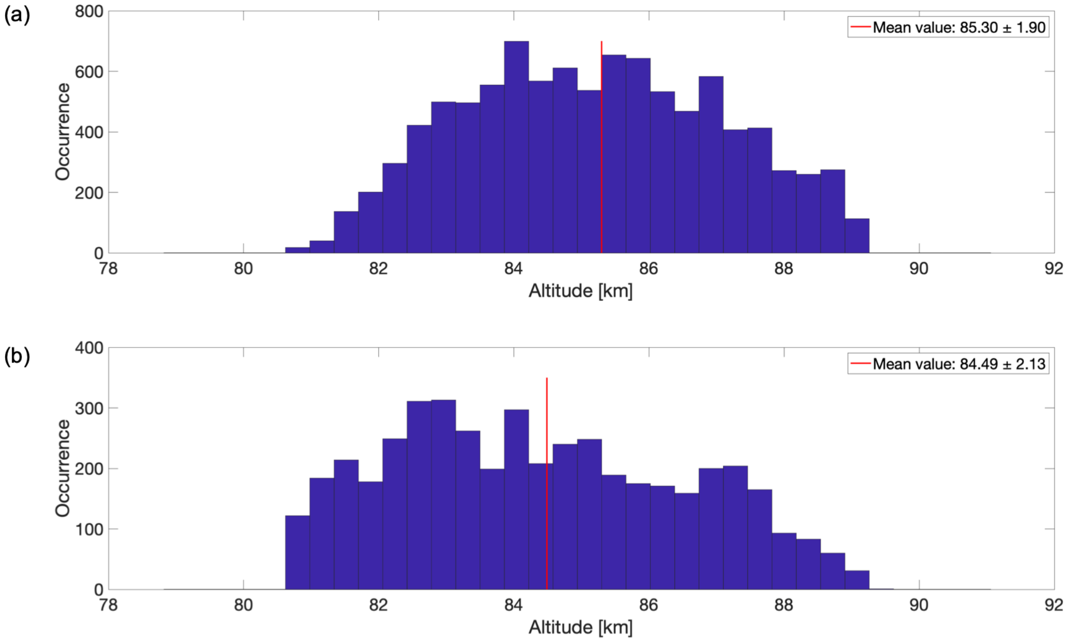

Figure 3. Altitude distribution of the data for the **(a)** solar maximum and **(b)** solar minimum. Each subplot has its respective mean altitude represented with a red line on the graph and specified in the legend together with 1 standard deviation.

more specifically, the amount of ultraviolet radiation. The K index describes geomagnetic activity and potentially corresponds to particle precipitation. Shucan et al. (2019) found that PMSE mono-, double-, and triple-layer occurrence ratios are positively correlated with the K index. Also, Shucan et al. (2019) mention that the PMSE triple-layer occurrence ratio shows a negative correlation with F10.7. Zhao et al. (2020) reported a positive correlation between the temperature of the mesopause and the F10.7 flux. They found that the temperature of the mesopause is decreasing with time over an 18-year-long investigation (from 0 to $-0.14\,\mathrm{K\,yr^{-1}}$), which could affect the formation of PMSEs. They also found that the height of the mesopause is decreasing with time at polar latitudes, which could potentially impact the height of PMSEs.

Lübken et al. (2021) show in their study that, over time, the ice particles are increasing in size. In Fig. 3, we can see that the altitude of the PMSE layers is, on average, lower for the solar minimum compared to the solar maximum. This could be due to the fact that the ice particle sizes increase with time over the years, and our selected dates for the solar maximum are anterior to the selected dates for the solar minimum. Considering these findings, the small difference in the altitude of the layers that we noted may be due to trends not related to solar cycle effects. Therefore, it appears that factors other than the sole influence from the solar cycle play a significant role in the altitude of PMSEs. Finally, further investigations and comparing the next solar maximum to the previous one might bring more clarity to the understanding of the influence from the solar cycle alone.

3.2 Distribution of the electron density

In the next step, we investigate how the distribution of the PMSE layers changes with ionization. We consider the electron densities observed above the PMSEs and ignore specific causes of ionization in this study. All the observed electron densities are summarized in Fig. 6; they range from 8.9 to 11.7 electrons per cubic meter in base-10 logarithmic unit during the solar maximum and their mean value is slightly higher during the solar maximum. Specifically, multilayer PMSEs with two layers exhibit the highest average corresponding electron density, reaching 10.47 electrons per cubic meter in base-10 logarithmic unit as one can see from Fig. 7. In contrast, the monolayers during the solar minimum have the lowest average corresponding electron density, with a value of 10.15 electrons per cubic meter in base-10 logarithmic unit, as displayed in Fig. 8. It is worth noting that, for both solar maximum and solar minimum periods, the monolayers corresponded to the lowest average electron density of their respective seasons. However, it is important to bear in mind that this trend is weak and that some P values corresponding to the different combinations of layers in Figs. 7 and 8 are greater than 0.05, as shown in Table B2. A plausible argument could be made that higher electron densities at ionospheric altitudes might be necessary to observe multilayered PMSEs.

During the solar maximum, we observe a wider range of electron densities compared to the solar minimum when PMSEs are present, particularly at higher electron densities. This variation in electron densities may explain why

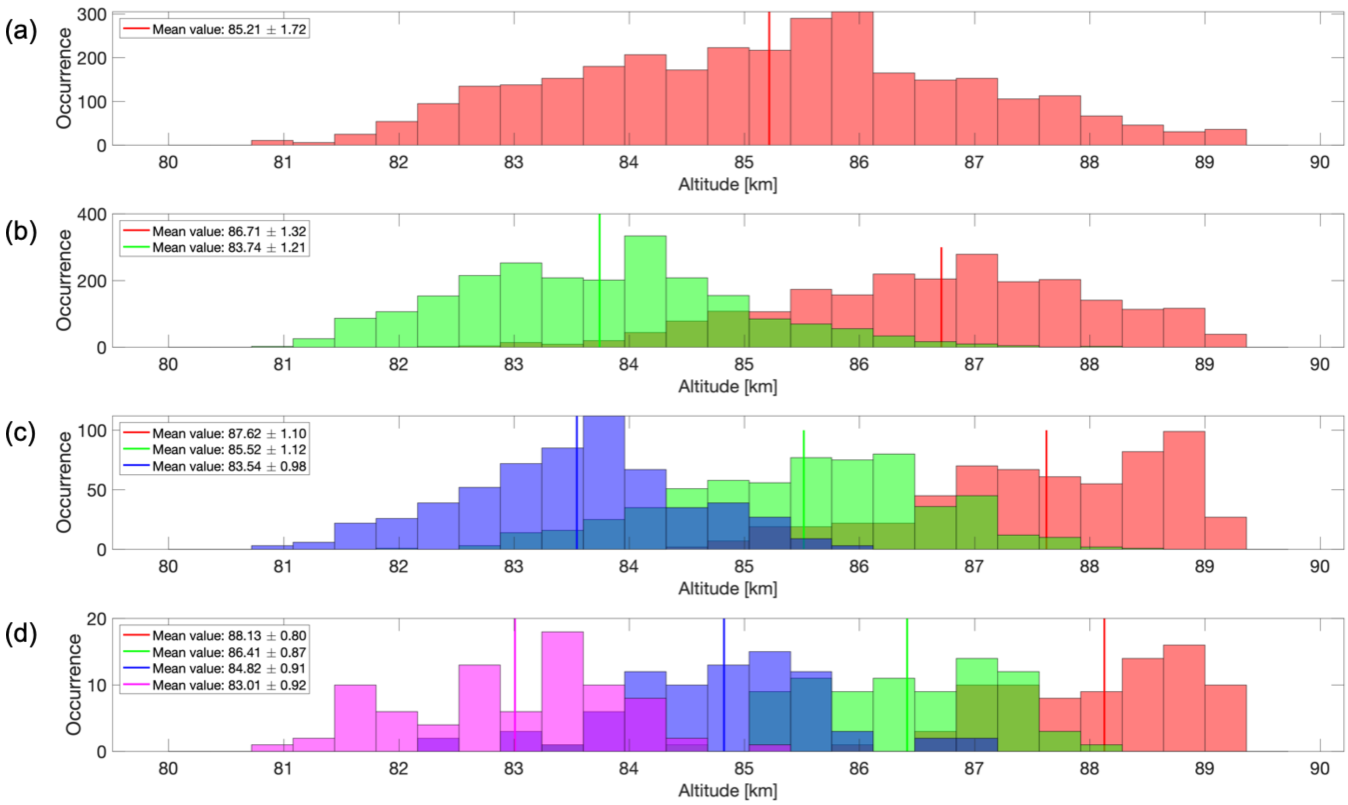

Figure 4. Altitude distribution of the data during the solar maximum for **(a)** monolayers, **(b)** multilayers with two layers, **(c)** multilayers with three layers and **(d)** multilayers with four layers. In each figure, the color scheme of the distributions indicates altitude order: red for the highest layer, green for the second-highest, blue for the third-highest and magenta for the fourth-highest. Intermediate colors represent overlapping altitude distributions. The legend displays the mean value and 1 standard deviation for each distribution.

the mean electron density at an altitude of 92 km is higher during the solar maximum than the solar minimum during PMSE events. Additionally, our analysis reveals that the standard deviation of electron densities decreases with increasing number of layers, with monolayers exhibiting the largest standard deviations and four-layer systems exhibiting the smallest standard deviations for both solar maximum and minimum conditions.

3.3 Distribution of the echo power

As discussed in Sect. 2.2, we classified the data using the classification model of Jozwicki et al. (2022) and applied a threshold to identify PMSEs. Specifically, we considered all echo power values above a threshold of 10.5 electrons per cubic meter in base-10 logarithmic unit as PMSEs. This explains the absence of values below 10.5 on the horizontal axis of Figs. 9, 10 and 11. Figures have been generated to visualize individual layers within the various sets of two, three and four multilayers seen in Figs. 10 and 11. This approach mirrors the technique employed in Figs. 4 and 5. However, since the separation of layers did not yield additional information, we have chosen to retain the averaged representations of all multilayers combined, as depicted in Figs. 10 and 11.

In Fig. 9, it is evident that the average echo power in PMSEs is higher during the solar maximum than the solar minimum. We noticed a greater distribution of higher values of echo power during the solar maximum as compared to the solar minimum, which leads to a higher mean value during the solar maximum. Further, in Fig. 10, we observe that the average echo power decreases as the number of multilayers increases for the solar maximum and the individual layers are considered. This indicates that a single monolayer has a higher echo power than the individual layers of two multilayers, which in turn have a higher echo power than the individual layers of three multilayers and so on. However, during the solar minimum, as shown in Fig. 11, this trend is less evident, and we do not see a clear decrease in echo power with the increasing number of layers.

3.4 Distribution of the thickness

In our study, we determined the thickness of the PMSE layers based on the number of neighboring data points or altitude channels exceeding the echo power threshold described in

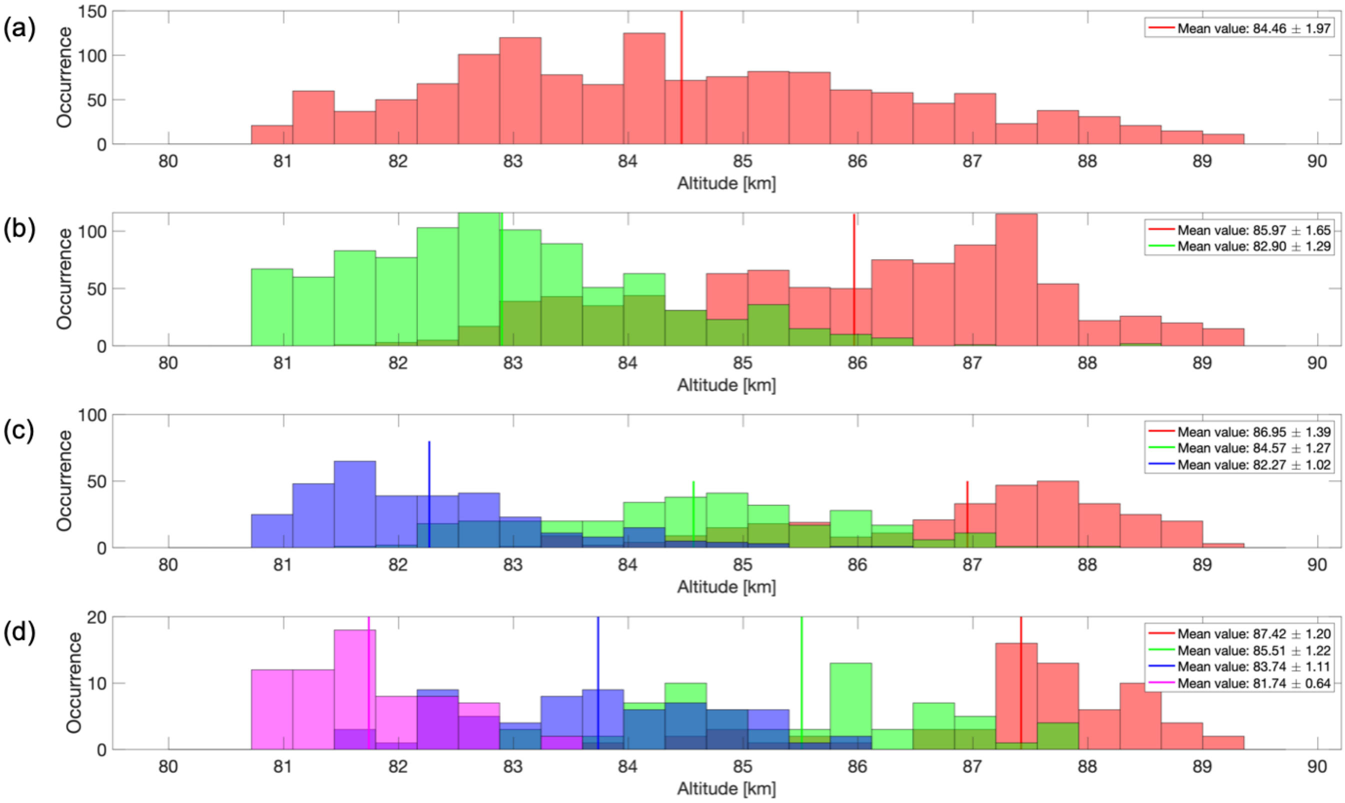

Figure 5. Altitude distribution of the data during the solar minimum for **(a)** monolayers, **(b)** multilayers with two layers, **(c)** multilayers with three layers and **(d)** multilayers with four layers. In each figure, the color scheme of the distributions indicates altitude order: red for the highest layer, green for the second-highest, blue for the third-highest and magenta for the fourth-highest. Intermediate colors represent overlapping altitude distributions. The legend displays the mean value and 1 standard deviation for each distribution.

Sect. 2.2. Each data point or altitude channel corresponds to a distance of 360 m. As shown in Fig. 12, the average thickness of the layers is higher during the solar maximum, with an average of 1.59 km, compared to solar minimum, where the average thickness is 1.32 km. When we examine the mono- and multilayer cases in more detail, as shown in Figs. 13 and 14, we observe that the average thickness decreases as the number of layers increases. This means that a monolayer will be thicker than a layer belonging to a set of two multilayers, which in turn will be thicker than a layer in a three-multilayer case and so on. Figures have been generated to visualize individual layers within the various sets of two, three and four multilayers seen in Figs. 13 and 14. This approach mirrors the technique employed in Figs. 4 and 5. However, since the separation of layers did not yield additional information, we have chosen to retain the averaged representations of all multilayers combined, as depicted in Figs. 13 and 14. The highest average layer thickness is obtained during the solar maximum for monolayers, with an average of 2.15 km, while the lowest average of 0.87 km is obtained during the solar minimum for four multilayers.

A comparison can be drawn between the thickness of NLCs and PMSEs. Although the formation mechanisms of these two phenomena differ, there is a shared population of ice particles that contribute to both. Therefore, it is worthwhile to explore the potential similarities and differences between them. Lübken et al. (2009) found that NLCs have a higher brightness at lower altitudes, while Schäfer et al. (2020) analyzed 182 h of lidar data and found that NLCs occur more than half of the time (57.2 %) in thick layers of more than 1 km. In our study, we analyzed 7790 instances of PMSEs with three or more altitude channels. Knowing that one altitude channel corresponds to 360 m, three altitude channels or more indicate a PMSE thickness of at least 1.08 km. Our findings show that 54.64 % of PMSE occurrences happened in thick layers of 1.08 km or more. These results are consistent with those of Schäfer et al. (2020), where they reported that 57.2 % of NLC occurrences were observed in thick layers of 1 km or more. Additionally, Schäfer et al. (2020) classified the NLCs they observed into 10 subcategories and found that the most frequently occurring subcategory consists of thick layers composed of multiple multilayers, with an occurrence rate of 20.5 %. They report that each of the multilayers move in parallel with each other. This implies that there is a similar movement in the vertical displacement of the multilayers. If we consider all types of multilay-

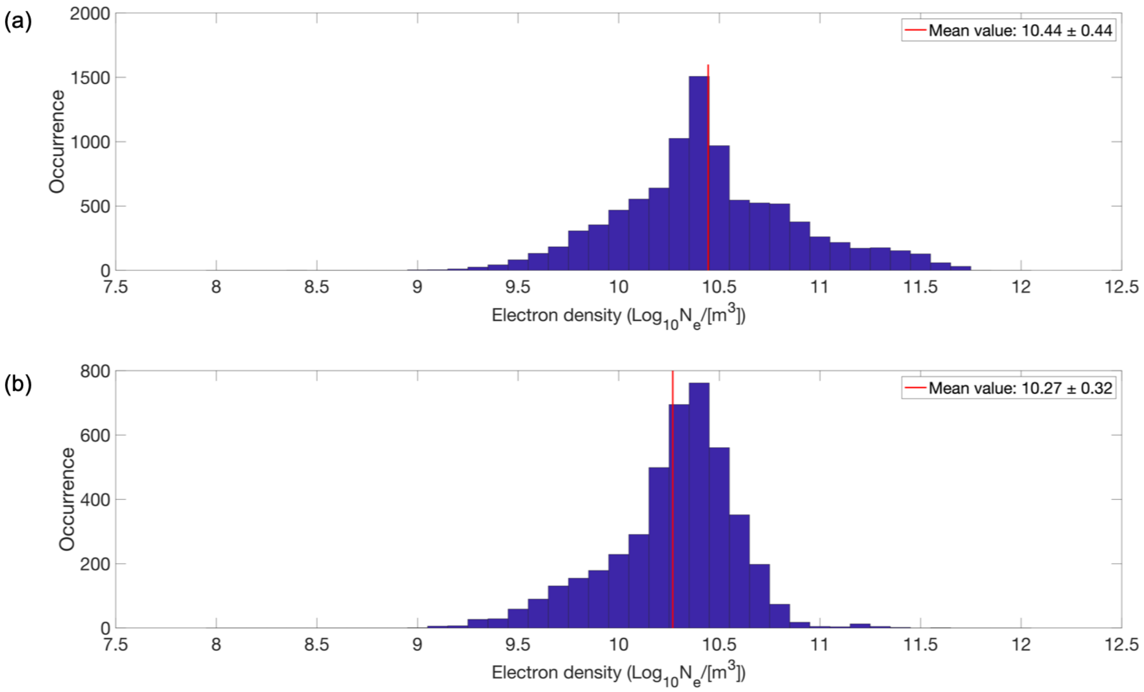

Figure 6. Electron densities at 92 km altitude for all layers during the **(a)** solar maximum and **(b)** solar minimum. Each subplot was its respective mean electron density represented with a red line on the graph and specified in the legend together with 1 standard deviation.

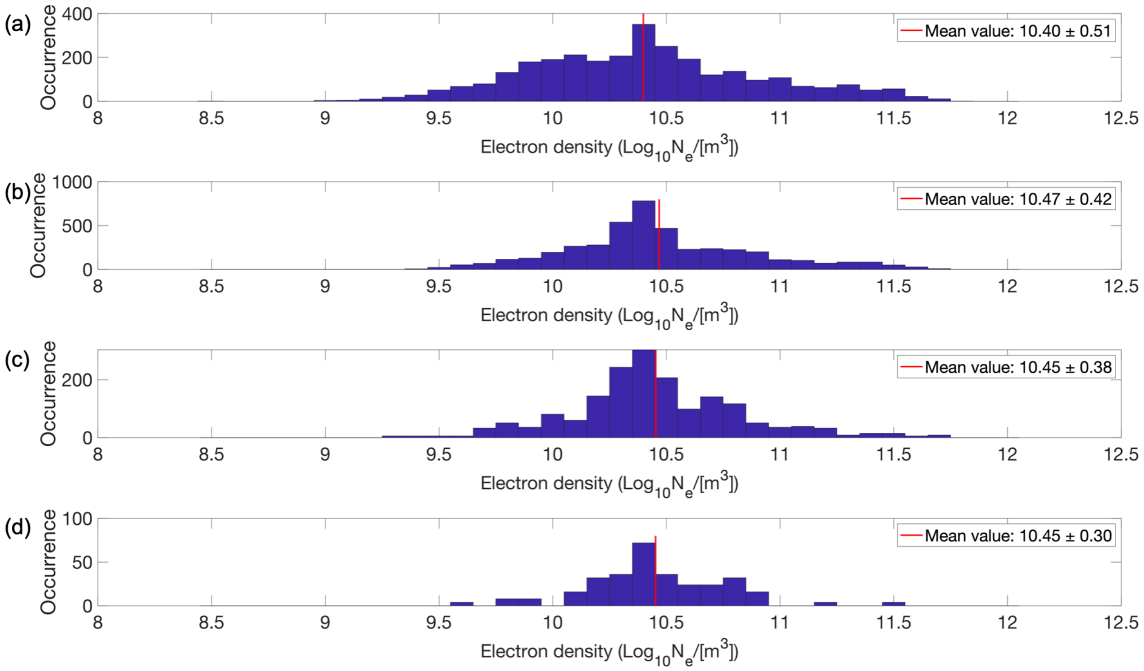

Figure 7. Electron density at 92 km altitude during the solar maximum for **(a)** monolayers, **(b)** multilayers with two layers, **(c)** multilayers with three layers and **(d)** multilayers with four layers. Each subplot was its respective mean electron density represented with a red line on the graph and specified in the legend together with 1 standard deviation.

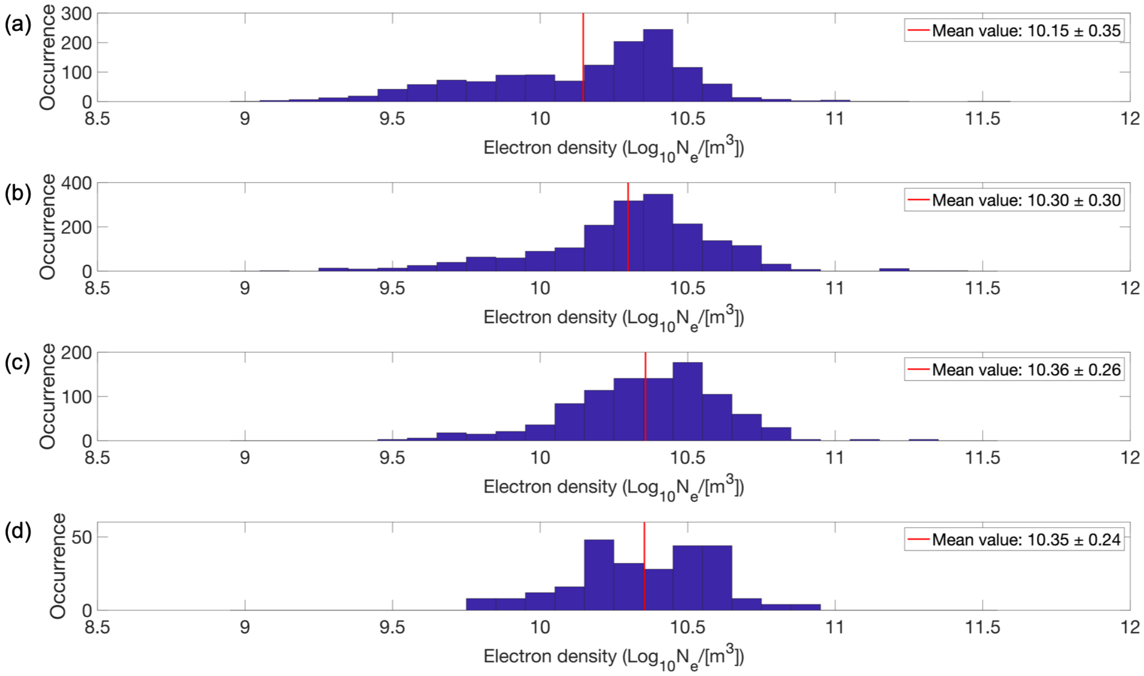

Figure 8. Electron density at 92 km altitude during the solar minimum for **(a)** monolayers, **(b)** multilayers with two layers, **(c)** multilayers with three layers and **(d)** multilayers with four layers. Each subplot was its respective mean electron density represented with a red line on the graph and specified in the legend together with 1 standard deviation.

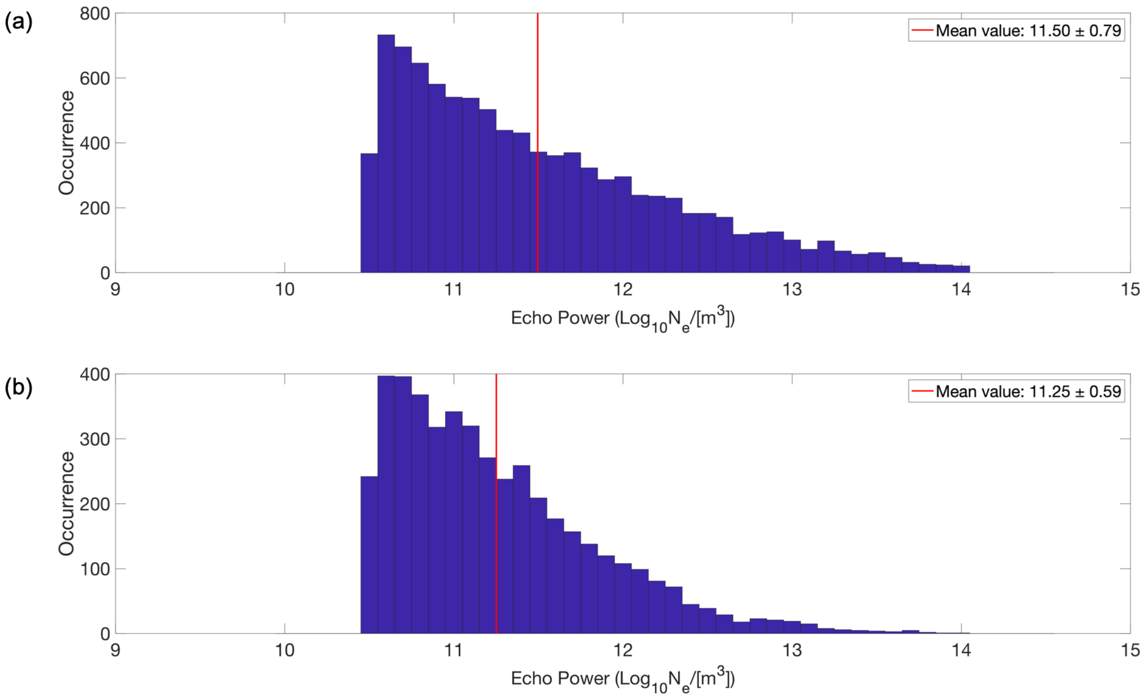

Figure 9. Echo power in the PMSEs for all layers during the **(a)** solar maximum and **(b)** solar minimum. Each subplot has its respective mean echo power represented with a red line on the graph and specified in the legend together with 1 standard deviation.

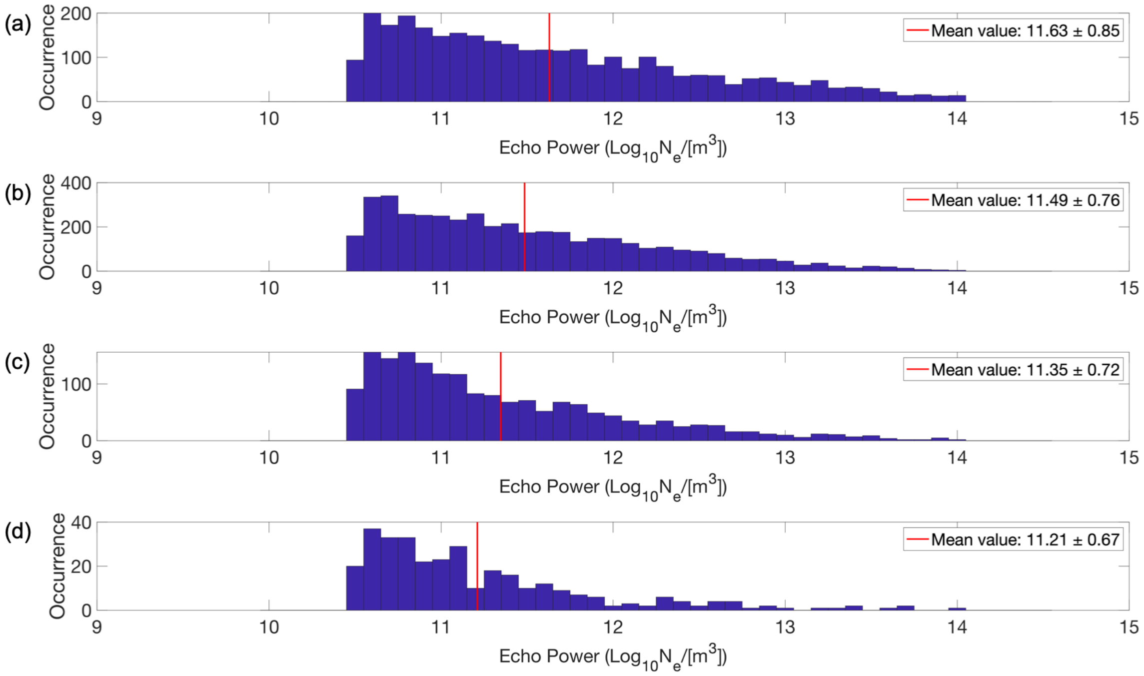

Figure 10. Echo power in the PMSEs during the solar maximum for **(a)** monolayers, **(b)** multilayers with two layers, **(c)** multilayers with three layers and **(d)** multilayers with four layers. Each subplot has its respective mean echo power represented with a red line on the graph and specified in the legend together with 1 standard deviation.

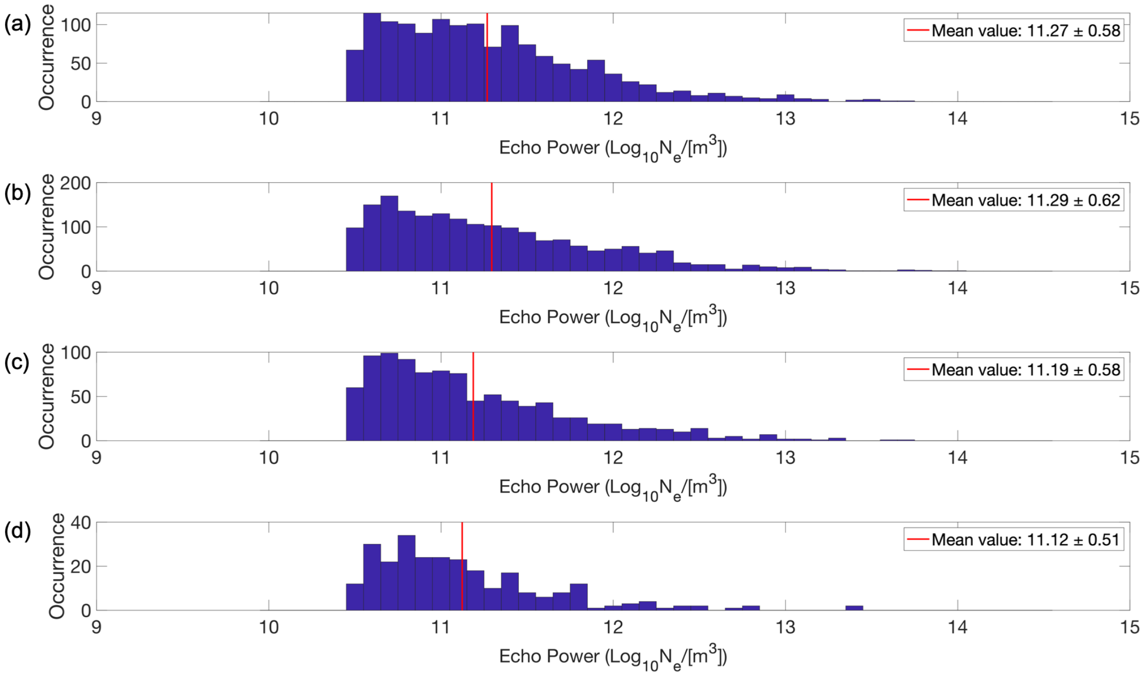

Figure 11. Echo power in the PMSEs during the solar minimum for **(a)** monolayers, **(b)** multilayers with two layers, **(c)** multilayers with three layers and **(d)** multilayers with four layers. Each subplot has its respective mean echo power represented with a red line on the graph and specified in the legend together with 1 standard deviation.

ers mentioned by Schäfer et al. (2020), this percentage increases to up to 27.6 %. In our study, multilayers happen half of the time, with an approximate occurrence rate of 49 %. Therefore, our results differ from the ones of Schäfer et al. (2020) when it comes to the occurrence rate of multilayers, which may be explained by some of the differences in the formation and measurement of the two phenomena.

Gravity waves are thought to play a role in the formation of PMSEs by generating neutral turbulence in the mesosphere. The complex dynamics and structuring because of shear instabilities and breaking of the gravity waves are derived, for example, from polar mesospheric cloud observations and can generate turbulence at PMSE altitudes (Fritts et al., 2019). This turbulence can lead to small-scale variations in the electron density, which can create the conditions necessary for PMSEs to form (Rapp and Lübken, 2004). Therefore, understanding the characteristics of gravity waves and their effects on the neutral atmosphere is essential for understanding the formation of PMSEs.

Li et al. (2016) developed a two-dimensional theoretical model to explore the creation process of multilayered PMSEs. The aim of the proposed model was to consider how gravity waves could cause movement of ice particles through collisions with the neutral atmosphere. Their model was able to simulate the presence of gravity waves by assigning both vertical and horizontal wavelengths. The ice particles are considered to be spherical, and their size does not vary during the simulations. This means that processes such as growth, sedimentation or sublimation are not taken into account in their model. In their first experiment, Li et al. (2016) fixed the particle size at 10 nm and varied the vertical wavelength of gravity waves to 3, 4 and 5 km. Only one wavelength was considered at a time, when varying the vertical wavelength. They observed a decrease in the number of layers as the vertical wavelength increased. Also, the thickness of the layers increased as the number of layers decreased. Our results on thickness distribution shown in Figs. 12, 13 and 14 show similar trends. We found that the average thickness of monolayers was higher than that of multilayers and that the thickness decreased with an increasing number of multilayers. One possible hypothesis that can be drawn is that the thickness of the layers could be related to the vertical wavelength of gravity waves, with higher wavelengths producing thicker layers.

In another experiment in the Li et al. (2016) study, they investigated the effect of varying ice particle size while fixing the vertical wavelength of gravity waves at 4km. They used particle sizes of 10, 20 and 30 nm and found that the altitude of the layers decreased more rapidly and their formation became more challenging with increasing particle size. Also, once the turbulence stopped, the larger ice particles took longer to go back to a neutral homogeneous state. It is worth noting that their model does not consider the growth, sedimentation and sublimation processes, so these findings should be considered preliminary hypotheses. Li et al. (2016) also reported the observation of preferred altitudes for each multilayer formation, which depended on the size of the ice particles. Potential mechanisms for ice formation at upper mesospheric altitudes that could be affected by the solar cycle are unknown to the authors, but this is something to investigate in a future study.

Neutral air turbulence, which is a key factor in PMSE formation, can be generated by wind shears. Singer et al. (2012) found that westward winds increase below an altitude of about 85 km, while eastward winds increase above 85 km, particularly during summer. They also found that at an altitude of about 75 km, the long-term trend of zonal winds corresponds to increased activity of gravity waves with periods of 3 to 6 h at altitudes between 80 and 88 km. Severe solar proton events cause eastward winds to increase above an altitude of about 85 km. This behavior of winds and their effects at PMSE altitudes may be another key to a better understanding of the formation of multilayered PMSEs.

3.5 Correlations

In this section, we will analyze the correlation between several parameters – namely, electron density, echo power, thickness and altitude. Table 4 shows both correlation coefficients for all layers together for the solar maximum on the lower portion of the table and for the solar minimum on the upper portion of the table. Table 5a shows the results of the Pearson correlation coefficient only, for mono- and multilayers separately, and for the solar maximum and minimum. Table 5b shows the results of the Spearman rank correlation coefficient only, for mono- and multilayers separately, and for the solar maximum and minimum. For simplicity, in all the abovementioned tables, the notation r_p is chosen to represent Pearson correlation coefficients, and the notation r_s is chosen to represent Spearman rank correlation coefficients. In Table 5a and b, the notations r_p1, r_p2, r_p3 and r_p4 denote the Pearson correlation coefficients for monolayers, double layers, triple layers and quadruple layers, respectively. In a similar manner, the Spearman rank correlation coefficient notations are r_s1, r_s2, r_s3 and r_s4.

In Table 4, it is observed that the electron density at 92 km altitude and the echo power are positively correlated with the thickness of all the layers for both the solar maximum and solar minimum. This is also the case for Table 5a and b. During the solar maximum, the positive correlation between electron density and thickness is greater than during the solar minimum, but this is not observed between echo power and thickness. In Table 4, the Pearson correlation coefficient of 0.480 for the solar maximum suggests a moderate positive linear relationship between electron density and thickness, while the Spearman rank correlation coefficient of 0.392 indicates a moderate positive monotonic relationship between the variables for the same case. Since the two values are similar, it suggests that during the solar maximum, there is a consistent association between electron density and

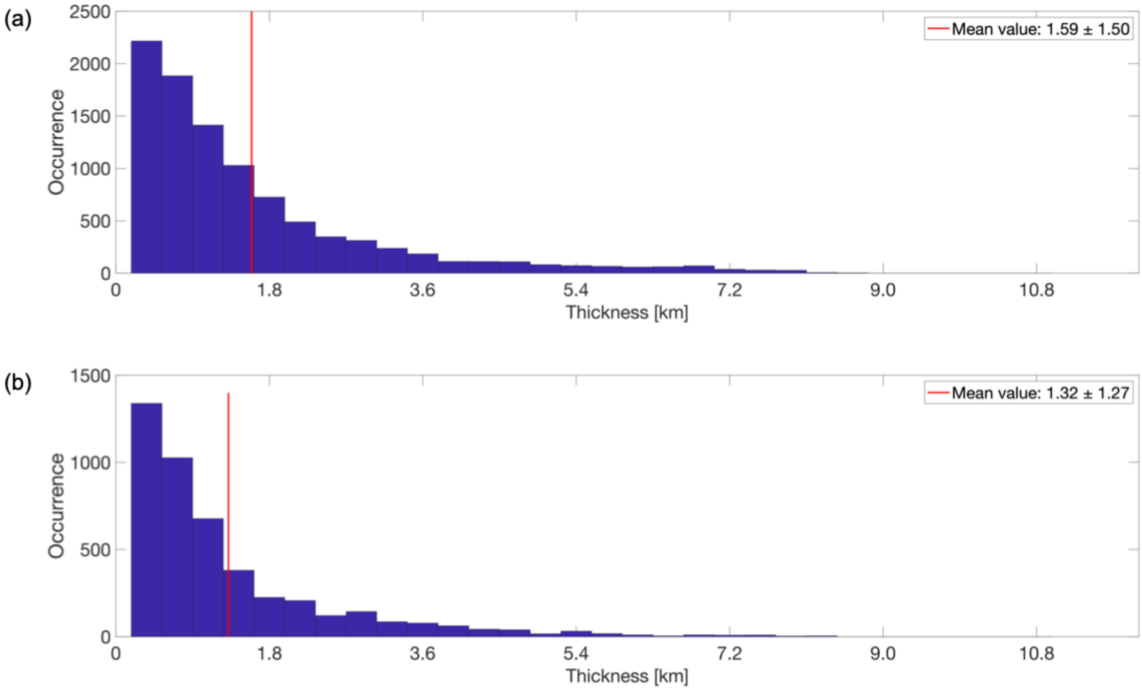

Figure 12. Thickness distribution of the layers for all layers combined during the **(a)** solar maximum and **(b)** solar minimum. Each subplot was its respective mean thickness represented with a red line on the graph and specified in the legend together with 1 standard deviation.

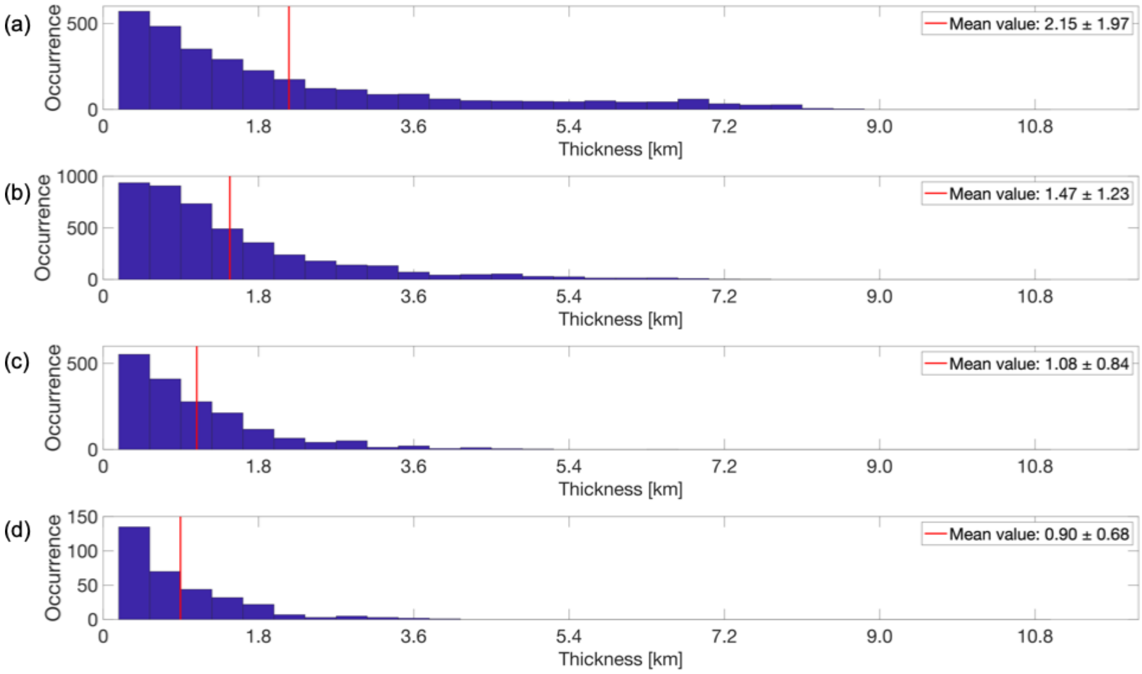

Figure 13. Thickness distribution during the solar maximum for **(a)** monolayers, **(b)** multilayers with two layers, **(c)** multilayers with three layers and **(d)** multilayers with four layers. Each subplot was its respective mean thickness represented with a red line on the graph and specified in the legend together with 1 standard deviation.

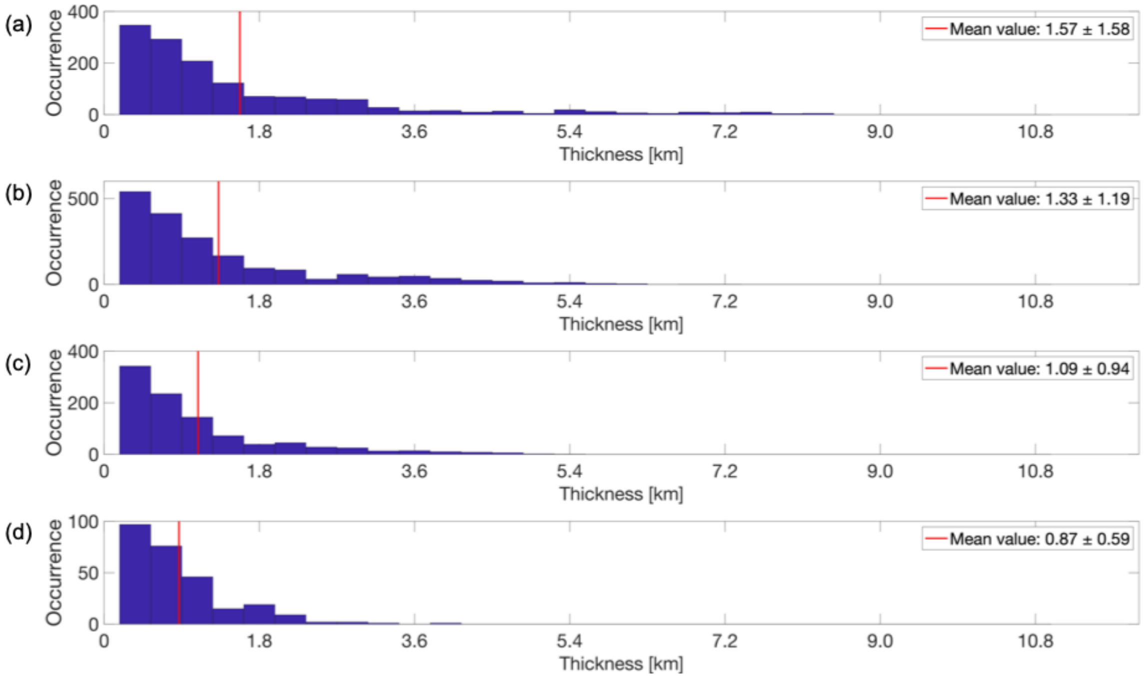

Figure 14. Thickness distribution during the solar minimum for **(a)** monolayers, **(b)** multilayers with two layers, **(c)** multilayers with three layers and **(d)** multilayers with four layers. Each subplot was its respective mean thickness represented with a red line on the graph and specified in the legend together with 1 standard deviation.

Table 4. Pearson and Spearman rank correlation coefficients for all layers together for the solar maximum and solar minimum.

		Solar minimum			
		Electron density	Echo power	Thickness	Altitude
Solar maximum	Electron density		$r_p = 0.213$ $r_s = 0.163$	$r_p = 0.251$ $r_s = 0.232$	$r_p = -0.079$ $r_s = -0.058$
	Echo power	$r_p = 0.338$ $r_s = 0.305$		$r_p = 0.521$ $r_s = 0.631$	$r_p = -0.165$ $r_s = -0.162$
	Thickness	$r_p = 0.480$ $r_s = 0.392$	$r_p = 0.510$ $r_s = 0.631$		$r_p = -0.153$ $r_s = -0.169$
	Altitude	$r_p = 0.011$ $r_s = 0.003$	$r_p = -0.034$ $r_s = -0.031$	$r_p = 0.039$ $r_s = 0.024$	

thickness. In Table 5a and b, we observe that the Pearson correlation coefficient and Spearman rank correlation coefficient between electron density and thickness decrease as the number of multilayers increases. Specifically, in both cases the highest correlation is observed for the solar maximum and monolayers, with a Pearson coefficient of 0.695 and a Spearman rank coefficient of 0.668. This could possibly indicate that at higher ionization levels at this altitude, the PMSE monolayers are thicker. Conversely, the lowest correlations were obtained for the solar minimum and the largest number of multilayers, which is 4, with a Pearson coefficient of 0.168 and a Spearman rank coefficient of 0.173.

From Tables 4, 5a, and b we notice a weak negative correlation between the echo power in the PMSEs and altitude for all layers during both solar maximum and solar minimum. The strongest negative correlation is found for 3 multilayers, with a Pearson coefficient of −0.228 and a Spearman rank coefficient of −0.240. Notably, altitude appears to be uncorrelated with the other variables, implying that additional factors may be influencing the formation of PMSEs at specific altitudes. For example, this could be attributed to mesopause conditions, gravity wave wavelength and ice particle size.

From Tables 4, 5a, and b electron density at 92 km altitude and the echo power in the PMSEs for all the layers and for both solar maximum and solar minimum. For Table 5a and

Table 5. **(a)** Pearson correlation coefficients for mono- and multilayers separately for the solar maximum and solar minimum. **(b)** Spearman rank correlation coefficients for mono- and multilayers separately for the solar maximum and solar minimum.

(a)		Solar minimum			
		Electron density	Echo power	Thickness	Altitude
Solar maximum	Electron density		$r_{p1} = 0.270$ $r_{p2} = 0.247$ $r_{p3} = 0.163$ $r_{p4} = 0.199$	$r_{p1} = 0.376$ $r_{p2} = 0.273$ $r_{p3} = 0.226$ $r_{p4} = 0.168$	$r_{p1} = -0.339$ $r_{p2} = 0.010$ $r_{p3} = 0.048$ $r_{p4} = 0.054$
	Echo power	$r_{p1} = 0.501$ $r_{p2} = 0.259$ $r_{p3} = 0.224$ $r_{p4} = 0.306$		$r_{p1} = 0.455$ $r_{p2} = 0.574$ $r_{p3} = 0.608$ $r_{p4} = 0.514$	$r_{p1} = -0.071$ $r_{p2} = -0.186$ $r_{p3} = -0.228$ $r_{p4} = -0.210$
	Thickness	$r_{p1} = 0.695$ $r_{p2} = 0.393$ $r_{p3} = 0.246$ $r_{p4} = 0.264$	$r_{p1} = 0.534$ $r_{p2} = 0.482$ $r_{p3} = 0.508$ $r_{p4} = 0.541$		$r_{p1} = -0.110$ $r_{p2} = -0.199$ $r_{p3} = -0.167$ $r_{p4} = -0.161$
	Altitude	$r_{p1} = 0.091$ $r_{p2} = -0.079$ $r_{p3} = -0.046$ $r_{p4} = 0.030$	$r_{p1} = 0.087$ $r_{p2} = -0.052$ $r_{p3} = -0.118$ $r_{p4} = -0.184$	$r_{p1} = 0.131$ $r_{p2} = 0.031$ $r_{p3} = -0.040$ $r_{p4} = -0.113$	

(b)		Solar minimum			
		Electron density	Echo power	Thickness	Altitude
Solar maximum	Electron density		$r_{s1} = 0.245$ $r_{s2} = 0.179$ $r_{s3} = 0.178$ $r_{s4} = 0.123$	$r_{s1} = 0.428$ $r_{s2} = 0.215$ $r_{s3} = 0.178$ $r_{s4} = 0.173$	$r_{s1} = -0.292$ $r_{s2} = 0.006$ $r_{s3} = 0.045$ $r_{s4} = 0.047$
	Echo power	$r_{s1} = 0.494$ $r_{s2} = 0.239$ $r_{s3} = 0.202$ $r_{s4} = 0.232$		$r_{s1} = 0.603$ $r_{s2} = 0.643$ $r_{s3} = 0.635$ $r_{s4} = 0.542$	$r_{s1} = -0.047$ $r_{s2} = -0.188$ $r_{s3} = -0.240$ $r_{s4} = -0.208$
	Thickness	$r_{s1} = 0.668$ $r_{s2} = 0.311$ $r_{s3} = 0.202$ $r_{s4} = 0.230$	$r_{s1} = 0.615$ $r_{s2} = 0.621$ $r_{s3} = 0.637$ $r_{s4} = 0.595$		$r_{s1} = -0.168$ $r_{s2} = -0.185$ $r_{s3} = -0.141$ $r_{s4} = -0.124$
	Altitude	$r_{s1} = 0.095$ $r_{s2} = -0.052$ $r_{s3} = -0.031$ $r_{s4} = 0.058$	$r_{s1} = 0.111$ $r_{s2} = -0.051$ $r_{s3} = -0.107$ $r_{s4} = -0.190$	$r_{s1} = 0.161$ $r_{s2} = 0.008$ $r_{s3} = -0.052$ $r_{s4} = -0.076$	

b, we note that the highest Pearson correlation coefficient and Spearman rank correlation coefficient are obtained for monolayers. Specifically for the solar maximum, the Pearson coefficient is 0.501 and the Spearman rank coefficient is 0.494, while for the solar minimum, the Pearson coefficient is 0.270 and the Spearman rank coefficient is 0.245. These results can possibly suggest that at higher ionization levels at 92 km altitude, the PMSEs have a higher intensity, indicated by a higher echo power, particularly in the case of monolayers during the solar maximum. On the other hand, the lowest correlations were found for multilayers containing three layers, with a Pearson coefficient of 0.224 and a Spearman rank coefficient of 0.202 for the solar maximum and a Pearson coefficient of 0.306 and a Spearman rank coefficient of 0.232 for the solar minimum.

Narayanan et al. (2022) investigated the effects of particle precipitation on PMSE formation using electron densities from 90 to 95 km. They found a clear response in the power of the PMSEs during particle precipitation events: in all their cases, an increase in PMSE power was observed in association with particle precipitations. However, Narayanan et al. (2022) say that the particle precipitation does not seem to be related to the very existence of PMSEs and that there seems to be no linear relationship between both, which is consistent with the results of our study. Specifically, we observe weak Pearson correlation coefficients during the solar minimum, as reported in Table 5a, which is consistent with the findings of Narayanan et al. (2022), who analyzed EISCAT VHF observations from 2019, a period corresponding to the solar minimum. However, our results indicate slightly higher Pearson correlation coefficients during the solar maximum, particularly for monolayers. It would be worthwhile to conduct a similar investigation as Narayanan et al. (2022) during the solar maximum phase of a solar cycle. These findings should be interpreted with care, considering that our study differs from that of Narayanan et al. (2022) in several ways. Specifically, our data selection process did not require the simultaneous presence of PMSEs and particle precipitation.

From Table 4, one can notice that for the combination of echo power and electron density during the solar maximum, the obtained Pearson correlation coefficient is 0.338 and the Spearman rank correlation coefficient is 0.305. In their study, Rauf et al. (2018a) used EISCAT VHF data to investigate the correlation between PMSE strength and particle precipitation over a dataset consisting of 111 h, or 5 d of observation. However, in their case, they derived the Pearson and Spearman correlation coefficients between their PMSE proxy, which is equivalent to our use of the term “echo power” and the electron density at 90 km altitude instead of 92 km we used. Nevertheless, it is interesting to note that they also found a positive correlation between echo power and electron density of 0.15 for the Pearson correlation coefficient, and 0.24 for the Spearman correlation coefficient. It is important to note that during their analysis, Rauf et al. (2018a) only selected data from 8 to 12 July 2013, when PMSEs and particle precipitation were occurring simultaneously. In our study, we included data from the year 2013 in the solar maximum period. Hence, we compare the correlation coefficients from Rauf et al. (2018a) with our own coefficients for the solar maximum. While both studies discovered a positive correlation, our findings had higher correlation coefficients than the Rauf et al. (2018a) study. One factor which could explain this difference might be the fact that in Rauf et al. (2018a) data, PMSEs and particle precipitation were always occurring simultaneously, while in our analysis, data were selected solely based on the presence of PMSEs without any filtering based on the occurrence of particle precipitation. It should be noted that while a PMSE was present in all of our cases, there may have been instances where particle precipitation was present and instances where it was not. Another factor might be that we used a lower threshold for PMSE detection than Rauf et al. (2018a) due to the fact that we used a classification model on the data beforehand. We used the threshold $N_\mathrm{e} > 3.2 \times 10^{10}\,\mathrm{m}^{-3}$, while Rauf et al. (2018a) used $N_\mathrm{e} > 4.6 \times 10^{11}\,\mathrm{m}^{-3}$.

4 Conclusions

The altitude, the echo power and the thickness of layers in PMSEs have, on average, higher values during the solar maximum than during the solar minimum. During the PMSE occurrence, as expected, the electron density at 92 km is, on average, higher during the solar maximum than solar minimum. Taking into account the findings presented by Lübken et al. (2021) that show an increase in ice particle size over time in conjunction with these results, it is difficult to isolate the exact mechanisms by which the PMSE properties are affected. Nonetheless, breaking down the multilayer sets into individual layers reveals a consistent trend: in both solar maximum and solar minimum cases, the altitude of the top layer tends to rise with an increasing number of multilayers. This tendency extends to the second- and third-highest layers as well. Our findings support the conclusions drawn by Hoffmann et al. (2005) regarding the altitude and occurrence rate of both mono and multiple layers. Additionally, when examining the lowest layer in various multilayer sets, the lowest layer almost always aligns with the NLC altitude as reported by Fiedler et al. (2003) of 83.3 km. The recent work by Vellalassery et al. (2024) addresses the variation in NLCs throughout the solar cycle. They used the Leibniz Institute Middle Atmosphere (LIMA) model and the Mesospheric Ice Microphysics and Transport (MIMAS) model over the years 1849 to 2019, corresponding to 15 solar cycles. Their findings indicate that NLC altitudes increase during periods of solar maximum and decrease during the solar minimum. Additionally, they observed a long-term decline in NLC altitude, attributed to the overall shrinking of the atmosphere. Our findings align with those results, as we observed a lower altitude of the PMSEs during the solar minimum period (years 2019 and 2020) compared to the solar maximum phase (years 2013 to 2015).

We have observed that the thickness of the layers decreases as the number of multilayers increases, indicating that a single monolayer will be thicker than the separate layers of a set of two multilayers, which in turn will be thicker than the separate layers of three multilayers and so on. This is mostly the case for layers 1 to 3 and for both the solar maximum and solar minimum. Furthermore, the echo power was found to decrease with increasing multilayers but only in the case of the solar maximum and mostly for layers 1 to 3. This suggests that there may be a relationship between the number of layers, echo power and thickness. Our study is consistent with the findings of Li et al. (2016) where they found that the thickness of multilayers decreases with increasing number of multilayers.

Based on our investigation, we have found that the electron density at 92 km altitude and the echo power are positively correlated with the thickness for all the layers and for both the solar maximum and solar minimum except for four multilayers at the solar minimum. We also found similar results as Rauf et al. (2018a), discovering a positive correlation between electron density and echo power, especially for monolayers and during the solar maximum. This can possibly suggest that under those conditions and at higher ionization levels at 92 km altitude, the PMSEs are stronger, which is indicated by a higher echo power. The electron density was highly correlated with the thickness of the layers except for the solar minimum and four multilayers. The correlation is the strongest, especially for the solar maximum and monolayers, which indicates that at higher ionization levels at 92 km altitude, the PMSE monolayers are commonly thicker. Comparing our results with Li et al. (2016) led us to the hypothesis that the thickness of the layers could be related to the vertical wavelength of gravity waves, with larger wavelengths producing thicker layers. Further investigations could explore this hypothesis, potentially providing a means of inferring the wavelength of gravity waves through PMSE observations at these altitudes.

For both solar maximum and solar minimum periods, the monolayers attained the lowest average electron density of their respective seasons though the trend was relatively weak. An argument could be made that higher electron densities at ionospheric altitudes might be necessary to generate multilayered PMSEs, though this requires more investigation.

A parallel can be drawn with the findings of Schäfer et al. (2020) regarding multilayered NLCs, where both of our studies found a similar occurrence rate for thick-layer formation above 1 km thickness. In light of the similarities in multilayer formation between PMSEs and NLCs, future studies may be able to utilize findings from NLC research to gain insights into PMSE dynamics.

In conclusion, the mechanism of the formation PMSEs might be presently well understood; however, the exact conditions leading to multilayered PMSE formation remain unclear, and further investigation is required. Hoffmann et al. (2005) proposed that PMSE layering can be explained by the stratification of ice particles resulting from successive nucleation cycles near the mesopause followed by growth and sedimentation. Other authors hypothesized a potential connection between PMSE multilayers and gravity waves (Li et al., 2016; Hoffmann et al., 2005). Our hypothesis on the formation of multilayered PMSEs is that gravity waves transport particles into regions of low temperature at varying altitudes. In these conditions, ice particles can form and grow. This process may impact the size of ice particles, which in turn could affect their spatial distribution via sedimentation, and potentially influence the formation of multilayers. Therefore, for example, future research could include further investigation of the connections between multilayered PMSE formation, winds and gravity waves. One possible way to do this is to measure gravity waves using the EISCAT radar (Günzkofer et al., 2023). Utilizing the dissipative anelastic gravity wave dispersion relation, Günzkofer et al. (2023) derive vertical wind profiles within the lower thermosphere. This is a promising avenue for further measuring of gravity waves during PMSE occurrences. Understanding the complex interplay of the factors involving the formation of PMSEs is crucial to gain insights into the thermodynamic and fluid dynamic processes occurring at altitudes between 80 and 90 km. While differences between the results from observations during the solar maximum and during the solar minimum considering all the layers together are statistically significant, the cause for the differences needs to be confirmed by future studies.

Appendix A

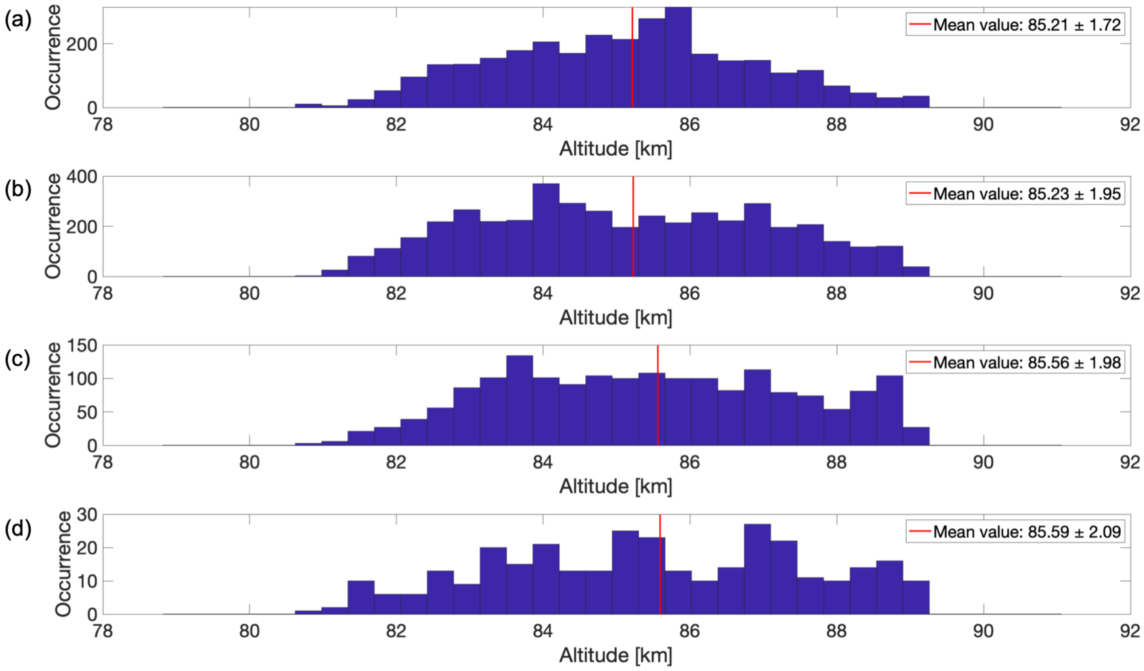

Figure A1. Altitude distribution of the data during the solar maximum for **(a)** monolayers, **(b)** multilayers with two layers, **(c)** multilayers with three layers and **(d)** multilayers with four layers. Each subplot was its respective averaged mean altitude of all the multilayers represented with a red line on the graph and specified in the legend together with 1 standard deviation.

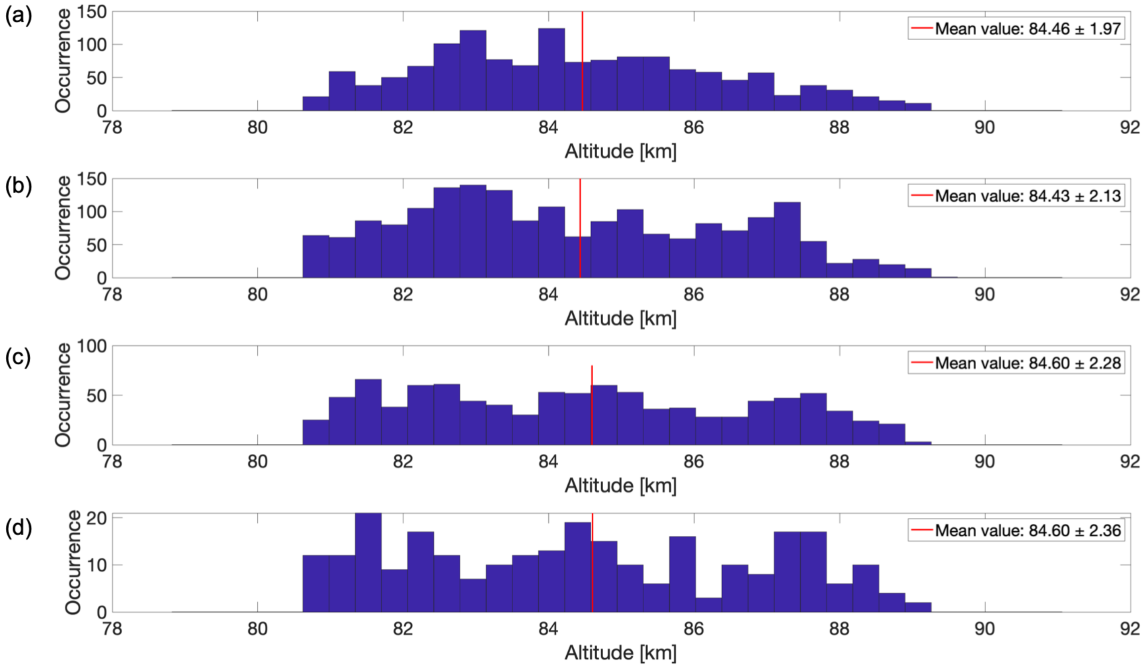

Figure A2. Altitude distribution of the data during the solar minimum for **(a)** monolayers, **(b)** multilayers with two layers, **(c)** multilayers with three layers and **(d)** multilayers with four layers. Each subplot was its respective averaged mean altitude of all the multilayers represented with a red line on the graph and specified in the legend together with 1 standard deviation.

Appendix B

Table B1. P values for all combinations of layers shown in Figs. 4 and 5.

	P values	Solar minimum									
		Monolayers	Layer 1 of 2	Layer 2 of 2	Layer 1 of 3	Layer 2 of 3	Layer 3 of 3	Layer 1 of 4	Layer 2 of 4	Layer 3 of 4	Layer 4 of 4
Solar maximum	Monolayers		$P < 0.0001$	$P < 0.0001$	$P < 0.0001$	0.3618	$P < 0.0001$	$P < 0.0001$	$P < 0.0001$	0.0027	$P < 0.0001$
	Layer 1 of 2	$P < 0.0001$		$P < 0.0001$	$P < 0.0001$	$P < 0.0001$	$P < 0.0001$	$P < 0.0001$	0.0268	$P < 0.0001$	$P < 0.0001$
	Layer 2 of 2	$P < 0.0001$	$P < 0.0001$		$P < 0.0001$	$P < 0.0001$	$P < 0.0001$	$P < 0.0001$	$P < 0.0001$	$P < 0.0001$	$P < 0.0001$
	Layer 1 of 3	$P < 0.0001$	$P < 0.0001$	$P < 0.0001$		$P < 0.0001$	$P < 0.0001$	0.0106	$P < 0.0001$	$P < 0.0001$	$P < 0.0001$
	Layer 2 of 3	$P < 0.0001$	$P < 0.0001$	$P < 0.0001$	$P < 0.0001$		$P < 0.0001$	$P < 0.0001$	$P < 0.0001$	$P < 0.0001$	$P < 0.0001$
	Layer 3 of 3	$P < 0.0001$	$P < 0.0001$	0.0002	$P < 0.0001$	$P < 0.0001$		$P < 0.0001$	$P < 0.0001$	$P < 0.0001$	0.0001
	Layer 1 of 4	$P < 0.0001$	$P < 0.0001$	$P < 0.0001$	0.0001	$P < 0.0001$	$P < 0.0001$		$P < 0.0001$	$P < 0.0001$	$P < 0.0001$
	Layer 2 of 4	$P < 0.0001$	0.0448	$P < 0.0001$	$P < 0.0001$	$P < 0.0001$	$P < 0.0001$	$P < 0.0001$		$P < 0.0001$	$P < 0.0001$
	Layer 3 of 4	0.0411	$P < 0.0001$	$P < 0.0001$	$P < 0.0001$	$P < 0.0001$	$P < 0.0001$	$P < 0.0001$	$P < 0.0001$		$P < 0.0001$
	Layer 4 of 4	$P < 0.0001$	$P < 0.0001$	$P < 0.0001$	$P < 0.0001$	$P < 0.0001$	$P < 0.0001$	$P < 0.0001$	$P < 0.0001$	$P < 0.0001$	

Table B2. P values for all combinations of layers and parameters shown in Figs. 3, A1, A2, 6, 7, 8, 9, 10, 11, 12, 13 and 14.

		Altitude	Electron density	Echo power	Thickness
Solar maximum	Layers 1–2	$P = 0.6462$	$P < 0.0001$	$P < 0.0001$	$P < 0.0001$
	Layers 1–3	$P < 0.0001$	$P = 0.0003$	$P < 0.0001$	$P < 0.0001$
	Layers 1–4	$P = 0.0002$	$P = 0.0831$	$P < 0.0001$	$P < 0.0001$
	Layers 2–3	$P < 0.0001$	$P = 0.0804$	$P < 0.0001$	$P < 0.0001$
	Layers 2–4	$P = 0.0014$	$P = 0.4000$	$P < 0.0001$	$P < 0.0001$
	Layers 3–4	$P = 0.8035$	$P = 1.0000$	$P = 0.0012$	$P = 0.0002$
Solar minimum	Layers 1–2	$P = 0.6808$	$P < 0.0001$	$P = 0.3483$	$P < 0.0001$
	Layers 1–3	$P = 0.1098$	$P < 0.0001$	$P = 0.0009$	$P < 0.0001$
	Layers 1–4	$P = 0.3030$	$P < 0.0001$	$P = 0.0001$	$P < 0.0001$
	Layers 2–3	$P = 0.0481$	$P < 0.0001$	$P < 0.0001$	$P < 0.0001$
	Layers 2–4	$P = 0.2284$	$P = 0.0091$	$P < 0.0001$	$P < 0.0001$
	Layers 3–4	$P = 1.0000$	$P = 0.5707$	$P = 0.0728$	$P = 0.0002$
	Solar max–min	$P < 0.0001$	$P < 0.0001$	$P < 0.0001$	$P < 0.0001$

Table B3. P values for the correlation coefficients for all layers together during the solar maximum and solar minimum shown in Table 4.

	P values	Solar min			
		Electron density	Echo power	Thickness	Altitude
Solar max	Electron density		1.53E-27	1.38E-54	1.06E-04
	Echo power	1.02E-203		0	2.51E-28
	Thickness	0	0		1.94E-30
	Altitude	0.772	2.24E-03	0.0175	

Table B4. *P* values for the correlation coefficients for the mono- and multilayers separately, during the solar maximum and solar minimum shown in Table 5b).

	P values	Solar minimum			
		Electron density	Echo power	Thickness	Altitude
Solar maximum	Electron density		Layer 1 = 1.86E-19 Layer 2 = 1.49E-14 Layer 3 = 4.17E-04 Layer 4 = 0.0489	Layer 1 = 1.02E-59 Layer 2 = 2.84E-08 Layer 3 = 4.17E-04 Layer 4 = 0.00542	Layer 1 = 2.08E-27 Layer 2 = 0.800 Layer 3 = 0.165 Layer 4 = 0.455
	Echo power	Layer 1 = 4.06E-183 Layer 2 = 5.68E-58 Layer 3 = 4.29E-12 Layer 4 = 3.19E-05		Layer 1 = 3.58E-139 Layer 2 = 5.62E-112 Layer 3 = 4.17E-04 Layer 4 = 6.96E-22	Layer 1 = 0.0760 Layer 2 = 2.30E-16 Layer 3 = 2.51E-14 Layer 4 = 5.92E-04
	Thickness	Layer1 = 0 Layer 2 = 9.23E-99 Layer 3 = 1.65E-17 Layer 4 = 3.60E-05	Layer 1 = 4.186E-319 Layer 2 = 0 Layer 3 = 8.51E-205 Layer 4 = 1.89E-32		Layer 1 = 2.87E-10 Layer 2 = 8.82E-06 Layer 3 = 4.17E-04 Layer 4 = 0.0418
	Altitude	Layer 1 = 1.80E-07 Layer 2 = 5.19E-04 Layer 3 = 0.194 Layer 4 = 0.305	Layer 1 = 6.87E-10 Layer 2 = 5.85E-04 Layer 3 = 5.32E-06 Layer 4 = 6.02E-04	Layer 1 = 2.93E-19 Layer 2 = 0.592 Layer 3 = 0.0288 Layer 4 = 0.174	

Data availability. EISCAT VHF data are available under https://madrigal.eiscat.se/madrigal/ (EISCAT, 2023).

Author contributions. DJ, PS, DH and IM: conceptualization; DJ: data curation, investigation, software, and writing (original draft); IM: funding acquisition; IM: project administration; PS, DH and IM: supervision; PS, DH and IM: validation; DJ, PS, DH and IM: writing (review and editing). All authors have read and agreed to the published version of the paper.

Competing interests. At least one of the (co-)authors is a member of the editorial board of *Annales Geophysicae*. The peer-review process was guided by an independent editor, and the authors also have no other competing interests to declare.

Special issue statement. This article is part of the special issue "Special issue on the joint 20th International EISCAT Symposium and 15th International Workshop on Layered Phenomena in the Mesopause Region". It is a result of the Joint 20th International EISCAT Symposium 2022 and 15th International Workshop on Layered Phenomena in the Mesopause Region, Eskilstuna, Sweden, 15–19 August 2022.

Acknowledgements. This work was carried out within a project funded by the Research Council of Norway. The Norwegian participation in EISCAT and EISCAT3D is funded by the Research Council of Norway. The EISCAT Scientific Association is supported by research organizations in Norway (NFR), Sweden (VR), Finland (SA), Japan (NIPR and STEL), China (CRIPR) and the United Kingdom (NERC). The authors would like to thank the anonymous reviewers for their valuable feedback and constructive comments, which have helped improve the quality of this paper.

Financial support. This research has been supported by the Norges Forskningsråd (NFR; grant no. 275503) and the UiT (The Arctic University of Norway) contribution to the EISCAT_3D project funded by the Research Council of Norway through research infrastructure (grant no. 245683).

Review statement. This paper was edited by Alexa Halford and reviewed by two anonymous referees.

References

Avaste, O.: Noctilucent clouds, J. Atmos. Terr. Phys., 55, 133–143, https://doi.org/10.1016/0021-9169(93)90118-I, 1993.

Belova, E., Chilson, P. B., Kirkwood, S., and Rietveld, M. T.: The response time of PMSE to ionospheric heating, J. Geophys. Res.-Atmos., 108, 8446, https://doi.org/10.1029/2002JD002385, 2003.

Beynon, W. and Williams, P.: Incoherent scatter of radio waves from the ionosphere, Rep. Prog. Phys., 41, 909–956, https://doi.org/10.1088/0034-4885/41/6/003, 1978.

Cho, J. Y. N. and Röttger, J.: An updated review of polar mesosphere summer echoes: Observation, theory, and their relationship to noctilucent clouds and subvisible aerosols, J. Geophys. Res.-Atmos., 102, 2001–2020, https://doi.org/10.1029/96JD02030, 1997.

EISCAT: EISCAT VHF data, Madrigal Database, EISCAT [data set], https://madrigal.eiscat.se/madrigal/, last access: 15 January 2023.

Fiedler, J., Baumgarten, G., and von Cossart, G.: Noctilucent clouds above ALOMAR between 1997 and 2001: Occurrence and properties, J. Geophys. Res.-Atmos., 108, 8453, https://doi.org/10.1029/2002JD002419, 2003.

Fritts, D. C., Miller, A. D., Kjellstrand, C. B., Geach, C., Williams, B. P., Kaifler, B., Kaifler, N., Jones, G., Rapp, M., Limon, M., Reimuller, J., Wang, L., Hanany, S., Gisinger, S., Zhao, Y., Stober, G., and Randall, C. E.: PMC Turbo: Studying Gravity Wave and Instability Dynamics in the Summer Mesosphere Using Polar Mesospheric Cloud Imaging and Profiling From a Stratospheric Balloon, J. Geophys. Res.-Atmos., 124, 6423–6443, https://doi.org/10.1029/2019JD030298, 2019.

Günzkofer, F., Pokhotelov, D., Stober, G., Mann, I., Vadas, S. L., Becker, E., Tjulin, A., Kozlovsky, A., Tsutsumi, M., Gulbrandsen, N., Nozawa, S., Lester, M., Belova, E., Kero, J., Mitchell, N. J., and Borries, C.: Inferring neutral winds in the ionospheric transition region from atmospheric-gravity-wave traveling-ionospheric-disturbance (AGW-TID) observations with the EISCAT VHF radar and the Nordic Meteor Radar Cluster, Ann. Geophys., 41, 409–428, https://doi.org/10.5194/angeo-41-409-2023, 2023.

Hocking, W., Rüster, R., and Czechowsky, P.: Absolute reflectivities and aspect sensitivities of VHF radio wave scatterers measured with the SOUSY radar, J. Atmos. Terr. Phys., 48, 131–144, https://doi.org/10.1016/0021-9169(86)90077-2, 1986.

Hoffmann, P., Rapp, M., Serafimovich, A., and Latteck, R.: On the occurrence and formation of multiple layers of polar mesosphere summer echoes, Geophys. Res. Lett., 32, L05812, https://doi.org/10.1029/2004GL021409, 2005.

Jozwicki, D., Sharma, P., and Mann, I.: Investigation of Polar Mesospheric Summer Echoes Using Linear Discriminant Analysis, Remote Sens., 13, 522, https://doi.org/10.3390/rs13030522, 2021.

Jozwicki, D., Sharma, P., Mann, I., and Hoppe, U.-P.: Segmentation of PMSE Data Using Random Forests, Remote Sens., 14, 2976, https://doi.org/10.3390/rs14132976, 2022.

Latteck, R., Renkwitz, T., and Chau, J. L.: Two decades of long-term observations of polar mesospheric echoes at 69° N, J. Atmos. Sol.-Terr. Phys., 216, 105576, https://doi.org/10.1016/j.jastp.2021.105576, 2021.

Lehtinen, M. S. and Huuskonen, A.: General incoherent scatter analysis and GUISDAP, J. Atmos. Terr. Phys., 58, 435–452, https://doi.org/10.1016/0021-9169(95)00047-X, 1996.

Li, H., Wu, J., and Zhou, Z.: The formation of multiple layers of ice particles in the polar summer mesopause region, Ann. Geophys., 34, 117–122, https://doi.org/10.5194/angeo-34-117-2016, 2016.

Lübken, F.-J., Berger, U., and Baumgarten, G.: Stratospheric and solar cycle effects on long-term variability of mesospheric ice clouds, J. Geophys. Res.-Atmos., 114, D00I06, https://doi.org/10.1029/2009JD012377, 2009.

Lübken, F.-J., Baumgarten, G., and Berger, U.: Long term trends of mesopheric ice layers: A model study, J. Atmos. Sol.-Terr. Phys., 214, 105378, https://doi.org/10.1016/j.jastp.2020.105378, 2021.

Myers, J. and Well, A.: Research Design and Statistical Analysis, 2nd Edn., Hillsdale, NJ, Lawrence Erlbaum Associates, Psychology Press, https://doi.org/10.4324/9781410607034, 2003.

Narayanan, V. L., Häggström, I., and Mann, I.: Effects of particle precipitation on the polar mesospheric summer echoes observed by EISCAT VHF 224 MHz radar, Adv. Space Res., 69, 3350–3361, https://doi.org/10.1016/j.asr.2022.02.015, 2022.

Rapp, M. and Lübken, F.-J.: Polar mesosphere summer echoes (PMSE): Review of observations and current understanding, Atmos. Chem. Phys., 4, 2601–2633, https://doi.org/10.5194/acp-4-2601-2004, 2004.

Rapp, M. and Thomas, G. E.: Modeling the microphysics of mesospheric ice particles: Assessment of current capabilities and basic sensitivities, J. Atmos. Sol.-Terr. Phys., 68, 715–744, https://doi.org/10.1016/j.jastp.2005.10.015, 2006.

Rauf, A., Li, H., Ullah, S., Lin, M., Wang, B., and Wang, M.: Statistical study about the influence of particle precipitation on mesosphere summer echoes in polar latitudes during July 2013, Earth Planet. Space, 70, 108, https://doi.org/10.1186/s40623-018-0885-6, 2018a.

Rauf, A., Li, H., Ullah, S., Lin, M., Wang, B., and Wang, M.: Investigation of PMSE dependence on high energy particle precipitation during their simultaneous occurrence, Advances in Space Research, 63, https://doi.org/10.1016/j.asr.2018.09.007, 2018b.

Schäfer, B., Baumgarten, G., and Fiedler, J.: Small-scale structures in noctilucent clouds observed by lidar, J. Atmos. Sol.-Terr. Phys., 208, 105384, https://doi.org/10.1016/j.jastp.2020.105384, 2020.

Shucan, G., Li, H., Xu, T., Zhu, M., Wang, M., Lin, M., Ullah, S., and Rauf, A.: Characteristics of the layered polar mesosphere summer echoes occurrence ratio observed by EISCAT VHF 224 MHz radar, Ann. Geophys., 37, 417–427, https://doi.org/10.5194/angeo-37-417-2019, 2019.

Singer, W., Hoffmann, P., Grandhi, K. K., Mitchell, N., and Wendt, V.: Atmospheric Coupling by Gravity Waves: Climatology of Gravity Wave Activity, Mesospheric Turbulence and Their Relations to Solar Activity, Springer, 409–427, ISBN 978-94-007-4347-2, https://doi.org/10.1007/978-94-007-4348-9_22, 2012.

Vellalassery, A., Baumgarten, G., Grygalashvyly, M., and Lübken, F.-J.: Long-Term Evolution in Noctilucent Clouds' Response to the Solar Cycle: A Model-Based Study, Atmosphere, 15, 88, https://doi.org/10.3390/atmos15010088, 2024.

Wilks, D.: Statistical Methods in the Atmospheric Sciences, 4th Edn., Academic Press, 100, 50–60, https://doi.org/10.1016/C2017-0-03921-6, 1995.

Zhao, X. R., Sheng, Z., Shi, H. Q., Weng, L. B., and Liao, Q. X.: Long-Term Trends and Solar Responses of the Mesopause Temperatures Observed by SABER During the 2002–2019 Period, J. Geophys. Res.-Atmos., 125, e2020JD032418, https://doi.org/10.1029/2020JD032418, 2020.